

TECHNISCHE UNIVERSITÄT MÜNCHEN  
Fakultät für Chemie

Max-Planck-Institut für Biochemie  
Abteilung für Molekulare Strukturbiologie

# **The conformational landscape of the AAA<sup>+</sup>-ATPase of the 26S proteasome studied by cryo-electron microscopy**

Marc Alexander Wehmer

Vollständiger Abdruck der von der Fakultät für Chemie  
der Technischen Universität München  
zur Erlangung des akademischen Grades eines  
Doktors der Naturwissenschaften  
genehmigten Dissertation.

Vorsitzender:

Prof. Dr. Johannes Buchner

Prüfer der Dissertation:

1. Hon.-Prof. Dr. Wolfgang Baumeister
2. Prof. Dr. Sevil Weinkauf
3. Prof. Dr. Bernd Reif (mündliche Prüfung)  
Prof. Dr. Friedrich Förster (schriftliche Beurteilung)

Die Dissertation wurde am 28.06.2017 bei der Technischen Universität München eingereicht und durch die Fakultät für Chemie am 04.09.2017 angenommen.



# Table of Contents

Table of Contents .....	i
Summary .....	iii
Zusammenfassung.....	iv
1 Introduction .....	1
1.1 Protein homeostasis.....	1
1.2 The ubiquitin-proteasome system .....	2
1.3 The 26S proteasome .....	3
1.3.1 The 19S regulatory particle .....	4
1.3.2 Conformational states of the 26S proteasome .....	6
1.3.3 The AAA <sup>+</sup> -ATPase.....	8
1.3.4 The 20S core particle.....	11
1.3.5 Regulator – CP interactions and opening of the 20S pore .....	12
2 Goal of the PhD thesis .....	14
3 Materials and Methods.....	15
3.1 Materials .....	15
3.1.1 Chemicals and consumables .....	15
3.1.2 Buffers and solutions.....	16
3.1.3 Cell culture media .....	17
3.1.4 Strains.....	17
3.2 Methods .....	17
3.2.1 Yeast cell culture .....	17
3.2.2 Proteasome purification.....	17
3.2.3 Analytical methods.....	18
3.2.4 Electron microscopy .....	20
3.2.5 Image processing.....	23
3.2.6 Single particle analysis .....	24
3.2.7 Model-building and analysis .....	26
4 Results .....	28
4.1 Purification of the yeast 26S proteasome.....	28
4.2 ATPase activity in the presence of nucleotide analogs .....	31
4.3 Cryo-EM reconstruction of the 26S proteasome in the presence of ATP .....	32

4.4	Cryo-EM reconstruction of the 26S proteasome in the presence of AMP-PNP shows the s3 state .....	38
4.5	Cryo-EM reconstruction of the 26S proteasome in the presence of BeF <sub>x</sub> reveals an hitherto unobserved state .....	39
4.5.1	Ubp6 is bound in the s4 state.....	41
4.6	Comparison between the s1, s2, s3, and s4 states of the yeast 26S proteasome .....	42
4.6.1	Structural comparison between the s1, s2, s3, and s4 states.....	42
4.6.2	The staircase arrangements of the pore-loops of the AAA <sup>+</sup> -ATPase change height between the states.....	46
4.6.3	The nucleotide-binding pockets possess different conformations.....	48
4.6.4	The gate of the CP is open in the s4 state and the HbYX motifs bind constitutively .....	50
4.7	Comparison with other 26S proteasome models .....	54
4.7.1	Comparison of the yeast s1, s2 and s3 models .....	54
4.7.2	Comparison of the AAA <sup>+</sup> -ATPase.....	56
4.7.3	Comparison of the gate of the 20S proteasome .....	61
5	Discussion.....	62
5.1	High-resolution proteasome structures.....	62
5.2	The staircase arrangement of the AAA <sup>+</sup> -ATPase.....	63
5.3	Nucleotide binding pockets of the 26S proteasome.....	65
5.4	Gate-opening mechanism of the CP.....	66
5.5	Functional model of ATP hydrolysis coupled to substrate translocation .....	68
6	Conclusion and Outlook .....	71
7	Appendix .....	72
7.1	Abbreviations .....	72
7.2	Bibliography .....	74
7.3	Acknowledgements.....	80

## Summary

In eukaryotic cells, two major pathways, the ubiquitin proteasome system (UPS) and autophagy, mediate protein degradation. The UPS is responsible for the specific elimination of damaged proteins or proteins that are no longer needed in the cell. It is largely divided into two processes: ubiquitylation and degradation. Ubiquitylation facilitates specific substrate selection, whereas degradation is mediated by the 26S proteasome. The 26S proteasome is a 2.5 MDa molecular machine that is composed of two subcomplexes, the 20S core particle (CP) and the 19S regulatory particle (RP), containing 14 and 19 subunits, respectively. The entrance of substrate into the CP cavity, where proteolysis takes place, is controlled by the RP. The RP consists of six AAA<sup>+</sup>-ATPases (Rpt1-6) and various non-ATPase subunits (Rpn1-3 and Rpn5-13). The base of the RP is formed by a heterohexameric ATPase module, which unfolds and translocates substrates into the CP.

Single-particle cryo-electron microscopy (cryo-EM) has emerged as a powerful technique for studying the structure of biological macromolecules. Although the development of direct electron detectors and automated electron microscopes allowed to push resolution to a range comparable with that of X-ray crystallography and NMR spectroscopy, it is still challenging to obtain high-resolution structures of macromolecular complexes like the 26S proteasome, which displays structural heterogeneity. In order to explore the conformational landscape, we applied single particle analysis and three-dimensional (3D) classification to the 26S proteasome using nucleotides and nucleotide analogs. Thereby we were able to reconstruct electron density maps of four distinct conformational states (s1 to s4) with resolutions varying from 4 to 8 Å. The resolution of the four conformers allowed us to build atomic models which provided new insights into the functional cycle of the yeast 26S proteasome. In all four states the three conserved HbYX motifs of the Rpt subunits constitutively bind the CP. Only in the newly described s4 state of the proteasome, the gate of the CP is open and the interaction of the C-terminus of Rpt6 with the CP was observed. Taken together the structures described in this study allow us to propose a functional model of the 26S proteasome driven by ATP hydrolysis.

## Zusammenfassung

In eukaryotischen Zellen gibt es zwei Hauptwege für den Proteinabbau: das Ubiquitin-Proteasom-System (UPS) und Autophagie. Das UPS ist verantwortlich für die spezifische Beseitigung von geschädigten Proteinen oder Proteinen die in der Zelle nicht mehr benötigt werden. Es ist weitgehend in zwei Wege unterteilt: Ubiquitinierung und Abbau. Die spezifische Substratelektion wird durch Ubiquitinierung erreicht, während der Abbau durch das 26S-Proteasom erfolgt. Das 26S-Proteasom ist eine 2,5 MDa-Molekülmaschine, die aus zwei Subkomplexen, dem 20S-Kernpartikel (CP) und dem 19S-regulatorischen Partikel (RP) besteht, die jeweils 14 bzw. 19 Untereinheiten enthalten. Der Eintritt des Substrats in den CP-Hohlraum, wo die Proteolyse stattfindet, wird durch das RP gesteuert. Das RP besteht aus sechs AAA<sup>+</sup>-ATPasen (Rpt1-6) und verschiedenen Nicht-ATPase-Untereinheiten (Rpn1-3 und Rpn5-13). Die Basis des RPs wird durch ein heterohexameres AAA<sup>+</sup>-ATPase-Modul gebildet, das Substrate in das CP entfaltet und transloziert.

Die Einzelpartikel-Kryo-Elektronenmikroskopie (cryo-EM) ist zu einer wichtigen Technik für die Untersuchung der Struktur biologischer Makromoleküle geworden. Obwohl die Entwicklung von Direktdetektoren und automatisierten Elektronenmikroskopen die Auflösungen in einen mit Röntgenkristallographie und NMR-Spektroskopie vergleichbaren Bereich bringen konnte, ist es immer noch schwierig, hochaufgelöste Strukturen komplexer Makromoleküle wie dem 26S Proteasom, das strukturelle Heterogenität enthält, zu erhalten. Um die Konformationslandschaft des 26S Proteasoms zu untersuchen, wurden dreidimensionale (3D) Klassifikationsansätze von großen Einzelpartikel-Datensätzen, sowie Probenbehandlung mit Nukleotiden und Nukleotid-Analoga verwendet. Dabei konnten wir Elektronendichtekarten von vier verschiedenen Konformationszuständen (s1 bis s4) mit Auflösungen von ~4 bis 8 Å rekonstruieren. Die Auflösung der vier Konformationen ermöglichte es uns, Atommodelle zu bauen, die neue Einblicke in den Funktionszyklus des Hefe-26S-Proteasoms gaben. In allen vier Zuständen binden die drei HbYX-Motive der Rpt-Untereinheiten das CP konstitutiv. Nur in dem hier neu beschriebenen s4-Zustand des Proteasoms ist der Zugang zum CP offen, und die Wechselwirkung des C-Terminus von Rpt6 mit dem CP wurde beobachtet. Zusammengefasst bilden die in dieser Studie beschriebenen Strukturen ein funktionelles Modell des 26S-Proteasoms, das durch ATP-Hydrolyse angetrieben wird.

# 1 Introduction

## 1.1 Protein homeostasis

Cellular protein levels and quality are controlled by distinct mechanisms including protein synthesis, folding and degradation. The network that maintains protein integrity is called protein homeostasis (proteostasis) network (PN) [1] (Figure 1.1).

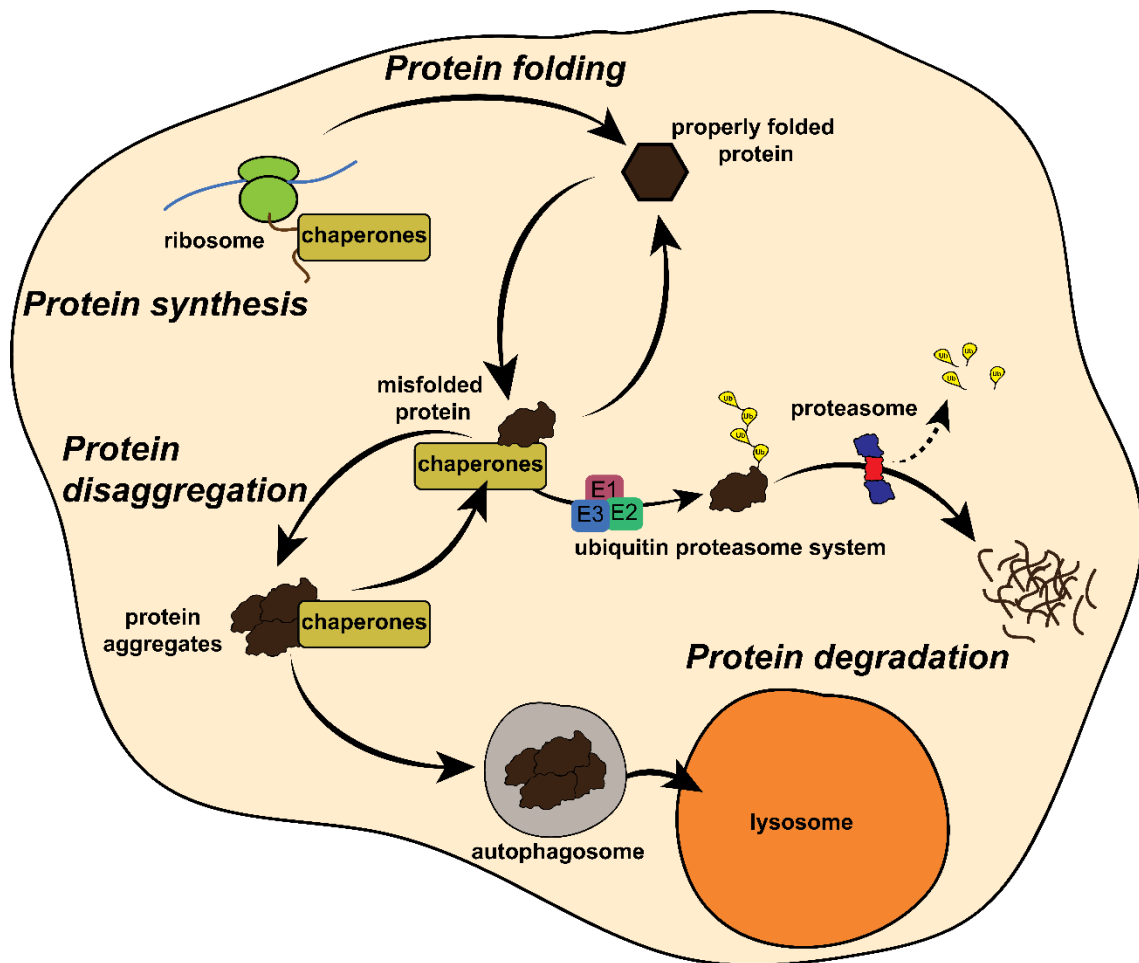


Figure 1.1: Schematic overview of the proteostasis network of a eukaryotic cell. Adapted from [1].

The PN is balanced between protein synthesis and protein degradation. Protein synthesis is controlled by ribosomes, transcription factors and chaperones to produce properly folded proteins. If proteins are no longer needed or malfunction because of protein damage, unfolding or aggregation, the PN removes these proteins through protein degradation [1]. Misfolded proteins can be refolded by molecular chaperones [2] or marked for degradation through the ubiquitin-proteasome system (UPS) [3], which is the primary degradation pathway inside the cell [1]. There are two degradation pathways: autophagy and UPS. Autophagy is responsible for bulk-degradation, whereas the UPS is a selective protein degradation

pathway. In autophagy, target proteins become engulfed by plasma membranes to form autophagosomes which subsequently deliver their cargo to the lysosome [4]. Regulated protein degradation of eukaryotic proteins is achieved by the UPS. The PN is necessary to maintain cell viability and organismal health and malfunction of these pathways leads to several diseases, such as cancer, many neurodegenerative diseases (Huntington’s disease, Alzheimer’s disease, Parkinson’s disease and amyotrophic lateral sclerosis) or cardiovascular diseases [1].

## 1.2 The ubiquitin-proteasome system

In the UPS, target proteins are marked with ubiquitin mediated by an enzymatic cascade involving E1 ubiquitin-activating enzyme, E2 ubiquitin-conjugating enzyme and E3 ubiquitin ligase [3], [5], [6] (Figure 1.2).

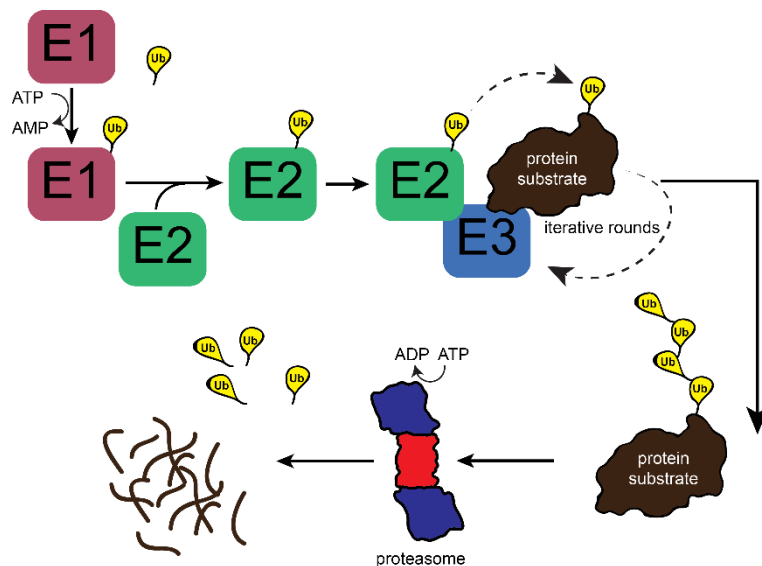


**Figure 1.2:** Schematic representation of the UPS. Adapted from [7].

First, ubiquitin is covalently attached, via a high-energy thioester bond, to E1 in an ATP-dependent manner. In yeast, only a single enzyme, encoded by the gene UBA1, is responsible for the activation of ubiquitin [8]. Next, the activated ubiquitin is transferred to the active cysteine of an E2, from which the ubiquitin is transferred either to the  $\epsilon$ -amino group of a lysine residue of a substrate or other non-canonical ubiquitylation sites (cysteine, serine, threonine). The ubiquitylation of substrates is catalyzed by E3 enzymes [6], [9], [10]. Monoubiquitylated proteins can undergo several rounds of ubiquitin attachment to form polyubiquitin chains. Any of the seven lysine residues (K6, K11, K27, K29, K33, K48 and K63) and the



N-terminus of ubiquitin can be fused to ubiquitin to form a polyubiquitin chain. Target protein can be further modified by the attachment of several different ubiquitin chains: e.g. multi-ubiquitylation, attachment of linear, branched and mixed ubiquitin chains [11], [12], [13], [14], [15]. Proteins marked for degradation by the 26S proteasome are modified by ubiquitin chains with many different topologies. The most common linkage targeting proteins for proteasomal degradation is through K48 [6], [16]. Recent studies have nevertheless shown that the minimum length of the ubiquitin chain of proteins recognized by the 26S proteasome can vary in size and branching [17], [18], [19], [20]. The polyubiquitin chain formed on substrates is recognized by the proteasome which degrades them in an ATP-dependent manner. Polyubiquitin chains of the substrate are cleaved by deubiquitylating enzymes located at the 26S proteasome prior to destruction and recycled for further use [21]. In addition to the position and topology of ubiquitin chains, the efficiency of degradation is influenced by unstructured regions, which serve as initiation sites for degradation [22].

### 1.3 The 26S proteasome

The 26S proteasome is a 2.5 MDa protein complex which is responsible for the regulated protein degradation of polyubiquitylated proteins. The yeast proteasome assembly consists of 33 distinct protein subunits which are highly conserved in evolution. This multi-subunit complex is composed of the barrel-shaped 20S core particle (CP) and one or two 19S regulatory particles (RP) which bind to the ends of the CP [6] (Figure 1.3). Depending on the number of RPs attached to the CP, the proteasome is either called single- or double-capped and therefore varies in dimensions with a maximum length of approximately 45 nm [23].

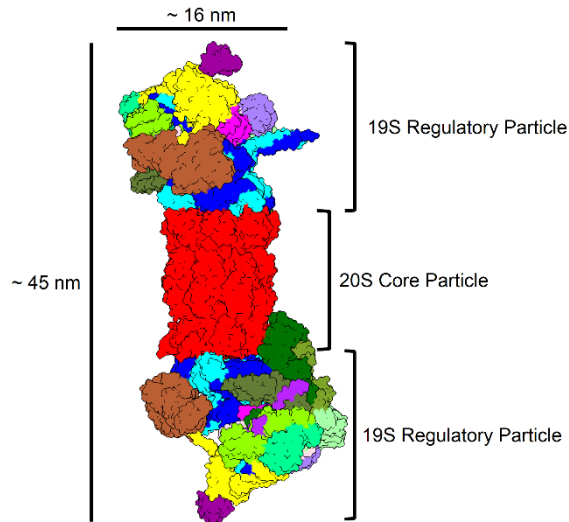


**Figure 1.3:** Dimensions and architecture of the yeast double-capped 26S proteasome. The subunits are colored accordingly: CP (red); Rpt1, Rpt6 and Rpt4 (blue); Rpt2, Rpt3 and Rpt5 (cyan); Rpn1 (brown); Rpn2 (yellow); Rpn3, Rpn5, Rpn6, Rpn7, Rpn9 and Rpn12 (shades of green); and Rpn8, Rpn10, Rpn11, Rpn13 and Sem1 (shades of purple).

The first structural studies on the 26S proteasome using electron microscopy were performed in 1993 and showed that the complex exists both in a single- or double-capped form [24]. Almost 20 years later, the first 3D reconstruction of the 26S proteasome from *Schizosaccharomyces pombe* at a sub-nanometer resolution was published which allowed to position some of the RP subunits (Rpt1-6 and Rpn11) inside the EM density map [25]. In the following years more detailed structures of the 26S proteasome with resolution of up to 7.7 Å revealed the complete subunit arrangement. The authors used hybrid approaches combining the information from crystal structures of individual subunits, homology models, protein-protein crosslinking data and low-resolution structures of GFP-labeled subcomplexes obtained by negative stain EM to elucidate the architecture of the 26S proteasome [26], [27], [28], [29], [30]. In a recent study which used cryo-EM tomography to describe the interior of neuronal cells, the authors were able to reconstruct the 26S proteasome in situ at a resolution of ~30 Å [31].

### 1.3.1 The 19S regulatory particle

The 19S regulatory particle is a 19 subunit protein complex (Figure 1.4) which is composed of two subcomplexes, the lid and the base [23]. The main function of the RP is the regulation of substrate entrance into the CP. The RP therefore caps either one or two ends of the CP and controls access to the catalytic chambers [6].

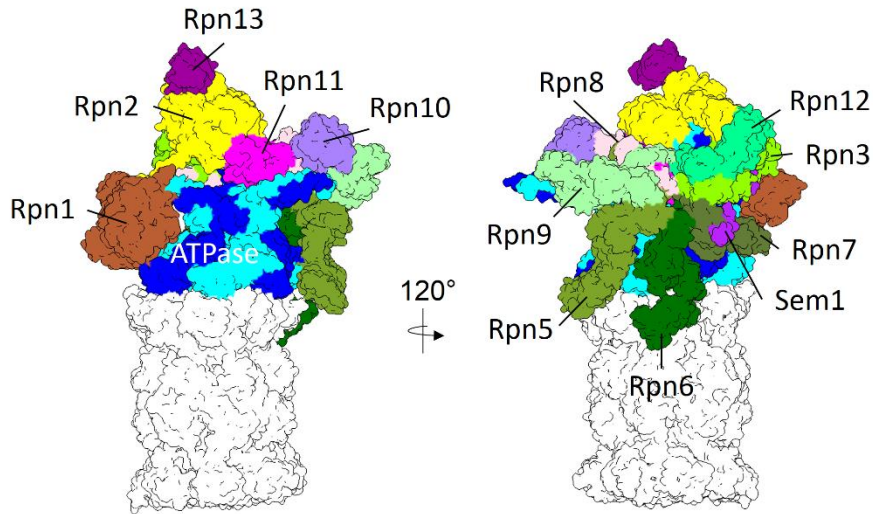


**Figure 1.4:** Architecture of the 19S regulatory particle from the front (left) and back view (right). The subunits of the RP are colored according to the color code applied in Fig. 1.3.

The lid of the RP is composed of the 9 subunits Rpn3, Rpn5, Rpn6, Rpn7, Rpn8, Rpn9, Rpn11, Rpn12 and Sem1. Rpn3,5-7,9 and 12 belong to the proteasome-COP9-initiation factor (PCI)-domain protein family and form a horseshoe-like structure via their PCI-domains where the N-termini point outwards in a radial manner [28], [32]. The subunits Rpn11 and Rpn8 belong to the *Mpr1-Pad1-N-terminal* (MPN) family and form a heterodimer. Although the structures of two subunits are highly conserved, only the Zn<sup>2+</sup>-metalloprotease Rpn11 is catalytically active [33], [34]. It is positioned above the oligosaccharide binding (OB)-ring of the ATPase associated with diverse cellular activities (AAA<sup>+</sup>-ATPase) and cleaves ubiquitin chains from ubiquitylated substrates. The subunit Sem1 is important for the stability of the interaction between Rpn3 and Rpn7 [35]. The C-termini of the lid complex subunits except Sem1, form a central helical bundle, which is located above the AAA<sup>+</sup>-ATPase and is fundamental for lid assembly [36]. The lid additionally has contact sites with the  $\alpha$ -subunits of the CP through the N-terminal regions of Rpn5 and Rpn6, which are assumed to act as a clamp that stabilizes the RP and CP interaction [32]. In contrast to the deubiquitylases Ubp6 and Uch37, which are known to cleave within ubiquitin chains, Rpn11 cleaves whole ubiquitin chains from the substrate and is therefore important for substrate processing and ubiquitin recycling [21], [37].

The base of the RP which forms the main contact sites between the RP and the CP is composed of the 10 subunits Rpt1-6, Rpn1, Rpn2, Rpn10 and Rpn13. The core of the base is built by six Rpt-subunits which belong to the family of AAA<sup>+</sup>-ATPases. They form a heterohexameric ring which is positioned on top of the  $\alpha$ -ring of the CP [38], [39], [40]. The architecture and function of the AAA<sup>+</sup>-ATPase ring is described in more detail in section 1.3.3. The largest subunits of the 26S proteasome, Rpn1 and Rpn2, are important

scaffolding and binding platforms for inter- and intra-protein networks. Rpn2 connects the base and lid complexes and interacts additionally with Rpn13. Rpn1 is known to be a binding platform for many transient proteasome interacting protein (PIPs) like Ubp6, Rad23, Dsk2 and Ddi1 [41]. Ubp6 is the most abundant PIP on the 26S proteasome. Additionally, Rpn1 was recently found to function as a ubiquitin receptor [42]. Both Rpn1 and Rpn2 share a common structural motif which forms a toroid-shaped structure. The toroid is built from eleven 35-40 amino acid repeats (proteasome/cyclosome (PC)-motives) which form a concentric ring of axial oriented  $\alpha$ -helices around two axially oriented  $\alpha$ -helices on the inside [43]. Apart from Rpn1, ubiquitin recognition by the 26S proteasome is mainly performed by the ubiquitin receptors Rpn10 and Rpn13 (Figure 1.4). They are both located at the distal end of the RP and serve as binding platforms for ubiquitylated substrates [43], [44], [45]. Whereas Rpn13 binds ubiquitin via a prou (pleckstrin-like receptor for ubiquitin) domain [44], Rpn10 binds ubiquitin via a ubiquitin-interacting motif (UIM) domain [46]. Ubiquitin recognition by the 26S proteasome is additionally regulated by different PIPs known as shuttle factors. Shuttle factors like Rad23, Ddi1 and Dsk2 contain a UIM domain, which binds ubiquitin, and a UBL (ubiquitin-like) domain which mediates binding to the 26S proteasome [44], [47], [48], [49], [50].

### 1.3.2 Conformational states of the 26S proteasome

The 26S proteasome is known to undergo major conformational changes, which depend on the nucleotide binding state and most likely reflect different substrate processing states. For the yeast 26S proteasome three different conformational states (s1, s2 and s3) have been reported [51] (Figure 1.5 A). In the presence of ATP the predominant conformation of the 26S proteasome is the s1 state [25], [26], [27], [51]. The s3 state is induced by a slowly-hydrolysable ATP analog ATP $\gamma$ S [30], whereas the s2 state is found in both samples in low abundance (Figure 1.5 B).

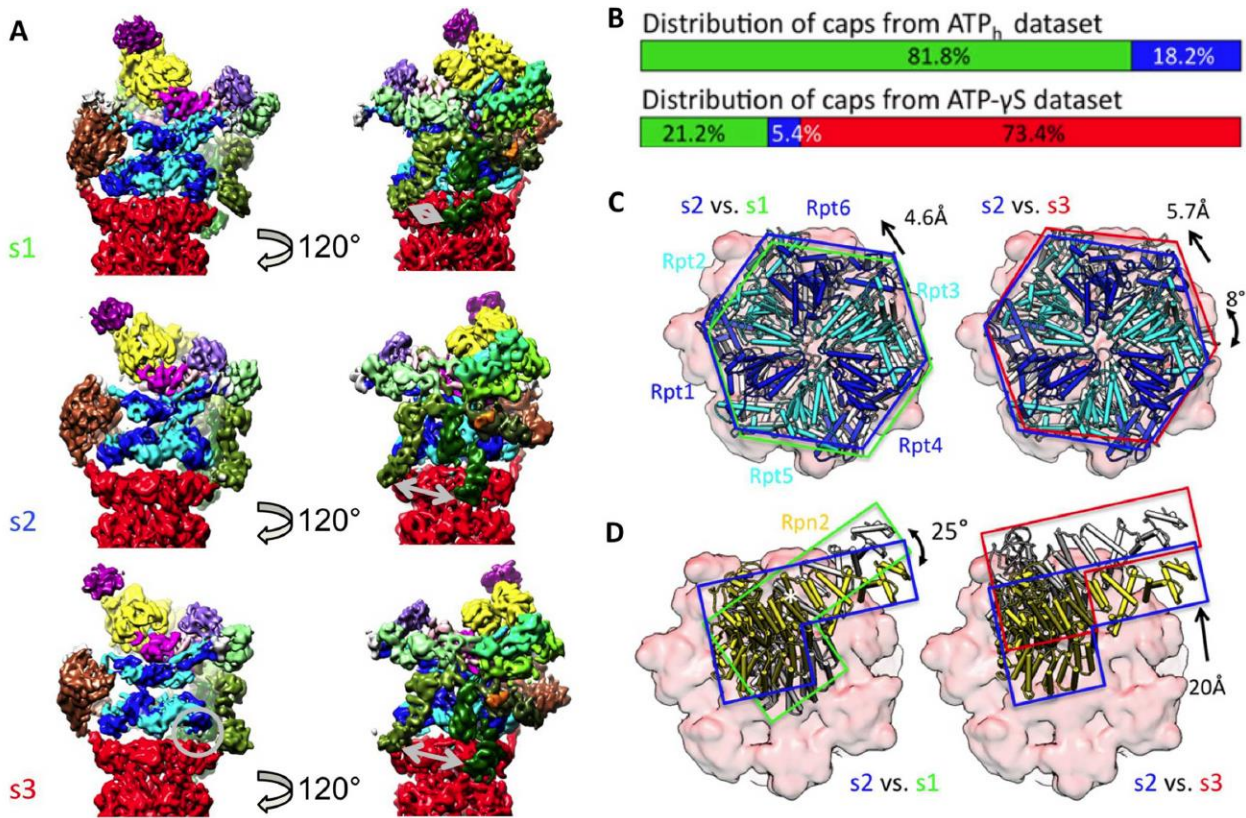


**Figure 1.5:** Conformational states of the yeast 26S proteasome. **(A)** 3D reconstructions of the 26S proteasome in the s1, s2 and s3 state colored in the color code of Fig. 1.3 according to the subunits. The main differences of the states are highlighted by gray arrows and circles. **(B)** Abundances of the states in different proteasome data sets. **(C)** Comparison of the AAA<sup>+</sup>-ring between the three states shown in the top view looking onto the ring. **(D)** Comparison of the position of Rpn2 within the three states. The CP is shown in light red (C & D). Figure taken with permission from [52].

The comparison of the three conformational states indicates that s2 is an intermediate conformation between s1 and s3. The main conformational differences can be described by shifts and rotations of the RP with respect to the CP or conformational changes of the lid and the ATPase subunits. From s1 to s2, the AAA<sup>+</sup>-ring shifts by approximately 5 Å (Figure 1.5 C) towards Rpn1, resulting in a coaxial alignment of the central channel of the AAA<sup>+</sup>-ring with that of the CP. In contrast, the lid undergoes a rotation of around 25° (Figure 1.5 D), which results in a longer distance between the N-terminal region of Rpn5 and Rpn6 (Figure 1.5 A). Additionally, the active site of the deubiquitylating enzyme Rpn11 locates closer to the entrance of the AAA<sup>+</sup>-ATPase channel. In contrast to the ground state (s1), the active site of Rpn11 is shifted by approximately 25 Å towards the central axis of the AAA<sup>+</sup>-ring in the s3 state [51], [53]. The N-terminal region of Rpn1 shifts towards the AAA<sup>+</sup>-ring and makes a contact with the subunit interface of Rpt6/2 in the s2 state. From s2 to s3, the lid subunits shift into the direction of Rpn1, as shown for Rpn2 in Figure 1.5 D. The AAA<sup>+</sup>-ring rotates by 8° and shifts by 5.7 Å to become fully aligned with the CP gate. In the s3 state, the central channels of the OB- and AAA<sup>+</sup>-ring are aligned with the central channel of the CP

[30], [51]. The ATPase ring forms a “lock washer” conformation, in which the helically-shaped ring is split at the interface of one of the nucleotide pockets (Figure 1.6 D) [30]. In addition to the shift and rotation of the AAA<sup>+</sup>-ring, each of the Rpt subunits undergoes a conformational change which results in a different position of the split site of the lock washer and height of the pore-1 loops as described in section 1.3.3. The s3 state, or an s3-like state, was also found in a study in which the proteasome was incubated with ATPγS or ubiquitylated substrates [29]. Considering the conformational differences of these three states, a functional model was proposed for the 26S proteasome. The s1 state is assumed to represent the ground state in which the proteasome is waiting for substrates. The s2 state might represent a commitment state where the proteasome starts to process the substrate and the s3 state was assigned to be the substrate-processing state, in which the polypeptide chain is unfolded by the ATPase and translocated into the CP to be degraded [51].

In an in situ study of structure and distribution of 26S proteasomes inside of neuronal cells, two states (s1 and s3) of the proteasome were identified. Taking into account the challenges of in situ structural biology and the resolution of this proteasome structure (~30 Å), the s2 state might be a short-lived state, which could not be identified in situ [31]. In a recent cryo-EM study, four different conformational states for the human proteasome were reported (S<sub>A</sub>, S<sub>B</sub>, S<sub>C</sub> and S<sub>D</sub>) which show similarities to the yeast states [54]. These studies confirmed that the conformational states observed in the yeast 26S proteasome are conserved in different species.

### 1.3.3 The AAA<sup>+</sup>-ATPase

Unfolding of proteasomal substrates is mediated by the Rpt subunits in an ATP-dependent fashion. They belong to the additional strand catalytic glutamate (ASCE) superfamily of ATPases and are composed of three domains. The N-terminal part is called OB domain, the middle part “large AAA<sup>+</sup> subdomain” and the C-terminal part “small AAA<sup>+</sup> subdomain”. The six Rpt subunits (Rpt1-Rpt6) form two stacked heterohexameric rings, the OB-ring and the AAA<sup>+</sup>-ring. They are positioned above the α-ring of the CP [55], [56] (Figure 1.6 A,B).

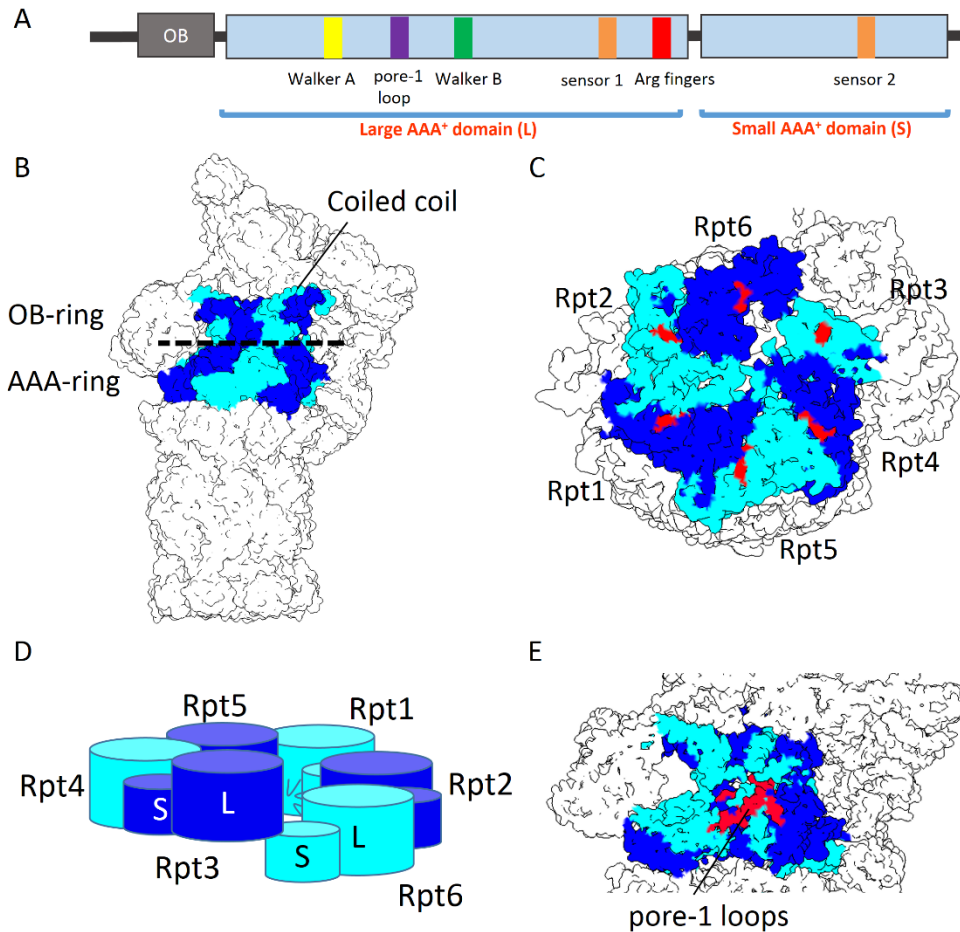


**Figure 1.6:** AAA<sup>+</sup>-ATPase of the 26S proteasome. **(A)** Architecture of the Rpt-domains of the 26S proteasome (adapted from [53]). **(B)** Three-dimensional structure and organization of the AAA<sup>+</sup>-ATPase within the 26S proteasome complex. **(C)** Slice-open view through the AAA<sup>+</sup>-ring at the position of the nucleotides. Nucleotide densities are marked in red. **(D)** Schematic representation of the staircase arrangement of the AAA<sup>+</sup>-ring in the s1 state showing the split site of the lock washer between Rpt3 and Rpt6 (adapted from [53]). **(E)** Slice-open view through the central translocation channel of the AAA<sup>+</sup>-ring. The pore-1 loops are colored in red.

Each Rpt subunit carries an  $\alpha$ -helical sequence at the very N-terminus of the OB-domain. The Rpt ring is composed of three dimers (Rpt1/2, Rpt6/3 and Rpt4/5) and two N-terminal  $\alpha$ -helices of the Rpt dimers twist around each other and form a coiled coil. The coiled coils interact with other subunits of the lid which stabilize the whole complex. The coiled coil of Rpt1/2 interacts with Rpn1. Different from the other coiled coils, the coiled coil of Rpt1/2 forms a kink in the middle probably due to the interaction with Rpn1. The coiled coil of Rpt3/6 interacts with Rpn2 and other lid subunits [26], [57]. The OB-ring is formed by the OB domains of the Rpt subunits and is positioned above the ring formed by the AAA<sup>+</sup> domains of the Rpt subunits. The deubiquitylating enzyme Ubp6 was shown to bind to the OB-ring [58]. The largest domain of the Rpt subunit is the AAA<sup>+</sup> domain. This domain carries conserved motifs necessary for nucleotide binding and hydrolysis and the aromatic pore-loops (pore-1 loop or Ar- $\phi$  loop), which are responsible for

substrate binding and protrude into the central channel of the AAA<sup>+</sup>-ring [27], [59]. The hydrolysis of ATP takes place in the nucleotide pockets which are formed by two neighboring Rpt subunits. The six nucleotide pockets of the 26S proteasome are located at the interfaces of Rpt3-4, Rpt4-5, Rpt5-1, Rpt1-2, Rpt2-6 and Rpt6-3. The topology of the AAA<sup>+</sup>-ring and the position of the nucleotide pockets is shown in Figure 1.6 C. Each Rpt subunit harbors the conserved motifs Walker A, Walker B, Arg-fingers, sensor 1 and sensor 2. The nucleotide is bound to a groove formed by the Walker A motif of the large domain of an Rpt subunit and coordinated by Arginine fingers of the clockwise adjacent Rpt subunit. The topology of the nucleotide pocket is similar to that of other members of the AAA<sup>+</sup>-ATPase family like ClpX, p97, NSF or CDC48 [60]. In the human proteasome structure, it was shown that the pockets are occupied with nucleotide densities. All pockets except for the Rpt6-3 pocket form a tight conformation and the nucleotides are coordinated by the adjacent Arg-fingers. In addition to the pocket distance which is larger in Rpt6-3, the nucleotide density is smaller in comparison to the other nucleotide densities. It was therefore concluded that Rpt6-3 binds ADP whereas the other pockets are occupied with ATP [57]. In the yeast proteasome, the split site of the lock washer of the s1 state is between Rpt6-3 and that of the s3 state is between Rpt5-1 [30].

The central channel of the AAA<sup>+</sup>-ATPase is lined by the pore-1 and pore-2 loops (Figure 1.6 E). They are responsible for substrate translocation through the channel into the CP [61]. The AAA<sup>+</sup>-ring of the proteasome in the ground state assumes a spiral staircase conformation with Rpt3 in the highest and Rpt6 in the lowest position (Figure 1.6 D, E). This results in different heights of the pore-1 loops in the central channel of the AAA<sup>+</sup>-ATPase ring with respect to the gate of the CP. Single molecule studies on the ATP-dependent caseinolytic protease X (ClpX) showed that the translocation of substrates is composed of a burst and a dwell phase. The hydrolysis of ATP occurs in the burst phase and is coupled to translocation of the polypeptide chain. During the dwell phase, ADP is exchanged for ATP to recover the ATPase subunit for the next round of ATP hydrolysis and substrate translocation [62]. As a consequence of nucleotide hydrolysis, the conformational change of the AAA<sup>+</sup>-ring causes the rearrangement of the heights of the pore-1 loops. In case of the proteasome, the staircase in the s3 state is rearranged in such a way that Rpt1 is in the highest and Rpt5 in the lowest position [30]. It is therefore assumed that substrate translocation in the proteasome is also coupled to the change of the staircase conformation, depending on the nucleotide state of the ATPase. So far, three different models have been proposed for the inter-subunit coordination of the conformational change of the ATPase coupled to ATP hydrolysis. The first model proposes a sequential hydrolytic cycle which proceeds successively through the ring. The second model proposes concerted hydrolysis and simultaneous conformational changes of all subunits. In the third



model proposed, each of the subunits independently hydrolyzes ATP in a stochastic manner [63], [64]. Although single molecule analysis of ClpXP supports a stochastic model [62], no mechanochemical model has been proposed for proteasome function.

The spiral staircase arrangement of the pore-1 loops of the proteasome has also been observed in other members of the ASCE family. For example, the helicase DnaB has a spiral arrangement of the DNA-binding loops in the substrate-bound crystal structure [65]. Similarly, the RNA-binding loops of the RecA type Rho helicase are arranged in a spiral staircase [66]. In contrast, the pore-loops of ClpX have a different organization in absence of substrate. Each half-ring shows a separate three-step staircase [67]. It was nevertheless not excluded that ClpX adopts a spiral staircase conformation similar to the proteasome in the presence of substrate [64]. In addition, the N-Ethylmaleimide-Sensitive Factor (NSF), which is a member of the AAA<sup>+</sup>-family, adopts a spiral staircase arrangement [68].

#### 1.3.4 The 20S core particle

The enzymatic digestion of polypeptide substrates, mediated by the proteasome, takes place in the catalytic chamber of the CP. The CP has a barrel-like structure, composed of four coaxially stacked heteroheptameric rings of  $\alpha$ - and  $\beta$ -subunits [69] (Figure 1.7).

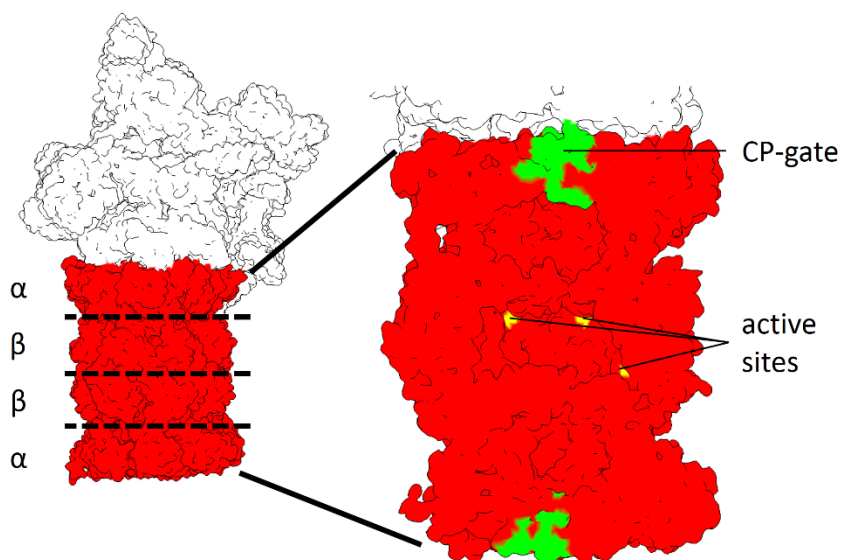


**Figure 1.7:** The 20S core particle is composed of four coaxially stacked heteroheptameric rings of  $\alpha$  and  $\beta$  subunits (left). The cut-open view (right) shows the CP-gate formed by N-terminal extensions of the  $\alpha$ -subunits (green). The catalytic active sites inside the catalytic chamber formed by the  $\beta$ -subunits are marked in yellow.

Among these subunits,  $\beta$ 1,  $\beta$ 2 and  $\beta$ 5 are catalytically active. During the assembly of the CP, the zymogen subunits become activated after cleavage of the propeptide. The catalytically active groups of the threonine-class proteases are the N-terminal  $\alpha$ -amino groups of threonine-1 [69], [70], [71].  $\beta$ 1,  $\beta$ 2 and  $\beta$ 5 have different specificities which are trypsin-like (basic residues in position P1), caspase-like (acidic residues), and chymotrypsin-like (hydrophobic residues), respectively. The CP is therefore able to digest a variety of different substrates [72]. These three active sites face the interior of the chamber formed by the  $\beta$ -rings. Self-compartmentalization is a hallmark of many intracellular proteases [73]. In order to regulate protein degradation, access to the catalytic chamber is controlled by the CP-gate, which is formed by the N-terminal extensions of the  $\alpha$ -subunits (Figure 1.7). In the closed form the  $\alpha$ -ring N-termini block the entry of substrates through the CP pore by extending in parallel to the plane of the  $\alpha$ -ring. In the open form, the N-termini undergo conformational changes and extend vertically to the  $\alpha$ -ring plane, thereby allowing substrates to enter. The gate opening is triggered by proteasome-activating proteins like Blm10 and the RP which bind to the CP [74], [75].

### 1.3.5 Regulator – CP interactions and opening of the 20S pore

The interaction of regulatory proteins with the CP is mainly mediated by C-terminal extensions of the regulator which interact with specific pockets formed by the  $\alpha$ -subunits of the CP [3], [74], [75]. The subunits Rpt2, 3 and 5 possess a conserved motif of a hydrophobic residue followed by a tyrosine residue and a residue of any kind (HbYX) which is known to interact with the  $\alpha$ -ring of the CP. This motif inserts into the intersubunit pockets of the  $\alpha$ -ring [75], [76]. In the published yeast proteasome structures, only the HbYX motifs of Rpt2 and Rpt3 were identified to tightly bind to the corresponding pockets, whereas the HbYX motif of Rpt5 seems to bind only transiently [26], [51], [75]. In all those structures the CP gate is in a closed conformation [26], [30], [51]. In the ground state of the human proteasome structure, the HbYX motifs of Rpt2 and Rpt3 were found to bind to the pockets and the gate of the CP is closed. In contrast, in the lowly abundant  $S_D$  state, five out of six C-terminal tails seem to interact with the CP of the proteasome and an open gate was observed [54], [57].

The archaeal proteasomal homolog proteasome-activating nucleotidase (PAN) [77] is responsible for the unfolding and translocation of substrates into the CP. The interaction of PAN with the CP is facilitated by the C-terminal amino acids which bind to the intersubunit  $\alpha$ -pockets. This interaction induces a rigid-body rotation of the  $\alpha$ -subunits which relocates a reverse-turn loop and stabilizes the open-gate conformation [78]. In contrast, the 11S activator PA26 possesses special activation loops which interact with the reverse

turn loops of the CP  $\alpha$ -subunits to stabilize gate opening independent of the interaction of the C-termini with the intersubunit pockets [79], [80]. The gate-opening mechanism of the 26S proteasome has not been well characterized yet. It remains to be shown whether the interaction of the HbYX motifs, together with other C-terminal amino acids of the Rpt subunits, is sufficient to induce an open-gate conformation or whether additional interactions are necessary to stabilize the open gate as observed with PA26.

## 2 Goal of the PhD thesis

Recent structural studies using single particle cryo-electron microscopy have revealed different coexisting conformations of the 26S proteasome [51]. Low resolution EM maps, however, hindered building accurate atomic models to understand mechanochemical function of the 26S proteasome. This work aims to gain deeper structural insights into the functional cycle of the proteasome. First, I applied SPA to the 26S proteasome in the presence of ATP, addressing the underlying mechanism of the conformational switch from s1 to s2 (Aim1). Second, I attempted to find additional low-abundance conformations using different nucleotides or nucleotide analogs focusing on the gate-opening mechanism of the 26S proteasome (Aim2).

(Aim1) All published high-resolution human proteasome structures adopt the s1 state or an s1-like conformation [54], [57], [81], [82]. I aimed at gaining high-resolution structures of the yeast 26S proteasome in the s1 and s2 state to allow us to build an accurate atomic model. The high-resolution EM maps would allow the construction of near-atomic models which would improve understanding of the 26S proteasomal function. For example six nucleotide densities inside the binding pockets of the AAA<sup>+</sup>-ATPase were reported for the human proteasome. The present study allowed to compare the molecular details of the nucleotide-binding pockets of the AAA<sup>+</sup>-ATPase of the yeast with the human proteasome.

(Aim2) In several high-resolution structures reported, the gate of the  $\alpha$ -rings that controls access to the catalytic chamber is closed. In the human s1 state, two out of three Rpt subunit HbYX motifs (Rpt3 and Rpt5) bind in the pockets of the  $\alpha$ -ring, indicating that docking of two HbYX motifs is not sufficient to open the CP gate [57], [81], [82]. Higher-resolution structures are needed for a precise mechanistic understanding of the gate opening. The second goal of this PhD thesis is to find low-abundance conformations of the yeast 26S proteasome by treatment with different nucleotides or nucleotide analogs. For this study, I applied ADP and the ATP analogs AMP-PNP and BeF<sub>x</sub> to the proteasome to find new conformations. The conformational landscape of purified ATP analog-treated proteasome complexes was investigated using cryo-EM SPA.

## 3 Materials and Methods

### 3.1 Materials

#### 3.1.1 Chemicals and consumables

Adenine	Sigma
Agarose	Sigma
Adenosine 5'-(3-thiotriphosphate) (ATP $\gamma$ S)	Roche
Adenosine diphosphate (ADP)	Sigma
Adenosine triphosphate (ATP)	Sigma
Adenylyl-imidodiphosphate (AMP-PNP)	Roche
Ammonium molybdate tetrahydrate	Sigma
ANTI-FLAG <sup>®</sup> M2 Affinity Gel (M2 beads)	Sigma
Ascorbic acid	Roth
Beryllium chloride	Sigma
Bio-Rad protein assay solution	Bio-Rad
Bovine serum albumin (BSA)	Sigma
Bacto yeast extract	BD
Bacto peptone	BD
Creatine phosphate (CPh)	Sigma
Creatine phosphate kinase (CPK)	Sigma
Dithiothreitol (DTT)	Merck
Ethane/Propane (37 % ethane / 63 % propane)	Linde
Ethylenedinitrilotetraacetic acid disodium salt dehydrate (EDTA)	Merck
3xFLAG peptide (DYKDHDGDYKDHDIDYKDDDDK)	MPI core facility
$\alpha$ -D(+) Glucose monohydrate	Roth
Glycerol 86-88%	Roth
Hydrochloric acid (HCl)	Merck
N-2-Hydroxyethylpiperazine-N'-2-ethanesulfonic acid (HEPES)	biomol
Magnesium chloride (MgCl <sub>2</sub> )	Merck
3-(N-Morpholino)propanesulfonic acid (MOPS)	Merck
NuPAGE <sup>®</sup> LDS Sample Buffer (4X)	ThermoFisher
N-succinyl-Leu-Leu-Val-Tyr-7-amino-4-methylcoumarin (Suc-LLVY-AMC)	bio-technie
Potassium antimonyl(III) tartrate hydrate (antimonyl tartrate)	Merck
Potassium dihydrogen phosphate	Roth
Tris Base	Sigma
SeeBlue <sup>®</sup> Plus2 Pre-stained Protein Standard	invitrogen
Sodium chloride (NaCl)	Merck
Sodium dodecyl sulfate	Roth
Sodium fluoride (NaF)	Sigma
Sucrose	Merck
Sulfuric acid	Sigma
Uranyl acetate (UA)	Merck

### 3.1.2 Buffers and solutions

All buffers and solutions were produced using deionized water from a Milli-Q Plus Ultrapure Water Purifier (dH<sub>2</sub>O).

#### **Buffer A**

50 mM Tris HCl, pH 7.4  
100 mM NaCl  
10% (vol/vol) glycerol  
10 mM MgCl<sub>2</sub>  
4 mM ATP  
25 mM CPh  
10 U/mL CPK

#### **Sucrose buffer (15%)**

20 mM HEPES, pH 7.4  
40 mM NaCl  
5 mM DTT  
10 mM MgCl<sub>2</sub>  
4 mM ATP  
16 mM CPh  
4.5 U/mL CPK  
15% (wt/vol) sucrose

#### **Sucrose buffer (45%)**

20 mM HEPES, pH 7.4  
40 mM NaCl  
5 mM DTT  
10 mM MgCl<sub>2</sub>  
4 mM ATP  
16 mM CPh  
4.5 U/mL CPK  
45% (wt/vol) sucrose

#### **ATP-containing reaction buffer**

50 mM HEPES, pH 7.4  
4 mM ATP  
10 mM MgCl<sub>2</sub>  
10% (vol/vol) glycerol

#### **ATPase activity assay color solution**

125 mM sulfuric acid  
0.5 mM ammonium molybdate  
10 mM ascorbic acid  
0.04 mM antimonyl tartrate

#### **20S activity assay solution**

100 mM HEPES, pH 7.4  
100 μM Suc-LLVY-AMC  
5 mM ATP  
10 mM MgCl<sub>2</sub>  
10% (vol/vol) glycerol

#### **MOPS running buffer**

50 mM MOPS, pH 7.7  
50 mM Tris Base  
0.1% (wt/vol) SDS  
1 mM EDTA

### 3.1.3 Cell culture media

All media were prepared using dH<sub>2</sub>O and sterilized by autoclave sterilization for 20 minutes at 120 °C.

#### YPD medium (liquid)

Bacto yeast extract	10 g
Bacto-peptone	20 g
1% (wt/vol) Adenine	2 mL
40% (wt/vol) Glucose	50 mL
dH <sub>2</sub> O	950 mL

#### YPD medium (solid)

Bacto yeast extract	10 g
Bacto-peptone	20 g
Agar	20 g
1% (wt/vol) Adenine	2 mL
40% (wt/vol) Glucose	50 mL
dH <sub>2</sub> O	950 mL

### 3.1.4 Strains

*Saccharomyces cerevisiae* YYS40 (*MATa rpn11::RPN11-3XFLAG-HIS3*)

## 3.2 Methods

### 3.2.1 Yeast cell culture

For a liquid cell culture, YYS40 yeast cells, which were stored as glycerol stocks, were streaked onto YPD plates and incubated at 30 °C until visible colonies appeared. One colony was inoculated in 5 mL YPD liquid medium, which was incubated overnight at 30 °C in a spinning wheel. The overnight culture was diluted in 100 mL YPD medium and cultured overnight in a horizontal shaker with 200 rpm at 30 °C. 20 mL of the overnight 100 mL-culture was inoculated into the final 1 L YPD culture in a baffled flask, which was incubated for 48 h in a horizontal shaker with 200 rpm at 30 °C. The cells were harvested by centrifugation using a Sorvall centrifuge equipped with a JA-10 rotor at 1,000×g. The pellet was washed with water twice and cells were kept at -80 °C until further use.

### 3.2.2 Proteasome purification

The yeast cell pellet was diluted with buffer A at a ratio of 1 g of cells to 1 mL of buffer. Cells were disrupted using Zirkonium glass beads in a glass bead mill (Vibrogen-Zellmühle Vi4; Edmund Bühler, Tübingen). The bead mill was cooled at 4 °C and cells were disrupted with three agitation cycles (35 sec on, 5 min off). The cell lysate was separated from the beads by centrifugation using an in house-made filter unit. The crude

extract was separated from cell debris by centrifugation in a Sorvall centrifuge for 30 min at 43,000×g and 4 °C. Subsequently the crude extract was filtered using a MCE-membrane syringe filter with a pore size of 0.8 μm. The pH of the crude extract was adjusted to pH 7.4 using Tris base. FLAG-tagged proteasomes were purified by immunoprecipitation using M2 beads (Sigma). The filtered crude extract was incubated with the resin for 1.5 h at 4 °C (1 mL of resin per 40 mL of crude extract). Unbound proteins were washed out twice with buffer A. The proteasome was eluted using 200 μg/mL 3×FLAG-peptide in buffer A. The eluate was concentrated by centrifugation in Amicon spin columns (10-kDa molecular weight cutoff). To further purify double-capped proteasomes, the concentrated eluate was applied to a sucrose gradient (15–45% sucrose buffer) and centrifuged for 17 h at 208,000×g at 4 °C in a Beckman SW41 rotor. The sucrose gradient was generated using a Gradient Station ip (Biocomp). To obtain proteasome samples with different ATP analogs, ATP and the ATP-regenerating system of the sucrose gradient buffer were replaced with 2 mM ADP, 2 mM AMP-PNP, or 2 mM ADP/2 mM BeF<sub>x</sub>, respectively. BeF<sub>x</sub> was obtained by mixing NaF with BeCl<sub>2</sub> [2:1 (wt/wt)]. To get proteasomes with ATP and BeF<sub>x</sub>, the proteasome sample containing ATP was incubated with 5 mM BeF<sub>x</sub> after sucrose gradient centrifugation. The sucrose gradient was fractionated into 500 μl fractions using the Gradient Station ip. All samples were stored at –80 °C after snap freezing in liquid nitrogen.

### 3.2.3 Analytical methods

#### 3.2.3.1 Determination of protein concentration using Bradford

The protein concentration was determined as described by Bradford [83]. For the measurement, 200 μL of Bio-Rad protein assay solution were mixed with 800 μL of sample and incubated for 5 min at room temperature. The OD<sub>595</sub> was determined using a photometer (Ultrospec III; Pharmacia) in plastic cuvettes using buffer as a reference. First a calibration curve was determined using samples ranging from 0 to 10 μg/mL BSA in 100 mM HEPES pH 7.4. The concentration determination of an unknown protein solution was done accordingly using the calibration curve.

#### 3.2.3.2 Discontinuous polyacrylamide gel electrophoresis (SDS-PAGE)

For SDS-PAGE, 15 μL of sample were incubated with 5 μL of NuPAGE® LDS Sample Buffer (4x) for 5 min at 70 °C. Gel electrophoresis was performed at 150 V until the bromophenol blue band reached the lower end of the 4-12% Bis-Tris gel (NuPAGE® Novex). The gel was washed three times with water for 10 min



before staining for 60 min using PAGE Blue™ protein staining solution (Fermentas). The gel was unstained with water before digitalization with a Chemocam Imager (Intas).

#### 3.2.3.3 20S proteasome activity assay

The 20S proteasome enzymatic activity of sucrose fractions was screened using Suc-LLVY-AMC. After cleavage from the peptide, AMC, which absorbs at 360 nm, shows fluorescence at 460 nm which is used to quantify proteolytic cleavage. 10 µL of sample were mixed with 90 µL 20S activity assay solution in a 96-well plate and the change of fluorescence (FU) was monitored for 60 min using a FLUOstar Optima (BMG Labtech). The slope (FU/sec), corresponding to the 20S activity, was calculated within the linear part of the progress curve.

#### 3.2.3.4 ATPase activity assay

To estimate the inhibition of the proteasomal AAA<sup>+</sup>-ATPase by different ATP analogs, the hydrolysis rate of ATP was measured using the colorimetric assay described by Bartolommei et al. [84]. The measurement was calibrated using different KPO<sub>4</sub> concentrations from 0 to 500 µM in 50 mM HEPES (pH 7.4) and 10% (vol/vol) glycerol. 100 µL of sample was incubated with 900 µL of color solution for 35 min at room temperature and the OD<sub>850</sub> was determined with a photometer (Ultrospec III; Pharmacia) in plastic cuvettes using buffer as a reference. The proteasome ATPase activity was measured in ATP-containing reaction buffer over 90 min at 30 °C. The phosphate concentration was determined at different time points using the same method as for the KPO<sub>4</sub> calibration curve. For each time point 100 µL samples (20 µM proteasome) were taken and analyzed. The inhibition of the AAA<sup>+</sup>-ATPase by BeF<sub>x</sub> was determined by measuring the ATP hydrolysis rate after addition of BeF<sub>x</sub> to the reaction buffer. For AMP-PNP and ATPγS, the ATPase activity was measured using the sample purified in the presence of 2 mM AMP-PNP or 2 mM ATPγS, respectively.

#### 3.2.3.5 Mass spectrometry

The abundances of proteasome subunits in fractions of the sucrose gradient was determined with a label-free intensity-based absolute quantification mass spectrometry approach (iBAQ) [85]. All mass spectrometry (MS) analyses were carried out by the Core Facility of the Max Planck Institute.

#### 3.2.4 Electron microscopy

The approach used in this study to obtain structural information of the 26S proteasome is called single particle analysis (SPA) cryo-EM. Purified protein complexes of interest are vitrified and subsequently imaged with a transmission electron microscope. Thousands of cryo-EM images (micrographs), showing different views of single molecules, are subsequently used to automatically identify particles, sort them into different classes according to their structural differences, and finally reconstruct them to get high-resolution electron density maps. The maps obtained are the basis for modelling techniques which generate near-atomic resolution models.

The basic principle of an electron microscope is quite similar to that of a light microscope. The schematic arrangement of an electron microscope is shown in Figure 3.1.

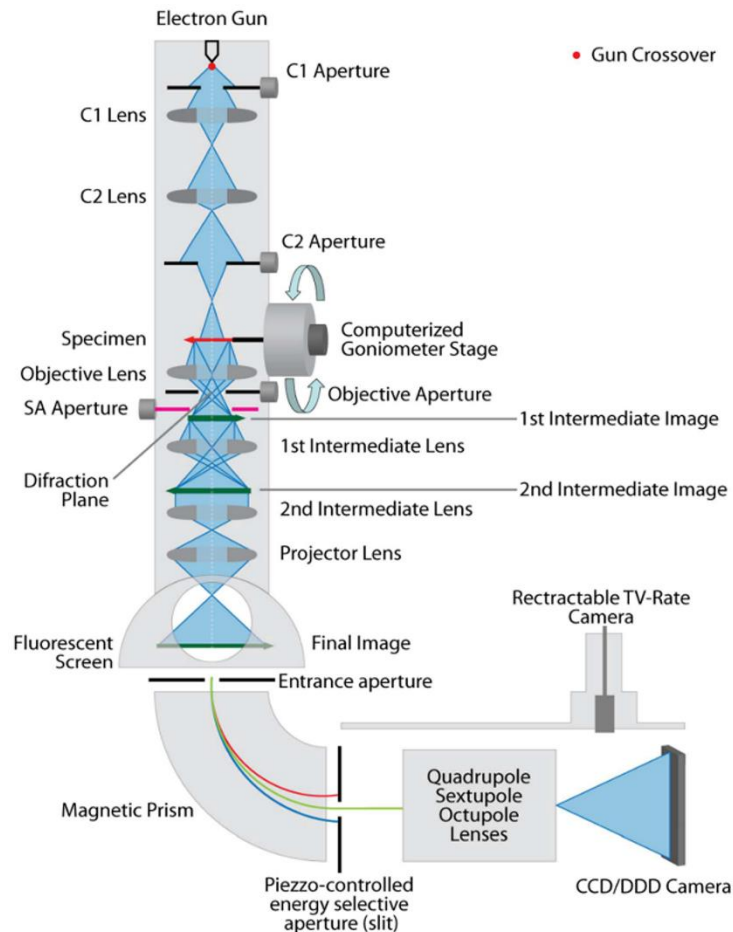


Figure 3.1: Schematic arrangement of an electron microscope. Figure taken with permission from [52].

At the tip of a modern electron microscope the electron beam is generated using a field emission gun (FEG). The voltage used to accelerate the electrons is 120-300 kV. A system of electromagnetic lenses is used to focus the beam on the sample and subsequently magnify the resulting image. The sample is inserted into the microscope using a computerized goniometer, which allows precise adjustment of the x-y- and z-coordinates and additionally to tilt the sample up to 70°. To improve the image quality, inelastic scattered electrons can be filtered through an energy filter. The final image is nowadays recorded on a direct digital detector, which allows the detection of single electrons with a very high detective quantum efficiency (DQE) and therefore improves the SNR of the images. Additionally DDD cameras have a very fast readout speed and are able to capture several subframes for one image. This allows for alignment of the frames of an image and, therefore, compensation for beam induced motion of the sample [86], [87], [88], [89].

#### 3.2.4.1 Sample preparation

To analyze biological molecules by electron microscopy the sample needs to be prepared in a way that it can be exposed to the vacuum inside the column of an electron microscope. Samples can either be stained with heavy metal salts like uranyl acetate or ammonium molybdate or embedded in vitreous ice. The cryogenic (“cryo”) sample preparation preserves a close to native state and is the method of choice in order to yield high-resolution reconstructions of biological samples. Cryo-fixation also captures structural heterogeneity of biological macromolecules, which can be analyzed by image classification techniques and gives insights into conformational dynamics of the sample [90].

##### 3.2.4.1.1 Negative Stain

For the preparation of negative stain-EM grids, 5  $\mu\text{L}$  of sample (approximately 100  $\mu\text{g}/\text{mL}$ ) was adsorbed onto a glow discharged carbon coated copper grid (Athene Grids, 400  $\times$  400 mesh) for 45 sec. Excess solution was removed and the grid was washed with 5  $\mu\text{L}$  of  $\text{H}_2\text{O}$  twice before stained for 45 sec with 5  $\mu\text{L}$  uranyl acetate [(2% in  $\text{H}_2\text{O}$  wt/vol)]. Excess staining solution was removed and the grid was dried at room temperature for at least 30 min before electron microscopy.

##### 3.2.4.1.2 Plunge freezing

For cryo-EM, the samples were plunge-frozen using a Vitrobot<sup>TM</sup> Mark IV (FEI) with 95% humidity, 4  $^\circ\text{C}$ , blot force 10 and blot time 10 sec. Carbon coated copper grids (Quantifoil 2/1, lacey carbon) were glow discharged for 15 sec and 5  $\mu\text{L}$  of sample was adsorbed for 30 sec. Excess solution was blotted using a filter paper and the grid was subsequently washed with 5  $\mu\text{L}$  of  $\text{H}_2\text{O}$  before rapid plunge-freezing in liquid ethane/propane. Until microscopic investigation grids were stored in liquid nitrogen.

##### 3.2.4.2 Negative stain EM

Negatively stained grids were analyzed with a Philips CM200/FEG electron microscope at 160 kV acceleration voltage. Images were acquired with a TVIPS CCD camera (4096  $\times$  4096 pixel) at a pixel size of 2.16  $\text{\AA}$  at specimen level. The nominal defocus varied from 2.5 to 3.0  $\mu\text{m}$ .

### 3.2.4.3 Cryo-EM data acquisition

Cryo-EM datasets were acquired with a Titan Krios (FEI) electron microscope equipped with a direct electron detector in an automated fashion. The acceleration voltage was 300 kV and movies were acquired either with EPU (Falcon cameras) or TOM<sup>2</sup> [91] (K2 camera), at a pixel size of 1.35 Å (Falcon) or 1.38 Å (K2) at specimen level, respectively. The total dose was  $\sim 45 \text{ e}^{-}\text{Å}^{-2}$ , which was distributed over 7 frames for Falcon II, 24 frames for Falcon III and 20 frames for movies acquired with the K2 camera. The nominal defocus varied from 1.5 to 3.5  $\mu\text{m}$ . All movies acquired with the K2 camera were corrected for anisotropic magnification distortion using the software “mag\_distortion\_correct” [92].

### 3.2.5 Image processing

Acquired movie frames of each image were aligned translationally and summed with an in-house implementation of the algorithm from the study by Li et al. [93]. The summed images of the aligned movie frame stacks were used for further processing. The CTF of the micrographs was determined with the software CTFFIND 3 [94] and micrographs with a CTF fit score below 0.05, as well as a defocus outside the range of 0.8-3.5  $\mu\text{m}$  were discarded. Table 3.1 summarizes the number of micrographs which were used for single particle analysis.

**Table 3.1:** Summary of the number of micrographs retained after image processing

Dataset	Camera	Micrographs
ATP	K2	66,462
ATP/BeF <sub>x</sub>	Falcon II	11,121
ADP-BeF <sub>x</sub>	Falcon III	6,522
AMP-PNP	Falcon II	3,304
ADP	Falcon II	5,732
ADP	Falcon III	6,136

### 3.2.6 Single particle analysis

#### 3.2.6.1 Principles of single particle analysis

Three dimensional reconstructions of macromolecular complexes, like proteins, can be obtained from micrographs using SPA and single particle reconstruction (SPR) techniques. An ideal micrograph of a protein complex contains several copies of the same molecule randomly oriented, covering all possible orientations of the molecule. These two-dimensional (2D) projections of the protein complex (“particles”) can be extracted from the micrograph using automated particle identification procedures. Because of the dose-sensitivity of biomolecules, a very low dose ( $\sim 20 \text{ e} \text{ \AA}^{-2}$ ) is used to acquire the micrographs. The SNR is therefore quite low, which means the signal of a particle is in a similar range as the background noise of the micrograph. In order to boost the signal, several 2D projections showing the same orientation of the particle are averaged. A 3D reconstruction is then computed from the 2D projections of several thousand particles. The higher the signal and homogeneity of the particles, the higher the resolution of the final reconstruction [95], [96], [97], [98].

The projection-slice theorem describes the basis for the 3D reconstruction of 3D objects from their 2D projections (Figure 3.2). According to the projection-slice theorem, each 2D projection corresponds to a slice of the object in Fourier space [97], [99].

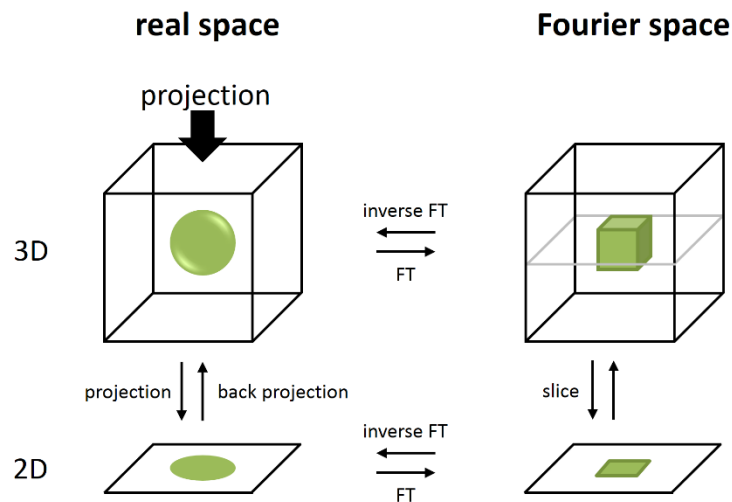


**Figure 3.2:** Projection-slice theorem. The projection of a 3D object in real space corresponds to a slice of the same object in Fourier space. Objects can be transformed from real space to Fourier space and vice versa using Fourier transformation (FT) and inverse FT, respectively.

In order to reconstruct a 3D volume from the Fourier transform, projections from all possible directions are necessary, which sample the object in Fourier space. The projection direction of each particle has to be determined in an optimization based alignment of the particles to their corresponding projection of the

3D object. During the alignment procedure, the three Euler angles  $\phi$ ,  $\psi$  and  $\theta$  and the x- and y- shifts are determined. The most commonly used alignment in SPA is “projection matching” [90], [96], [100], [101]. During projection matching, all particles are compared to projection images of a reference in different angles using cross correlation. Based on the cross correlation values the particles are assigned to a certain projection reference using maximum likelihood (ML) algorithms. ML assigns the particles to a projection with a certain probability. Ideally the probability converges during iterative rounds of projection matching refinement to the correct projection of the 3D object. During the first iteration a reference is needed which is used to generate the projections. Because the angle of the projection direction the particles are assigned to is known, it is then possible to reconstruct a 3D volume from the particle dataset. The steps, projection of a 3D volume, assignment of the particles to the projections and 3D reconstruction from the particles using the determined angles and shifts is done iteratively to improve the result [102], [103]. The final resolution of the 3D reconstruction mainly depends on the signal and orientations of the particles of a data set.

The sample preparation for cryo-EM allows the particles to move freely in solution before freezing. As a consequence, structural flexibility of macromolecular complexes is conserved, which means that the single particle data set can be quite heterogeneous. Each particle has to be assigned not only to the parameters needed for 3D reconstructions but additionally to a different structural conformation of the protein complex. It is therefore challenging to determine if a 2D projection of a protein belongs to the same conformation [98]. New image classification approaches nowadays allow to classify a data set in 2D and 3D to sort structural heterogeneity of a protein complex. Thereby SPA can be used not only to get the 3D reconstruction of a protein, but also to understand the dynamics of the complex [104].

### 3.2.6.2 Single particle analysis of the 26S proteasome

Micrographs were subjected to automated localization of 26S proteasome particles by cross-correlation analysis of template projections using the TOM toolbox as described in Beck et al. [26]. Particles were sorted by iterative 2D classification in order to remove false positive hits. All further single-particle analysis was performed with the software package RELION [103]. 2D-sorted proteasome particles were extracted with a box size of  $384 \times 384$  pixels for K2 datasets and  $416 \times 416$  pixels for Falcon datasets. Particles were resized to a box size of  $256 \times 256$  pixels and subjected to iterative reference-free 2D classification. 2D classes containing high quality particles were additionally sorted into single-capped (sc26S) and double-

capped 26S proteasomes (dc26S) according to their 2D class averages. The number of sc26S and dc26S particles and the results of the 3D classification for each dataset are summarized in Table 3.2.

**Table 3.2:** Summary of number of particles used for single particle analysis (taken from [105])

Dataset	sc26S	dc26S	s1	s2	s3	s4	Not well defined
ATP	196475	194803	286534	193337	-	-	106210
ATP/BeF <sub>x</sub>	20325	119023	52335	67747	25376	23228	89685
ADP-BeF <sub>x</sub>	75323	109021	121560	58156	44347	4397	73135
AMP-PNP	5680	40709	-	-	67522	-	19576
ADP	32821	49434	-	-	-	-	131689

Single particle analysis was done as described in Wehmer et al. [105] with the help of Dr. Antje Aufderheide (MPI biochemistry). In brief, initial 3D structures of sc26S and dc26S particles were reconstructed. The reconstructed particles exhibited an uneven angular distribution. For data sets with particle numbers larger than 500,000 (sc26S and psc26S), particles, that score worst in terms of the `_rlnMaxValueProbDistribution` value in RELION, from angular classes with an above-average occupancy were removed. Particles were subjected to particle polishing. The broken C2 symmetry of dc26S particles was addressed by in silico separation of the RPs as described in Unverdorben et al. [51] to obtain RPs of dc26S particles (pseudosc26S/psc26S). Sc26S and psc26S particles were classified using a soft-edged mask on the RP and the 3D class averages were compared to the previously identified proteasome states s1, s2 and s3 [51]. Psc26S and sc26S particles showing the same conformational state were combined, refined and post-processed using RELION to obtain final reconstructions. The resolution of the resulting final reconstruction was assessed by Fourier shell correlation (FSC<sub>0.143</sub>) using the gold-standard method as described in Chen et al. [106].

### 3.2.7 Model-building and analysis

Model-building was done together with Dr. Till Rudack (Ruhr University) as described by Wehmer et al. [105]. In brief, the initial models were obtained by comparative and de novo modeling. The merged structure of the CP crystal structure (PDB-ID: 5cz4 [107]) and the RP homology model based on the human structure (PDB-ID: 5l4g [57]) were used as initial structure for the s1 state. The subunits were positioned into the EM map and subsequently refined. First real space refinement was performed as described in [108] using molecular dynamics flexible fitting (MDFF) [109] and then in reciprocal space. MDFF



simulations were prepared using QwikMD [110], analyzed with VMD [111], and carried out with NAMD [112]. The refined final structure of s1 was used to initiate an MDFF run into the density of the s2 state. The final refined structure of the s2 state was fitted through MDFF into the density of the s3 state, and the final s3 state structure was finally fitted into the s4 density.

Rpn13 modeling was done together with Florian Beck (MPI biochemistry) as described by Wehmer et al. [105] performing an exhaustive 6D correlation scan using the EM map of the best resolved class of a classification with a spherical mask on the RP.

Analysis of models was done with University of California at San Francisco (UCSF) Chimera. Images were rendered using UCSF Chimera. Model analysis was done together with Florian Beck and Dr. Antje Aufderheide.

## 4 Results

The following results have to a large extent been published by Wehmer et al. [105] and were obtained in collaboration with the co-authors. In detail, biochemical work was done by Marc Wehmer. Electron microscopy was done by Marc Wehmer with the help of Günter Pfeifer (MPI biochemistry). Image processing, single particle and model analysis was done by Marc Wehmer with the help of Florian Beck and Dr. Antje Aufderheide. Model building was done by Dr. Till Rudack with the help of Marc Wehmer and Dr. Antje Aufderheide.

### 4.1 Purification of the yeast 26S proteasome

The yeast 26S proteasome was purified in two steps: 1) affinity purification via FLAG-tagged Rpn11 and 2) sucrose gradient to enrich dc26S. Figure 4.1 A shows the elution profile of the sucrose gradient. The fractions with the highest protein concentrations were found in a range of fraction number 9 to 12, which corresponds to a sucrose concentration of approximately 26-30% (Figure 4.1 A). The concentration of fraction 11, which shows the highest 20S activity (Figure 4.1 B), was approximately 1.0 mg/mL, as estimated by Bradford assay. The negative stain analysis of fraction 11 (Figure 4.1 C) shows the assembly state of the proteasome (single or double capped 26S proteasome). The proteasomes are observed in different orientations on the carbon film (top view and side view). Similar orientation and assembly state of the proteasomes were observed in the cryo-EM image of this sample (Figure 4.1 D).

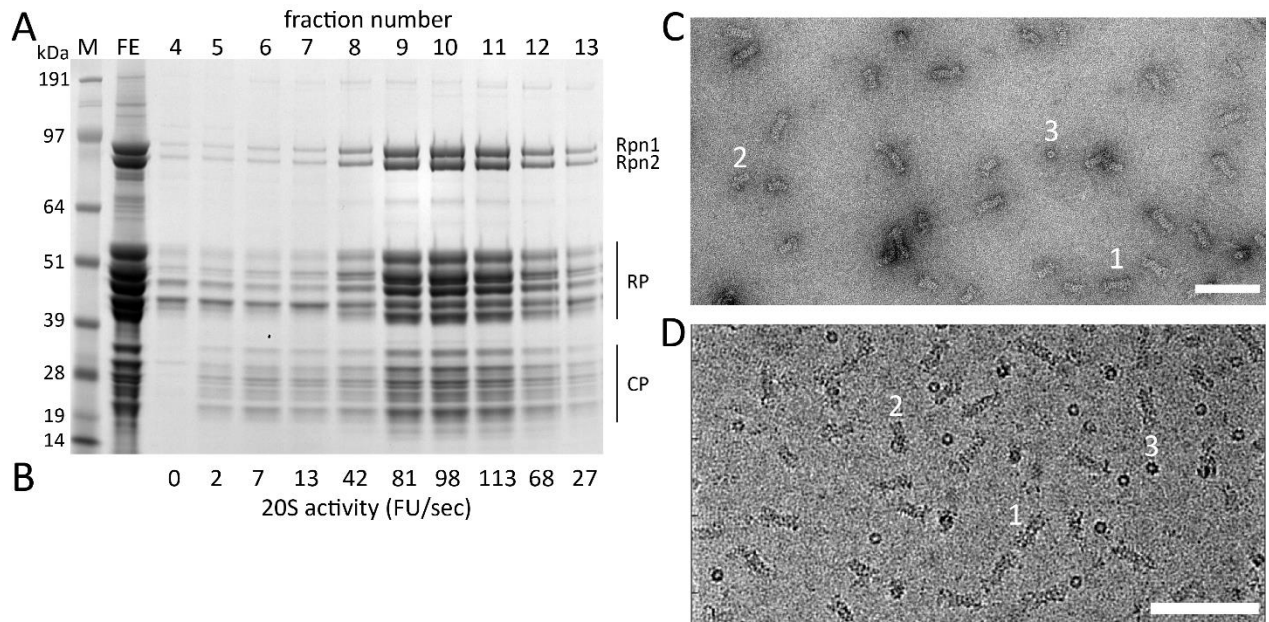


**Figure 4.1:** Purification of the 26S proteasome in the presence of ATP (adapted from [105]). **(A)** SDS-PAGE gel (CBB staining) of the concentrated FLAG eluate (FE), fractions of the sucrose gradient (4-13) and molecular weight marker (M). The bands of the subunits Rpn1, Rpn2, RP subunits and CP subunits are indicated. **(B)** 20S activity of the fractions from (A). **(C)** Negative stain EM image of fraction 11 from (A) diluted to  $\sim 100 \mu\text{g/mL}$ . Scale bar 100 nm. **(D)** cryo-EM image of *S. cerevisiae* 26S proteasome after sucrose gradient. Scale bar 100 nm. Double-capped side views (1), single-capped side views (2) and top views (3) of the proteasome are indicated in (C) and (D).

Proteasome in the presence of ADP, AMP-PNP and ADP-BeF<sub>x</sub> was purified in the same way as with ATP, replacing the ATP and ATP regeneration system by the ATP analogs during the sucrose gradient. The biochemical features of the proteasome purified in the presence of AMP-PNP and ADP-BeF<sub>x</sub> were similar to the results of the purification in the presence of ATP. In contrast, the sucrose gradient elution profile of the proteasome in the presence of ADP distributed in fractions with lower sucrose concentrations, indicating a higher percentage of single capped proteasomes (Figure 4.2 A). This result was confirmed by negative stain EM (Figure 4.2 B) and cryo-EM, which showed a higher percentage of single-capped and “broken” 26S proteasome particles in the presence of ADP.

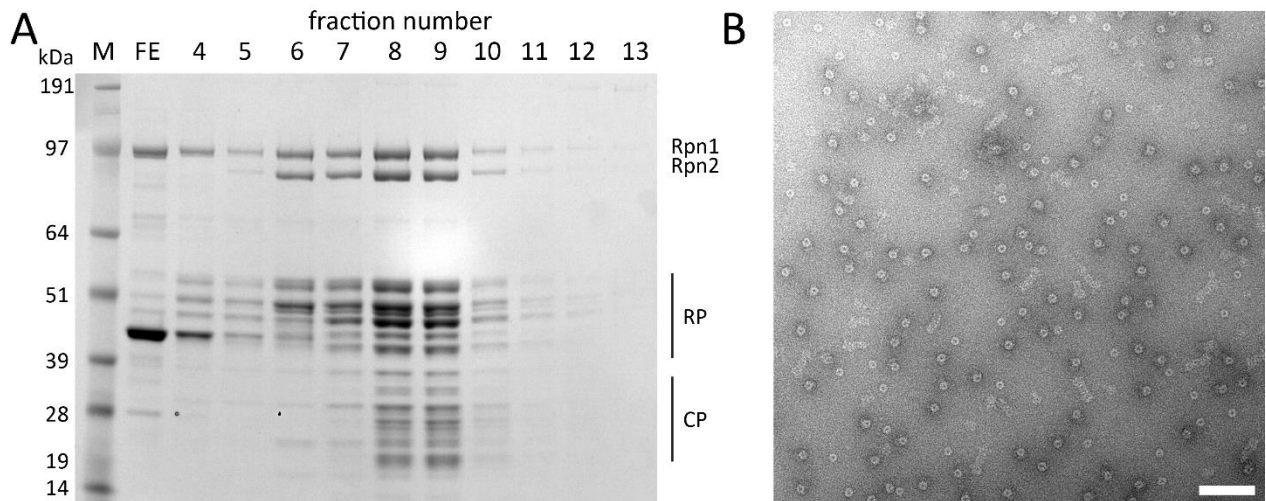


**Figure 4.2:** Purification of the 26S proteasome in the presence of ADP. **(A)** SDS-PAGE gel (CBB staining) of the concentrated FLAG eluate (FE), fractions of the sucrose gradient (4-13) and molecular weight marker (M). The bands of the subunits Rpn1, Rpn2, RP subunits and CP subunits are indicated. **(B)** Negative stain EM image of proteasome purified in presence of ADP. Scale bar 100 nm.

The subunit composition of the purified proteasomes was analyzed by a label-free intensity-based absolute quantification MS approach (iBAQ) (Figure 4.3). Overall, the occupancy of the subunits is not stoichiometric. Some subunits like Sem1, Rpn13 and Ubp6 are only present in 30% of the complexes. It was reported that the low abundance of Sem1 in MS analysis results from the small size of the protein [113]. The lid subunits have a lower abundance than the CP and ATPase subunits which might indicate that some of the purified complexes have disassembled. This analysis additionally shows that the use of the ATP analogs AMP-PNP and ADP did influence the abundances of single subunits in the samples. The largest difference was observed for the subunit Rpn1 which was present in the ATP sample in stoichiometric amounts and reduced by approximately 35 % in the samples with AMP-PNP and ADP.

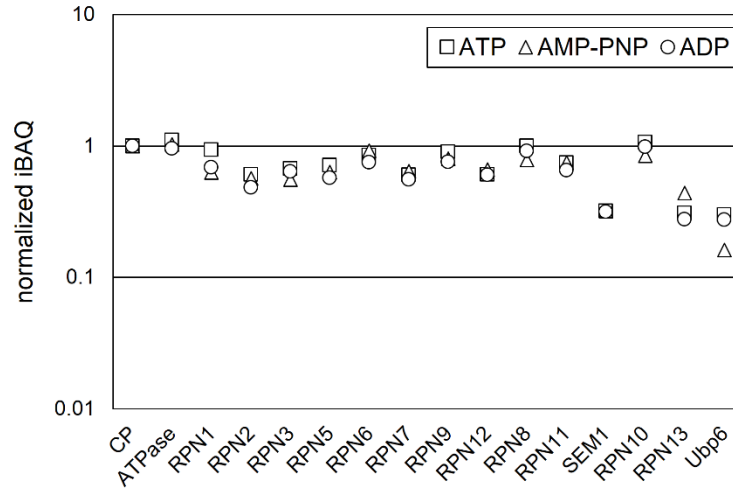


**Figure 4.3:** iBAQ analysis of the purified 26S proteasome in the presence of ATP, AMP-PNP and ADP. The iBAQ values were normalized to the average iBAQ of the subunits of the CP. CP and ATPase subunits are shown as an average.

#### 4.2 ATPase activity in the presence of nucleotide analogs

To analyze the influence of ATP analogs on the  $\text{AAA}^+$ -ATPase of the 26S proteasome, the ATPase activity was analyzed (Figure 4.4). This assay detects the free inorganic phosphate which is cleaved from ATP during hydrolysis by the proteasomal ATPase. While 2 mM  $\text{BeF}_x$  inhibited the ATPase activity at approximately 60%, 5 mM  $\text{BeF}_x$  resulted in 90% inhibition which is similar to the result obtained with 2 mM ATP $\gamma$ S (Figure 4.4 A). Although AMP-PNP is a non-hydrolysable ATP analog like ATP $\gamma$ S, only 20% of the activity was inhibited by 2 mM AMP-PNP (Figure 4.4 B). We confirmed that AMP-PNP itself was not cleaved by the 26S proteasome (Figure 4.4 B). In addition, detectable release of inorganic phosphate due to the auto-hydrolysis of neither AMP-PNP nor ATP was observed in the absence of the proteasome. A lower affinity for AMP-PNP than for ATP may hinder the precise measurement of the ATPase activity in the presence of AMP-PNP. Based on the results, either 5 mM  $\text{BeF}_x$  or 2 mM AMP-PNP were used for cryo-EM data acquisition.

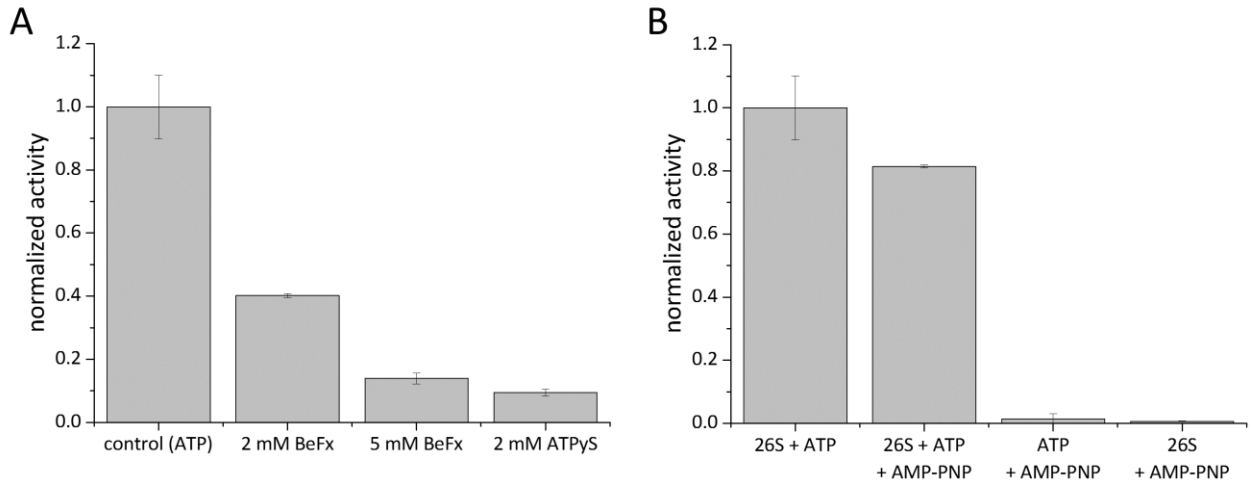


**Figure 4.4:** ATPase activity assay of the 26S proteasome in the presence of ATP analogs (adapted from [105]). **(A)** ATPase activity of the 26S proteasome was monitored by measuring the hydrolysis of ATP in the presence of the ATP analogs ATP $\gamma$ S and BeF $_x$  at different concentrations. The activity was normalized to the control sample, which contained only ATP. **(B)** ATPase activity in the presence of 2 mM AMP-PNP (26S + ATP + AMP-PNP) normalized to the control (26S + ATP). Auto-hydrolysis of 2 mM AMP-PNP (ATP + AMP-PNP) and hydrolysis of 2 mM AMP-PNP by the 26S proteasome (26S + AMP-PNP) were determined.

### 4.3 Cryo-EM reconstruction of the 26S proteasome in the presence of ATP

To obtain a cryo-EM reconstruction of the 26S proteasome in the presence of ATP, a data set of 66,462 micrographs was collected with a Titan Krios electron microscope (Figure 4.5 A). After automated particle location, ~1.5 Mio presorted proteasome particles were subjected to reference-free 2D classification. The classification resulted in 269,853 dc26S and 419,463 sc26S particles (Figure 4.5 B). The 3D reconstructions of the particles showed an uneven angular distribution (Figure 4.5 C and D), which limits the final resolution [57]. In order to reduce computational time, we decreased the size of the dataset by discarding particles from angular classes with an above-average occupancy (Figure 4.5 C and D). The resultant 196,475 sc26S and 194,803 dc26S particles were polished and refined as described in section 3.2.6 (Figure 4.5 E). To address the broken C2 symmetry of dc26S, the particles were *in silico* separated into two psc26S. Both sc26S and psc26S particles were classified separately in 3D using a spherical mask on the RP (Figure 4.5 F and G). From 389,606 psc26S particles, 52% of particles adopt the s1 state, 37% the s2 state, whereas 11% could not be assigned to any known state. The class averages of these particles did not show a well-defined proteasome structure and were therefore referred to as “broken” particles. From the sc26S particles, 42% were assigned to the s1 state, 26% to the s2 state and 32% were broken. All s1-like sc26S (83,007) and psc26S particles (203,527) were combined and reconstructed using auto-

refinement. The final resolution of the 3D reconstruction was 4.1 Å according to the  $FSC_{0.143}$  criterion (Figure 4.5 H and Figure 4.6 A). In the same way, s2-like particles (50,066 sc26S and 143,371 psc26S) were reconstructed. The final resolution of the 3D reconstruction was 4.5 Å (Figure 4.5 I and Figure 4.6 B).

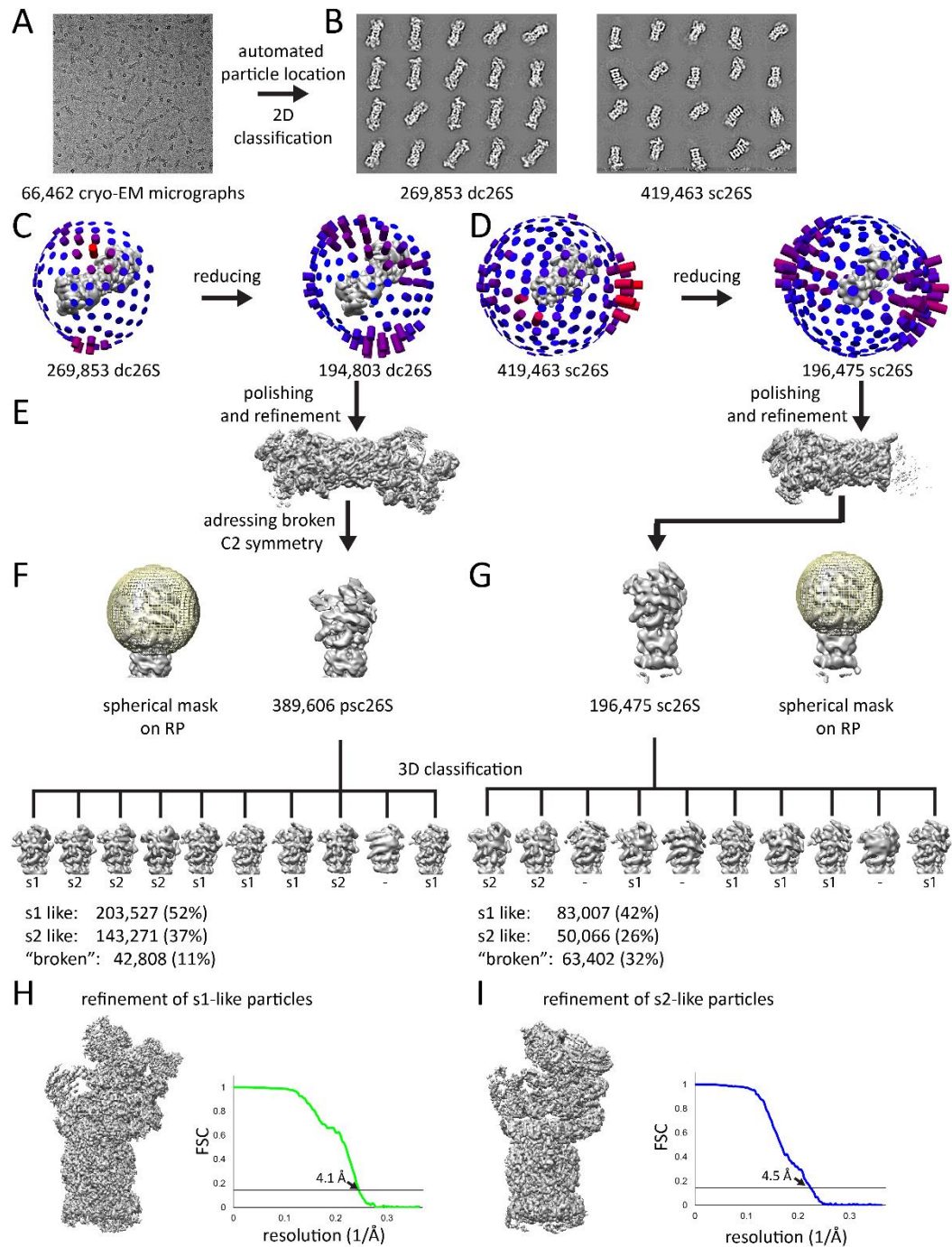


**Figure 4.5:** SPA of the 26S proteasome in the presence of ATP (adapted from [105]). **(A)** Representative cryo-EM image of the data set. **(B)** Representative 2D class averages of sc26S and dc26S. **(C and D)** Angular distribution of all dc26S/sc26S particles. Reduction of particle number from above-average occupied angular classes. Distribution of particles per angle class is shown as colored bars. Height and color of the bars correspond to the particle number. **(E)** Refined 3D reconstruction of dc26S and sc26S particles, respectively. **(F and G)** Classification of psc26S and sc26S with a spherical mask on the RP. The class averages are shown and the particle numbers which were assigned to the states s1 and s2, as well as unassigned particles are indicated. **(H and I)** 3D reconstruction of the refined particles in the s1 and s2 state, respectively. The resolution of the reconstructions on the basis of the gold-standard Fourier shell correlation criterion ( $FSC_{0.143}$ ) is shown.



The obtained high-resolution maps of the s1 and s2 states are identical to the previous structures but revealed more structural details of the 26S proteasome. For example, we were able to resolve structural features like the central helical bundle of the lid complex or side chains of several  $\alpha$ -helices (Figure 4.6 A, inset). The local resolution of both the s1 and s2 state reconstructions indicate, that the CP, especially in the s1 state, is resolved to better than  $1/4 \text{ \AA}^{-1}$ . Subunits in the periphery of the lid, like Rpn1, Rpn10 or Rpn13 have a resolution lower than to  $1/8 \text{ \AA}^{-1}$  (Figure 4.6 C and D). These subunits are more flexible than the CP of the proteasome and thus results in not well defined densities in the final reconstruction.

The density maps of the human [54], [57], [81] and yeast s1 state have a very similar shape. In contrast to the human 26S density maps the yeast map does show a density for the subunit Rpn13, which is not present in stoichiometric amounts in human proteasome preparations. The position of Rpn1 is also different between the human and yeast s1 state.

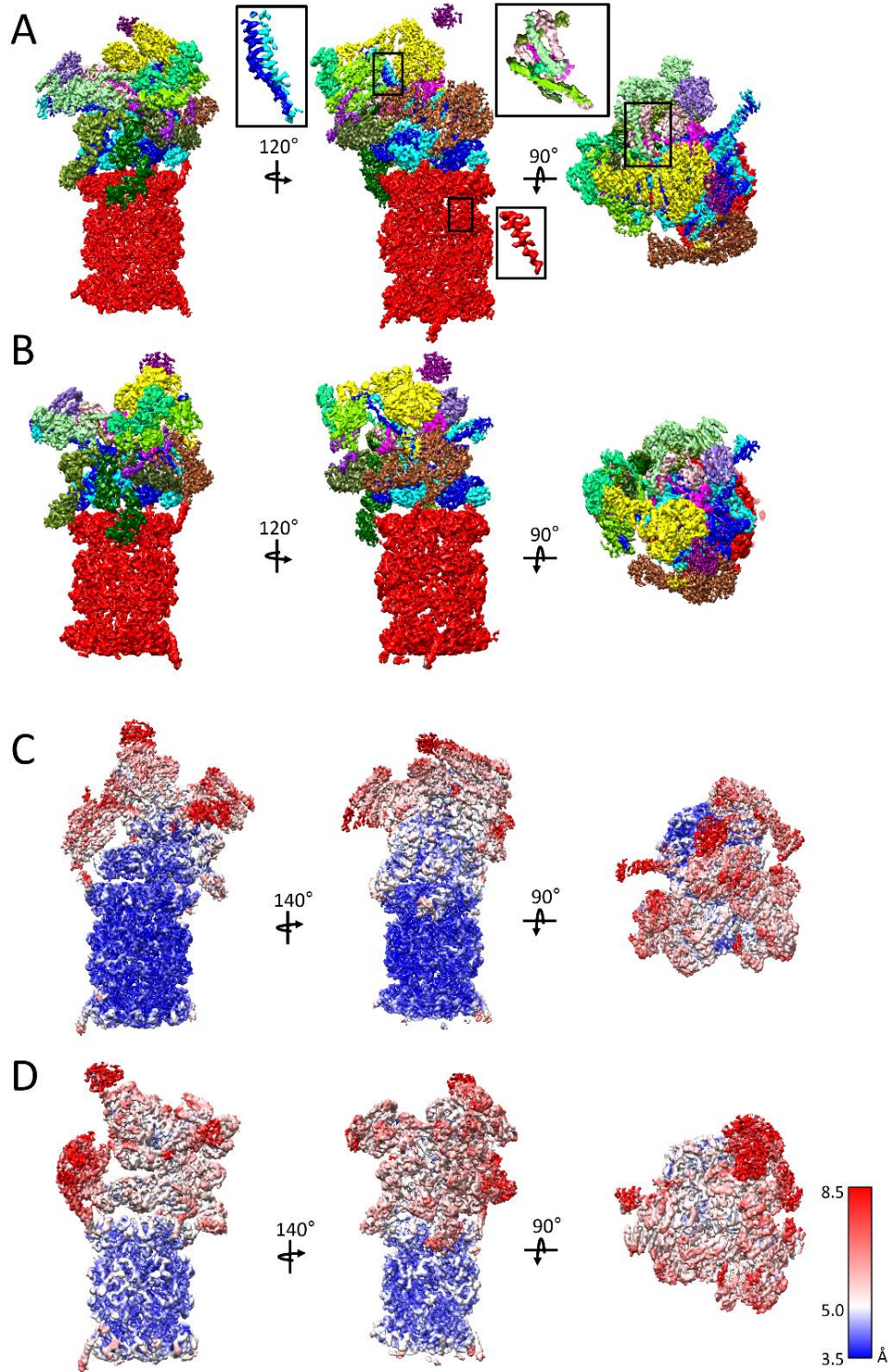


**Figure 4.6:** Cryo-EM reconstructions of the yeast 26S proteasome (taken from [105]). **(A)** s1 and **(B)** s2 reconstructions at a resolution of 4.1 and 4.5 Å, respectively. The reconstructions are colored according to the color code applied in Fig. 1.3. The insets show magnified highly resolved features like an  $\alpha$ -helix of the CP, the coiled coil of Rpt3/6 and the helical bundle of the lid. **(C and D)** Three-dimensional reconstruction from (A and B) colored according to the local resolution as given by the color gradient.

The density maps were used to build a near atomic model of the yeast 26S proteasome. First, a homology model based on the human RP model (PDB-ID: 5I4k, 5I4g; [57]) in combination with the model derived from the crystal structure of the yeast CP (PDB-ID: 5cz4; [107]) was built by comparative and de novo modeling. This initial model was fitted iteratively into the EM density using flexible fitting, which employs molecular dynamics during the fit and thus permits protein flexibility while maintaining realistic protein conformations [105]. The final model of the s1 state (Figure 4.7 A) was then fitted into the density of the s2 state using the same approach (Figure 4.7 B).

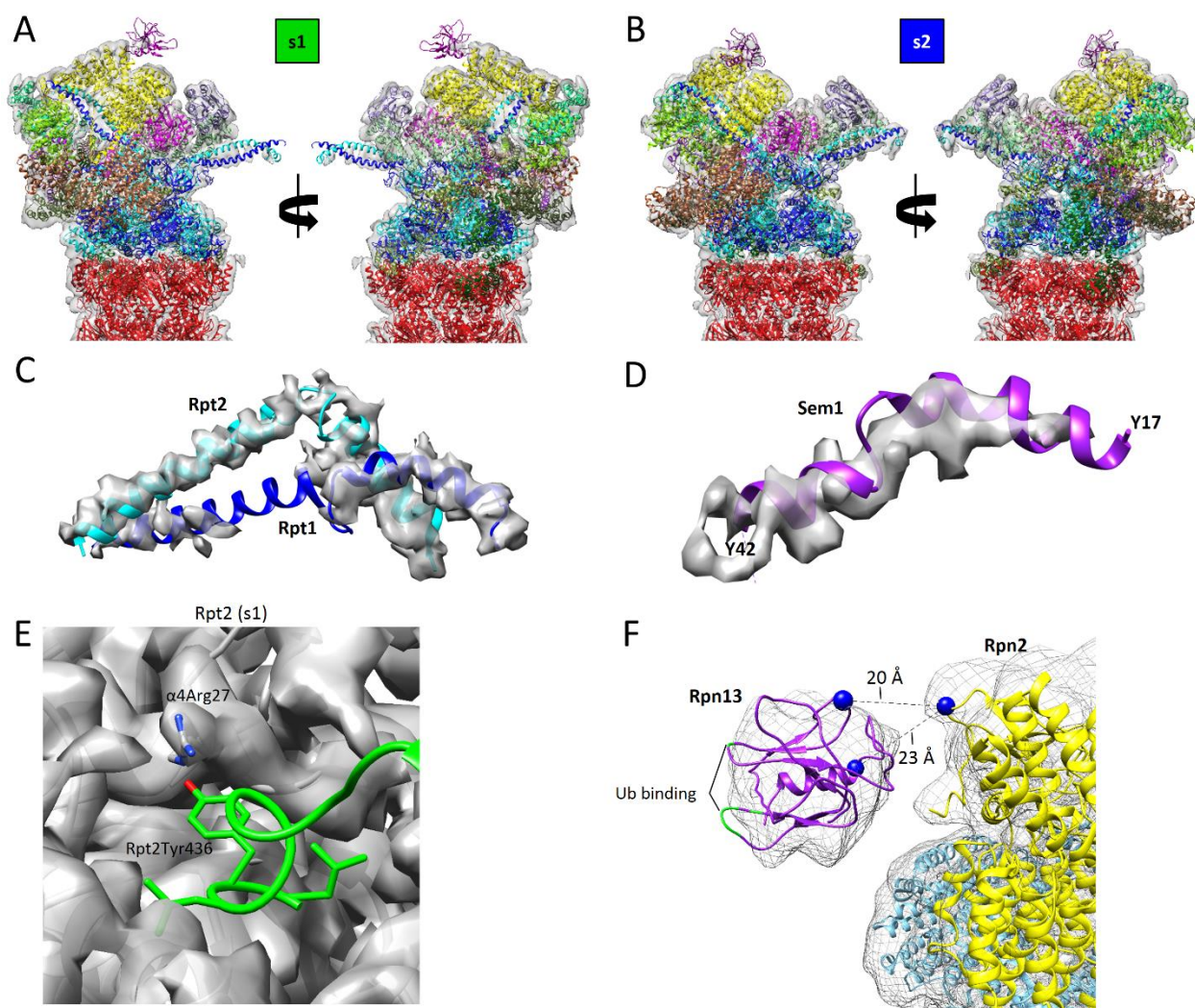


**Figure 4.7:** Model of the s1 and s2 state (adapted from [105]). Cryo-EM maps of the s1 (A) and s2 state (B) filtered to a resolution of 8 Å with the corresponding model depicted using the color code as applied in Fig. 1.3. (C) Coiled coil of Rpt1 (blue) and Rpt2 (cyan) in the s1 state. EM density is depicted in gray. (D) Model for the amino acids 17-42 of Sem1. EM density is depicted in gray. (E) HbYX motif of the Rpt2 subunit in the s1 state. EM density is depicted in gray. (F) Position of Rpn13 (purple) in respect to the lid subunit Rpn2 (yellow). The surface of the EM density of the s2 state is shown as mesh. The crosslinking distance between the residues (blue sphere) is indicated.

The highly resolved densities of the s1 and s2 states allowed us to model a kink of the coiled coil of Rpt1/2 (Figure 4.7 C), similar to the human structure [57]. In addition, we were able to model two helices of the subunit Sem1 ranging from amino acid 17-31 and 36-42 (Figure 4.7 D). Those structural regions were not modeled in previous studies [51], [82]. The detailed molecular arrangement of the nucleotide binding pockets was modeled and will be further discussed in section 4.6.3. The density of the HbYX motifs of Rpt2, 3 and 5 were clearly visible in the s1 and s2 state and allowed to position the model backbone for all Rpts. Additionally the density of the HbYX motif of Rpt2 allowed the modelling of the hydrophobic side chains (Figure 4.7 E).

Despite the lower overall resolution, the lid subunit Rpn13 was better resolved in the s2 state. In order to further analyze the structure and movement of Rpn13, a 3D classification was performed. The Rpn13 density map of the best resolved class allowed us to perform a 6D correlation scan, resulting in an unambiguous position of Rpn13, which fulfills the crosslinking restraints obtained by crosslinking mass spectrometry. In this position the ubiquitin binding residues of Rpn13 point away from the subunit Rpn2 (Figure 4.7 F). In contrast to the Rpn13 position reported previously [51], Rpn13 is rotated by  $\sim 105^\circ$ , so that the Rpn2 binding region of Rpn13 points towards Rpn2.

#### 4.4 Cryo-EM reconstruction of the 26S proteasome in the presence of AMP-PNP shows the s3 state

From 3,304 micrographs which were collected for the AMP-PNP data set, 5,680 sc26S and 40,709 dc26S particles remained after automated particle location and 2D classification. Among those, all assigned particles (sc26S and psc26S) represent the s3 state (Figure 4.8 A). The resolution of the final 3D reconstruction of the s3-like particles was 7.8 Å (Figure 4.8 B and C). The s2 model of the proteasome was fitted into the density of the s3 state using flexible fitting (Figure 4.8 D).

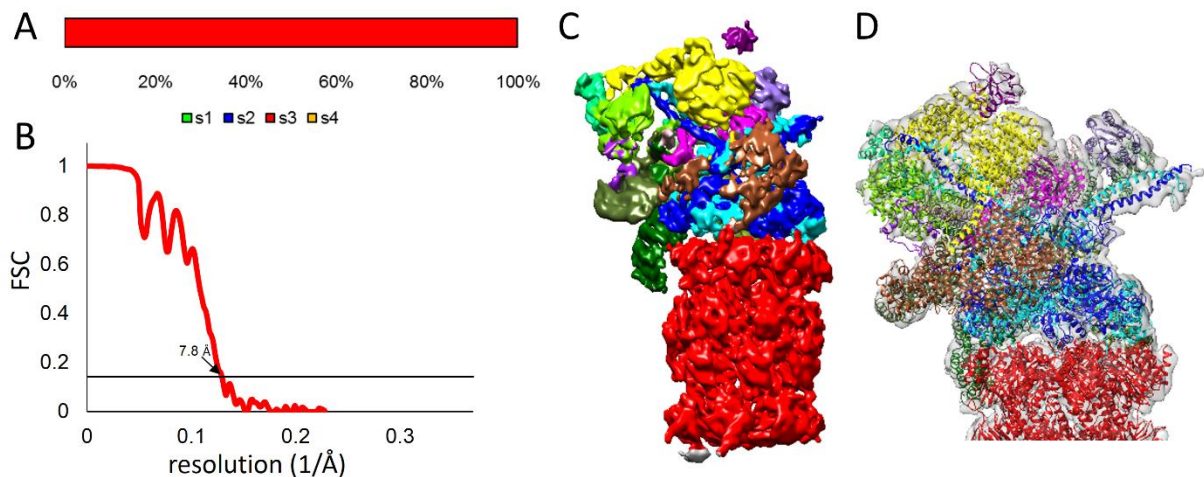


**Figure 4.8:** SPA of the AMP-PNP data set (adapted from [105]). **(A)** Distribution of particles assigned to the different states of the 26S proteasome. **(B)** The resolution of the reconstructions on the basis of the gold-standard Fourier shell correlation criterion ( $FSC_{0.143}$ ). **(C)** Cryo-EM reconstruction of the s3 state at a resolution of 7.8 Å. The reconstruction is colored according to the color code applied in Fig. 1.3. **(D)** Cryo-EM map of the s3 state filtered to a resolution of 8 Å with the corresponding model depicted using the color code as in (C).

#### 4.5 Cryo-EM reconstruction of the 26S proteasome in the presence of $BeF_x$ reveals an hitherto unobserved state

To study the state distribution of the 26S proteasome in the presence of the transition state ATP analog  $BeF_x$ , two data sets were collected. One data set with 11,121 micrographs was collected from proteasomes which were purified in the presence of ATP and  $BeF_x$  was subsequently added to the sample before plunging (ATP/ $BeF_x$ ). The second data set with 6,522 micrographs was collected from samples which were purified in the presence of ADP and  $BeF_x$  (ADP- $BeF_x$ ). Both data sets were subjected to automated particle localization and sequential 2D classification separately. 20,325 sc26S and 238,046 psc26S particles from the ATP- $BeF_x$  data set and 75,323 sc26S and 218,042 psc26S particles from the ADP- $BeF_x$  data set were classified separately in 3D and the class averages were assigned to the states of the proteasome. All particles from both data sets which did not show the s1 state, were combined and further classified in 3D. Among those particles 27,625 were assigned to a previously unknown state which is termed the s4 state (Figure 4.9). The overall architecture of the s4 state is similar to the s3 state, with the difference that Rpn1 is in a similar configuration as in the s2 state, where the N-terminus is closer to the  $AAA^+$ -ATPase.

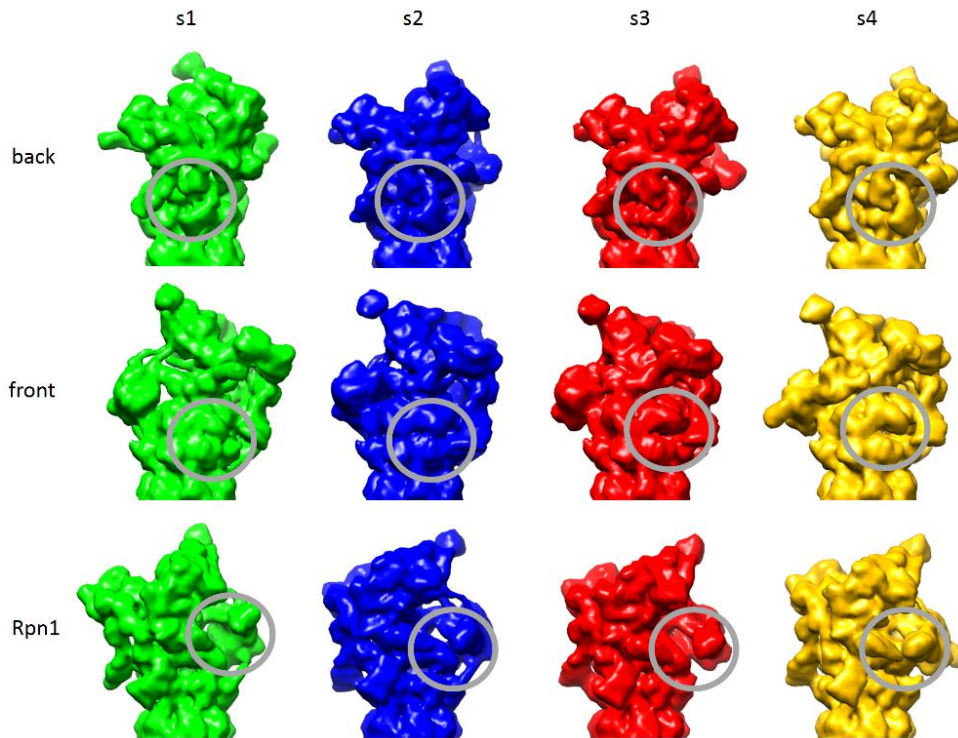


**Figure 4.9:** Comparison of EM density maps of the s1 (green), s2 (blue), s3 (red) and s4 (yellow) states. Main structural differences are highlighted with gray circles.

The s4 state is a very lowly abundant state in both data sets, which implies to a transient conformation of the proteasome. The abundance in the presence of ADP-BeF<sub>x</sub> is only around 2%, while in the presence of ATP/BeF<sub>x</sub> 9% (Figure 4.10 A). The s4-like particles were refined and the final reconstruction had a resolution of 7.7 Å (Figure 4.10 B and C). Starting from the s3 model, a model of the s4 state was built using flexible fitting (Figure 4.10 D).

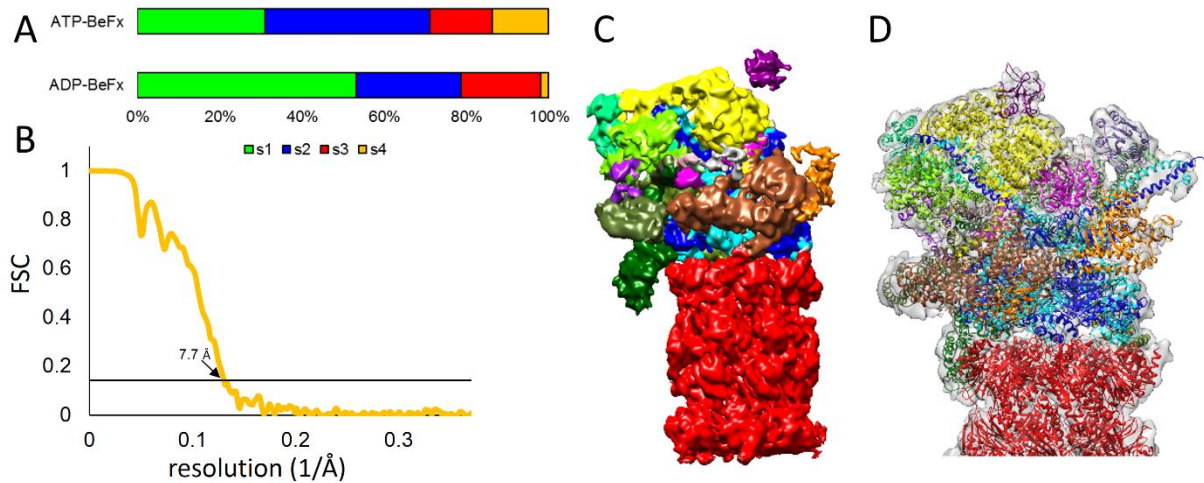


**Figure 4.10:** SPA of the ADP/ATP-BeF<sub>x</sub> data sets (adapted from [105]). **(A)** Distribution of particles from the ATP/BeF<sub>x</sub> and ADP-BeF<sub>x</sub> data set assigned to the different states of the 26S proteasome. **(B)** The resolution of the reconstructions on the basis of the gold-standard Fourier shell correlation criterion (FSC<sub>0.143</sub>). **(C)** Cryo-EM reconstruction of the s4 state at a resolution of 7.7 Å. The reconstruction is colored according to the color code applied in Fig. 1.3, additionally Ubp6 is colored in orange. **(D)** Cryo-EM map of the s4 state filtered to a resolution of 8 Å with the corresponding model depicted using the color code as in (C).

#### 4.5.1 Ubp6 is bound in the s4 state

The reconstruction of the s4-like particles shows an additional density (Figure 4.10 C, orange) which was not observed in any other states in the BeF<sub>x</sub> data sets. The density has a similar shape to the density which was assigned to Ubp6 [52] and, indeed, the Ubp6 model was fitted into the observed density (Figure 4.11 B). The Ubl domain of Ubp6 was found to bind Rpn1 and the USP domain is bound to the OB-ring of the ATPase. Due to the dynamic binding of Ubp6 on the proteasome, Ubp6 was stabilized by ubiquitin aldehyde (UbAld) in the previous study [52]. The density corresponding to UbAld was, indeed, missing in the density map of the s4 state. Different from the Ubp6-proteasome complex from this study, the previously reported Ubp6-proteasome adopts the s2 conformation. To clarify whether Ubp6 induces the s4 conformation, we applied a focused classification of the s4-like particles with a spherical mask around the Ubp6 density. Nearly half of the particles contain an Ubp6 density but the rest of particles do not possess Ubp6, indicating that Ubp6 is not a determinant of the s4 conformation (Figure 4.11 A).

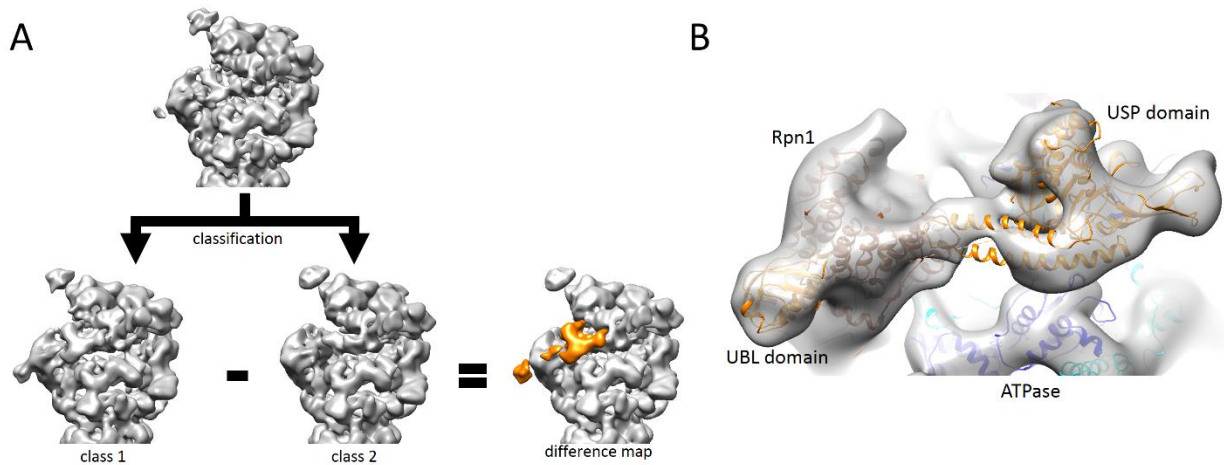


**Figure 4.11:** Ubp6 density of s4-like particles (adapted from [105]). **(A)** Classification of s4-like particles using a spherical mask around the density of Ubp6. The difference map, highlighting the Ubp6 density, is colored orange. **(B)** Model of the Ubp6-bound proteasome structure (same color code as Fig 4.10) positioned into the cryo-EM map of class 1 from (A).

## 4.6 Comparison between the s1, s2, s3, and s4 states of the yeast 26S proteasome

### 4.6.1 Structural comparison between the s1, s2, s3, and s4 states

The CP behaves almost as a rigid body and does not undergo large scale conformational changes in the four conformational states. In contrast, the RP exhibits not only global conformational changes with respect to the CP but also local conformational changes which relocate the positions of the RP subunits. In the s1 state, the lid subunits are positioned in a way that the N-terminal  $\alpha$ -solenoid of Rpn6 is in contact with the CP. The central pores of the CP, AAA<sup>+</sup>-ring and OB-ring are not coaxially aligned and the catalytic site of Rpn11 is off-axis with the pore of the OB-ring [26], [51]. From s1 to s2, the lid undergoes a rotation leading to a discrete position of the N-terminal parts of Rpn5 and Rpn6 [51] (Figure 4.12 A). The AAA<sup>+</sup>-ring shifts towards Rpn1 and as a consequence, the central channel of the ring aligns with that of the CP. Additionally the Rpn8/11 heterodimer is shifted, positioning the catalytic site of Rpn11 along the central axis of the ATPase ring as described previously [51], [53].

The conformational differences among the lid subunits of the s2, s3 and s4 state can be described as a shift towards Rpn1. The ATPase subunits undergo a shift coupled to the conformational change of the lid complex aligning the central channel of the AAA<sup>+</sup>-ring with the one of the CP (Figure 4.12 B, C and D). In the s3 and s4 state the central channels are better aligned than in the s2 state as reported previously [30].



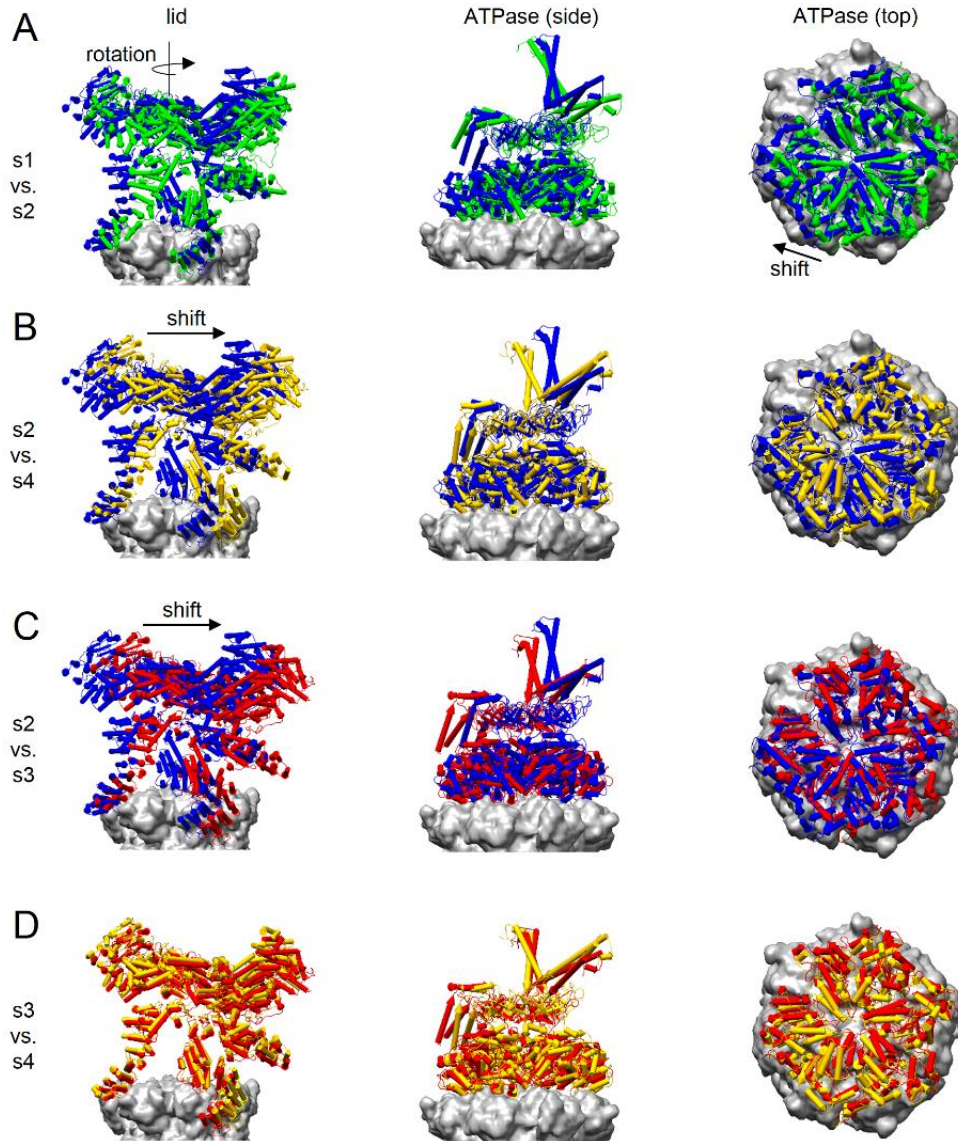


**Figure 4.12:** Superimposition of the models of the 26S proteasome states (adapted from [105]). The EM density of the CP is shown in gray. The models of the lid (left) and the ATPase (center and right) are depicted in pipes-and-planks representation (s1, green; s2, blue; s3, red; and s4, yellow).

A detailed comparison between s3 and s4 visualizes the shift of several subunits (Figure 4.13). For example the catalytic subunit Rpn11 is shifted by  $\sim 11$  Å towards Rpn10 from the s3 to the s4 state, coupled to the shift of the OB-ring of the ATPase. The  $\alpha$ -solenoid of Rpn6 moves by  $\sim 12$  Å towards Rpn7. The conformational change from s3 to s4 brings the N-terminus of Rpn1 about  $\sim 24$  Å closer to the AAA<sup>+</sup>-ring.

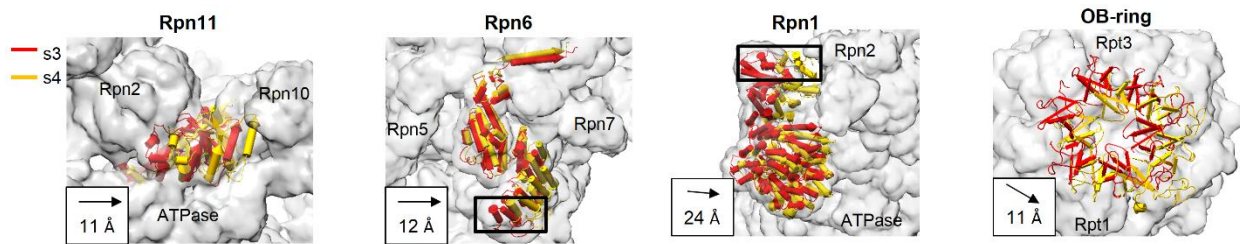


**Figure 4.13:** Superimposition of selected subunits of the s3 and s4 states (adapted from [105]). The s3 and s4 models are colored in red and yellow and the proteasome density of the s3 state is displayed in gray.

In order to visualize conformational differences of the Rpt subunits on an atomic level, the residue-wise root-mean-square deviation (RMSD) was calculated comparing the models from s1, s2, s3, and s4 (Figure 4.14). As previously reported, the lid undergoes a large rotation and the position of the AAA<sup>+</sup>-ring with respect to the CP is shifted by  $\sim 10$  Å from s1 to s2 (Figure 4.14 A, C and D). Interestingly, the superimposition of the AAA<sup>+</sup>-rings shows no significant conformational difference between s1 and s2 (Figure 4.14 B). Only the HbYX motifs and the ATPase coiled coils change their position, which is in line with the previous observation of the shift of the AAA<sup>+</sup>-ring from s1 to s2. While the residue-wise RMSD for the coiled coils of Rpt6/3 and Rpt4/5 is in the range of  $\sim 10$  Å, the N-terminal part of the coiled coil of Rpt1/2 which is connected to Rpn1 changes the position by approximately 20 Å. Considering that no structural change in the nucleotide pockets of the AAA<sup>+</sup>-ring was observed (Figure 4.14 B), ATP-hydrolysis is not likely to be involved in the structural transition from s1 to s2.

In contrast to the conformational difference between s1 and s2, the Rpt domains undergo a large conformational change from s2 to s3 (Figure 4.14 B). The structural shifts of the coiled coils are in the range of  $\sim 20$  Å. The largest conformational difference was observed for subunits Rpt3 and Rpt4, implying that most likely ATP binding or hydrolysis triggers the transition from s2 to s3. Some of the lid subunits like Rpn2, 3 and 12 undergo a conformational change in the range of 30 Å, whereas most of the lid subunits change their positions by around 15 Å (Figure 4.14 C and D). The difference between s3 and s4 is not as pronounced as between s2 and s3. The coiled coils and the OB-ring shows a residue-wise RMSD in the range of  $\sim 10$  Å. The AAA<sup>+</sup> domains of most of the subunits show a residue-wise RMSD between 0-10 Å. Only Rpt1 and Rpt2 seem to undergo a larger shift in the position of the atoms of up to 20 Å. In contrast to the RMSD differences between the s2 and s3 state, most of the lid subunits do not undergo large conformational changes from s3 to s4. Only the N-terminal amino acids of Rpn1 show RMSD values in the range of 30 Å (Figure 4.14 C and D).

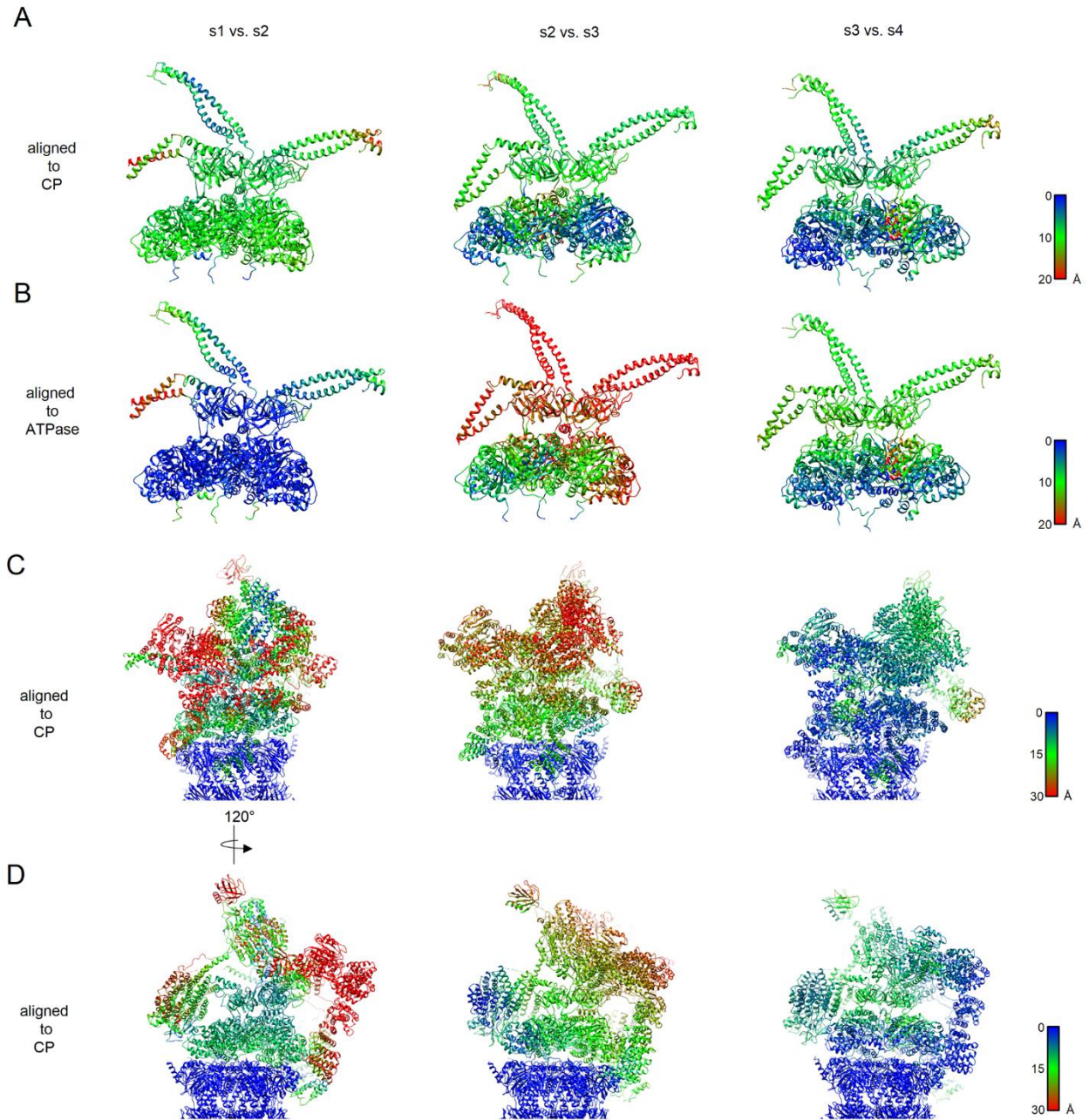


**Figure 4.14:** Residue-wise root mean square deviation (RMSD, in Å) of the 26S proteasome (taken from [105]). **(A and B)** Residue-wise RMSD of the AAA<sup>+</sup>-ATPase between the s1 vs. s2 state (left), s2 vs. s3 state (middle) and s3 vs. s4 state (right), aligned to the CP (A) and to the ATPase (B). **(C and D)** Residue-wise RMSD of the whole proteasome aligned to the CP. Colored according to the RMSD as given by the respective color gradient.

#### 4.6.2 The staircase arrangements of the pore-loops of the AAA<sup>+</sup>-ATPase change height between the states

The AAA<sup>+</sup>-ring of the proteasome in the s1 state does not adopt a planar structure. Instead, it forms a helical staircase arrangement of the Rpt subunits leading to a lock washer conformation, splitting the interface between the subunits Rpt3 and Rpt6 [30]. The pore-loops which are responsible for the translocation of substrates by pulling the polypeptide into the CP protrude into the channel of the ATPase ring [61]. In the pore-1 loop, a tyrosine residue is conserved among the Rpt subunits. To address the dynamics of the pore-1 loops, the height of the tyrosine residue above the CP in each conformational state was shown in Figure 4.15. In the s1 state the tyrosine residues position in a staircase arrangement with Rpt2 at the bottom and Rpt3 at the top position. The staircase arrangement of the s2 state is similar to that of the s1 state, due to the structural similarity of the ATPase. The conformational change of the ATPase subunits from s2 to s3 and s4 induces a change of the staircase conformation. In the s3 state Rpt5 is at the bottom and Rpt1 at the top of the staircase. The staircase of the s4 state is arranged with Rpt3 at the bottom and Rpt5 at the top (Figure 4.15).

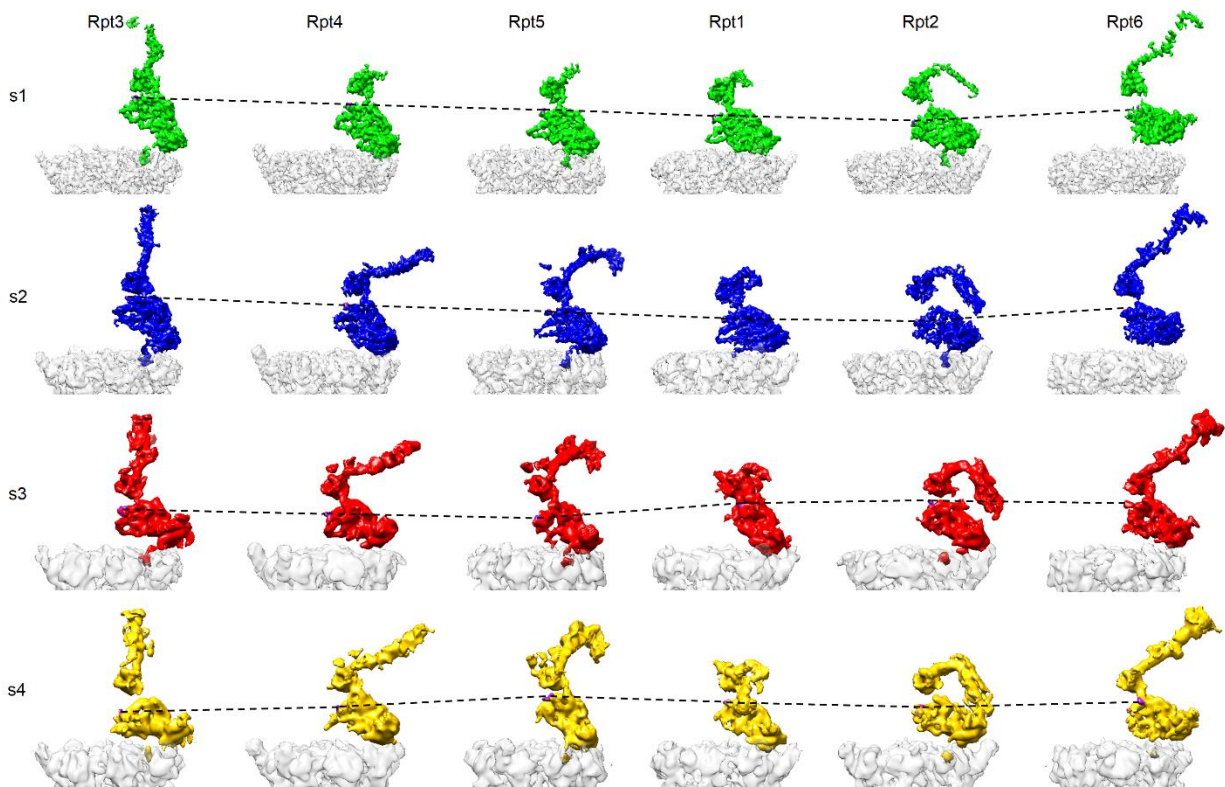


**Figure 4.15:** Height of the conserved tyrosine of the pore-1 loops (taken from [105]). Segmented densities of the Rpt subunits of the four states rotated around the CP axis (60° steps). The conserved tyrosine is colored purple and the dotted lines represent the heights. The density of the CP is colored gray.

Because of the flexibility of the pore-1 loops, their density is not well-resolved in all states. Instead, we investigated the staircase arrangement by measuring the height of the  $\alpha 8$  helices, which follow C-terminally of the pore-1 loops (Figure 4.16 A). The  $\alpha 8$  helices alter not only their height but also their tilt angle with respect to the CP plane within each state (Figure 4.16 A, B and C). For the s1 state, the  $\alpha 8$  helix of Rpt3 which positions at the top of the staircase is almost parallel to the CP, whereas the Rpt2  $\alpha 8$  helix at the bottom of the staircase is tilted inwards (Figure 4.16 A). The  $\alpha 8$  helices of the other four Rpt subunits locate in between the helices of Rtp3 and Rpt2 and have different tilt angles. The positions and tilts of the  $\alpha 8$  helices of the s2 state are similar to the s1 state, again indicating that most likely the conformation of the AAA<sup>+</sup> domains of the ATPase between s1 and s2 is identical. The arrangement of the  $\alpha 8$  helices in the s3 state is different to the one observed for the s1 and s2 states. For example, the  $\alpha 8$  helix of Rpt2 is oriented in parallel and almost at the top position of the staircase in the s3 state. The  $\alpha 8$  helix of Rpt3 which was parallel and at the top of the staircase in the s1 state resides at an intermediate height of the staircase and is tilted inwards in the s3 state. The  $\alpha 8$  helix of Rpt1 is at the top and the helix of Rpt5 at the bottom of the staircase in the s3 state. In contrast the  $\alpha 8$  helices of the s4 state adopt a different staircase than the other states. The  $\alpha 8$  helix of Rpt5 is tilted outwards and at the top position and the  $\alpha 8$  helix of Rpt3 is tilted inwards and located at the bottom (Figure 4.16 A and B). Thus, the pore-1 loops change their heights depending on the conformational state. The difference in tilt angles of the  $\alpha 8$  helices helps to gain larger height difference of the pore-1 loops which results in a larger step size during substrate translocation.

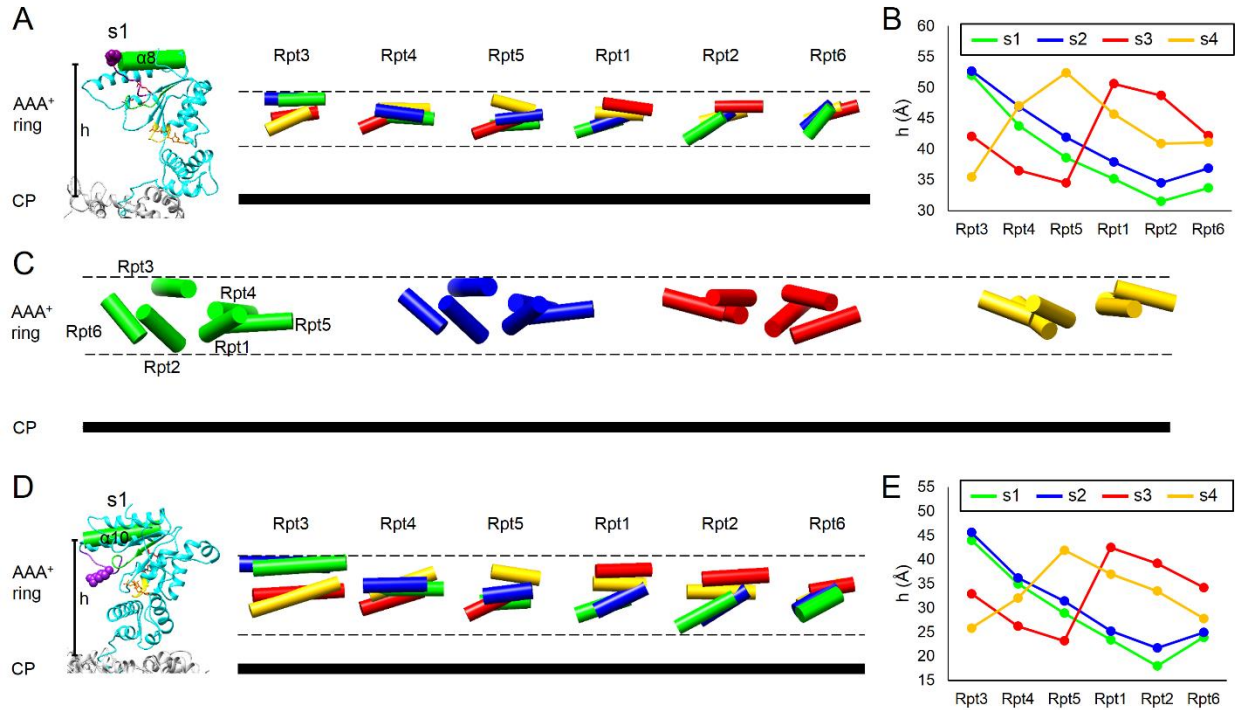


**Figure 4.16:** Conformation of the AAA<sup>+</sup>-ATPase (A, B and C taken from [105]). **(A)** Architecture of the pore-1 loop of Rpt3 in the s1 state (Left). The conserved tyrosine residue is shown as spheres and colored purple. The  $\alpha 8$  helices are depicted as colored cylinders (Right; s1, green; s2, blue; s3, red; and s4, yellow). **(B)** Height (h) of the N-terminal tip of the  $\alpha 8$  helix with respect to the CP (plane spanning through the C <sub>$\alpha$</sub>  atoms of  $\alpha_4$  Arg-27,  $\alpha_2$  Glu-30, and  $\alpha_6$  Glu-30). **(C)** Conformation of the  $\alpha 8$  helices of the four states. **(D)** Architecture of the pore-2 loop of Rpt3 in the s1 state (Left). The conserved arginine residue is shown as spheres and colored purple. The  $\alpha 10$  helices are depicted as colored cylinders reflecting different states (Right). **(E)** Height (h) of the N-terminal tip of the  $\alpha 10$  helix with respect to the CP.

The pore-2 loops, which are located approximately 10 Å below the pore-1 loops, also show a staircase arrangement. In order to describe the height of the pore-2 loops, which have a conserved Arginine residue, the height of the N-terminal tip of the  $\alpha 10$  helix was determined (Figure 4.16 D and E). The staircase arrangement of the pore-2 loops is very similar to the staircase arrangement of the pore-1 loops. For example the  $\alpha 10$  helix of Rpt3 locates at the top and the  $\alpha 10$  helix of Rpt2 at the bottom of the staircase in the s1 state, as observed for the staircase arrangement of the pore-1 loops. The movements of the pore-1 and pore-2 loops are coupled, indicating a cooperative function during substrate translocation.

#### 4.6.3 The nucleotide-binding pockets possess different conformations

The nucleotide-binding pocket of the Rpt subunits consists of five conserved motifs: Walker A, Walker B, sensor I, sensor II, and Arg-fingers. The nucleotide binds in the “interface module” formed by the large domain of an Rpt subunit and the small domain of its adjacent Rpt subunit. In the “engaged” pocket, the

nucleotide binds to the Walker A motif and is coordinated by the side chains of the Arg-finger (Figure 4.17 A).

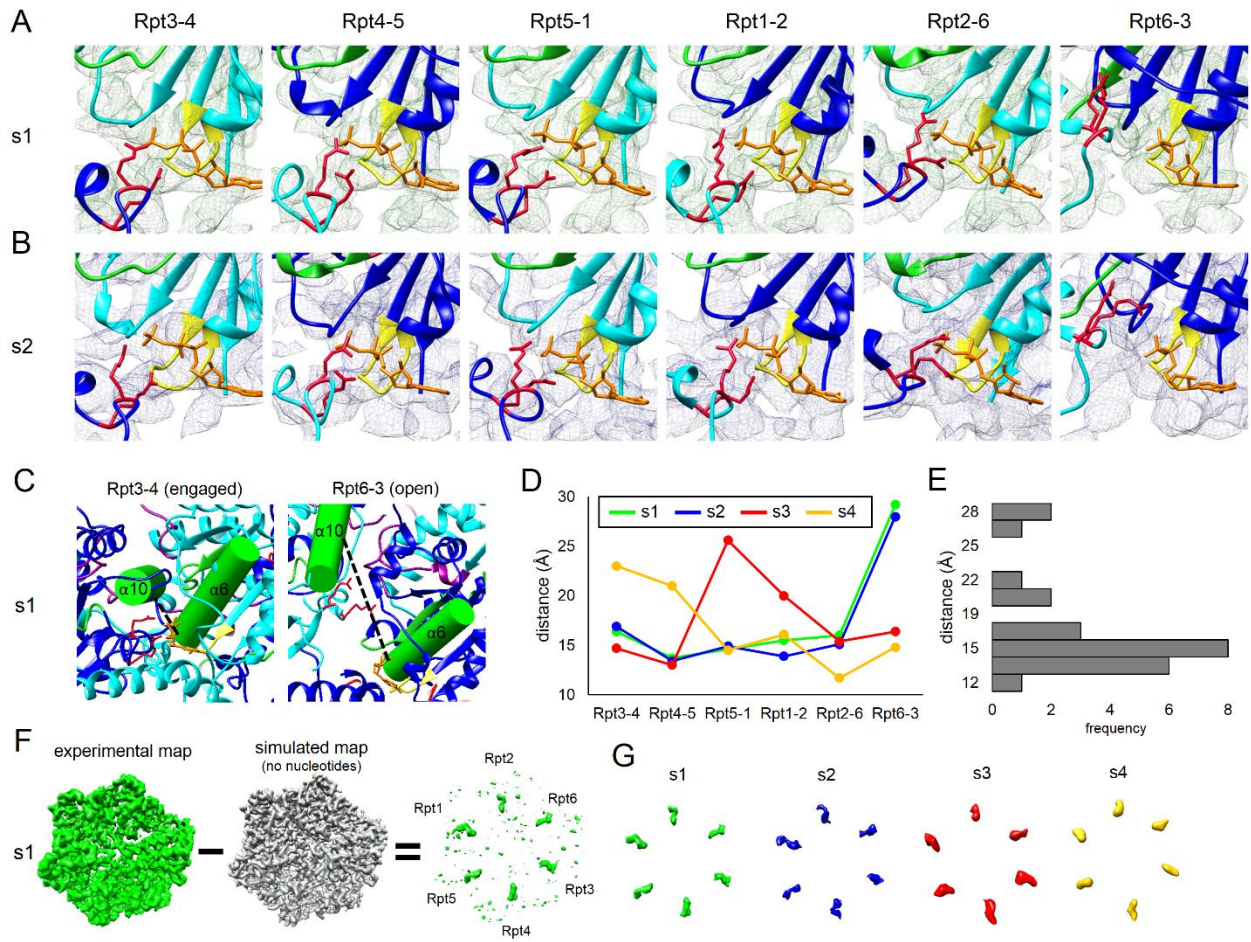


**Figure 4.17:** Nucleotide-binding pockets (taken from [105]). EM density and model of the nucleotide binding pocket of the AAA<sup>+</sup>-ATPase in the s1 state (A) and s2 state (B). The nucleotide is colored in orange, the Arg-fingers in red, the Walker A motif in yellow and the Walker B motif in green. The Rpt subunits are colored in cyan (Rpt2, 3 and 5) and blue (Rpt1, 4 and 6). (C) The position of the helices  $\alpha_6$  and  $\alpha_{10}$  of the nucleotide binding pocket in the s1 state for an engaged (left) and open (right) pocket. (D) Pocket distances of the N-terminal tip of helix  $\alpha_6$  and the center of  $\alpha_{10}$  for the four states. (E) Histogram of the pocket distance from (D). (F) Subtraction of the EM density of the experimental map from the simulated map of the model without nucleotides for the s1 state. (G) Comparison of the difference maps for the four states (s1, green; s2, blue; s3, red; and s4, yellow).

In the s1 state, five out of six nucleotide pockets show tight binding of the nucleotide, implying ATP binding as observed previously [57]. The nucleotide binding pocket of Rpt6/3 does show a different conformation and the distance between the Arg-fingers is larger than for the engaged pockets. This “open pocket” is positioned at the split site of the lock washer conformation. The nucleotide binding pockets of the s2 state show the same conformation as for the s1 state, implying no change in the nucleotide composition of the ATPase between s1 and s2. The distance of the nucleotide binding pockets can be described by the

distance between the N-terminal tip of helix  $\alpha_6$ , where the Walker A motif is located, and the middle of the  $\alpha_{10}$  helix (“pocket distance”) (Figure 4.17 C). The distance of the “engaged pocket” is around 15 Å, whereas the one of the “open pocket” is ~28 Å (Figure 4.17 D and E). The ATPase of the s3 state does show a different conformation than the s1/s2 state with the split site of the lock washer (“open pocket”) located between Rpt5 and Rpt1 (Figure 4.17 D). The pockets of Rpt3/4, Rpt4/5, Rpt2/6 and Rpt6/3 have a small distance, indicating tight binding of the nucleotide. In contrast to the s3 state, the nucleotide pocket of Rpt5/1 has a short distance in the s4 state. None of the nucleotide pockets in the s4 state shows a clear “open pocket” conformation as observed for the s1, s2 and s3 state. Only the pockets of Rpt3/4 and Rpt4/5 have a longer distance of around 20 Å. In order to show the nucleotide density of the Rpt subunits, the difference map of the experimental map and the simulated map of the model was calculated (Figure 4.17 F). All nucleotide pockets possess a nucleotide density in all four states (Figure 4.17 G).

#### 4.6.4 The gate of the CP is open in the s4 state and the HbYX motifs bind constitutively

The gate of the CP is assembled by the N-termini of the  $\alpha$ -subunits. They extend perpendicularly to the central axis of the CP and control the entry of substrates into the catalytic chamber of the CP. The center of the  $\alpha$ -rings in the four states show different densities in the area of the gate (Figure 4.18 A). The gate density of the s1 state is similar to the simulated density of the crystal structure of the 20S with a closed gate. This indicates that the CP gate in the s1 state is in a closed conformation. The EM densities of the s2 and s3 state also show a closed gate, although the EM density of the gate in those states is not as dense as in the s1 state. The s4 state does not show a gate density, indicating an open gate conformation. Interestingly, the density is similar to the simulated map of the 20S open gate crystal structure. In the model (Figure 4.18 B and C), the N-termini of the  $\alpha$ -subunits close the gate in the s1 state and extend towards to ATPase in the s4 state to form an open gate structure.



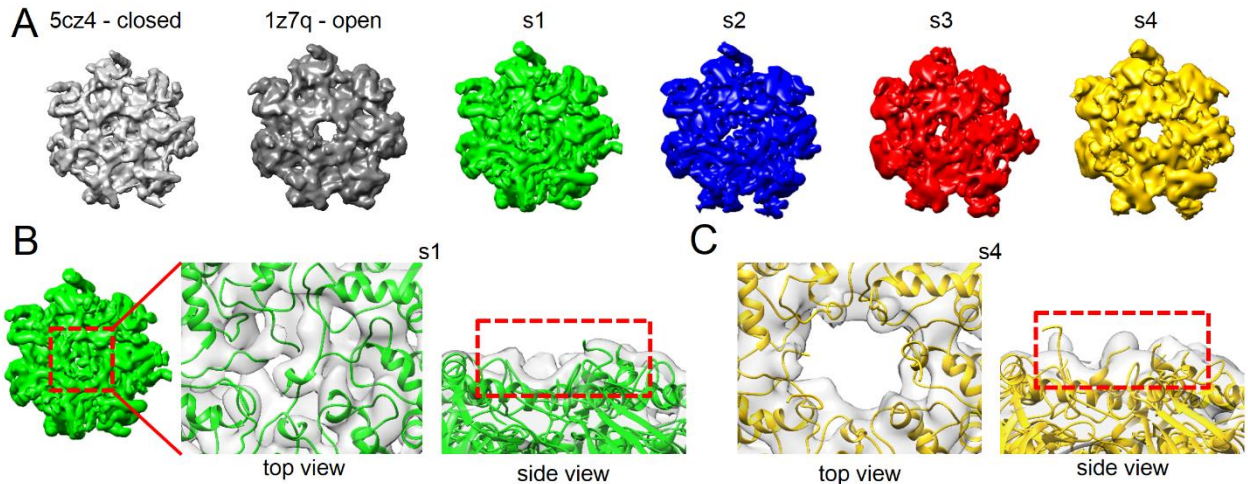


**Figure 4.18:** Gate of the CP (taken from [105]). **(A)** EM density of the  $\alpha$ -ring of the four states filtered to a resolution of 8 Å and colored accordingly. Simulated density of the crystal structure of the closed gate 20S [107] in light gray and open gate 20S [79] in dark gray. **(B and C)** Close-up view of the EM density of the  $\alpha$ -ring of the s1 state (B) and s4 state (C) with the corresponding model.

In order to quantify the CP gate EM density, the radial average of the  $\alpha$ -rings was calculated perpendicular to the central axis of the CP (Figure 4.19 and Figure 4.20). The radial average of the gate of the s1 state is similar to the reference of the closed gate crystal structure, indicating a closed gate in the s1 state. In contrast, the radial average of the s4 gate is similar to the simulated density of the open gate 20S crystal structure, supporting the open gate conformation. The gate radial averages of the s2 and s3 states lie in between the maxima of the s1 and s4 states. This might indicate that the gate is in an intermediate conformation in the s2 and s3 state. Thus, the gate opening is changed coupled to the conformational states of the AAA<sup>+</sup>-ATPases.

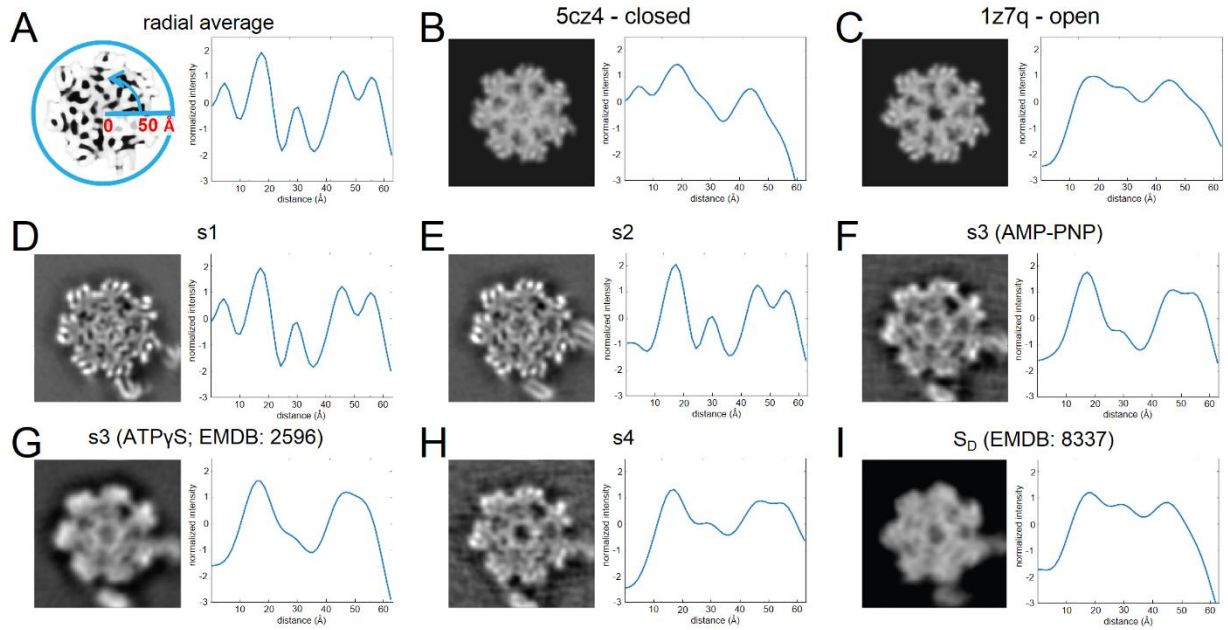


**Figure 4.19:** Radial average of the  $\alpha$ -ring (taken from [105]). **(A)** Schematic representation of the radial average calculation. Determination of the radial average of the: simulated maps (8 Å) of the **(B)** closed gate 20S crystal structure [107]; **(C)** open gate 20S crystal structure [79]; **(D-F and H)** EM maps of this study; **(G)** s3 EM map of the proteasome in the presence of ATP $\gamma$ S [51]; **(I)** EM map of the human proteasome  $S_D$  state [54].

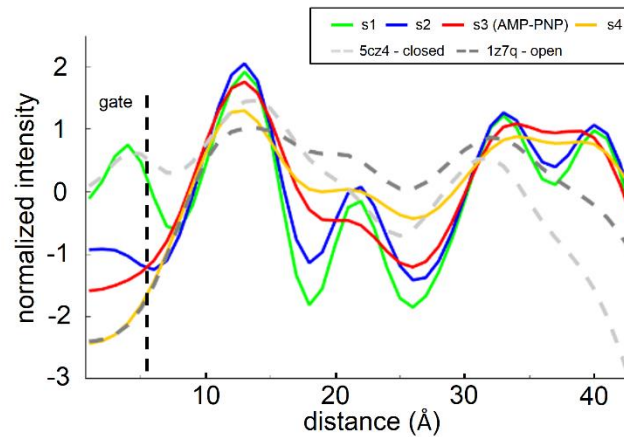


**Figure 4.20:** Radial average (modified from [105]). Overlay of the radial averages of the EM maps from Figure 4.19. The area of the gate is indicated with a black dotted line ( $\sim 6$  Å [69]).

The C-termini of three of the six AAA<sup>+</sup>-ATPase subunits (Rpt2, 3 and 5) contain a conserved HbYX motif, which is proposed to trigger opening of the 20S gate [114]. In the ground state of the human 26S proteasome, the C-termini of Rpt3 and Rpt5 are resolved [54], [57]. To analyze those interactions, the difference density of the experimental map of the CP and the simulated map was calculated (Figure 4.21 A). All four states show a clear density for three HbYX motifs. In addition, the s4 state exhibits a density for the C-terminus of Rpt6 which is bound to the pocket built by  $\alpha$ 3 and  $\alpha$ 4. The C-terminus of the Rpt1 subunits shows a helical structure in the s1 state (Figure 4.21 B) which extends towards the  $\alpha$ 6 subunit of the CP in the s2 state (Figure 4.21 B). In the s3 and s4 states, no density for the C-terminus of Rpt1 was detected. The C-terminus of Rpt4 could not be detected in any of the states.

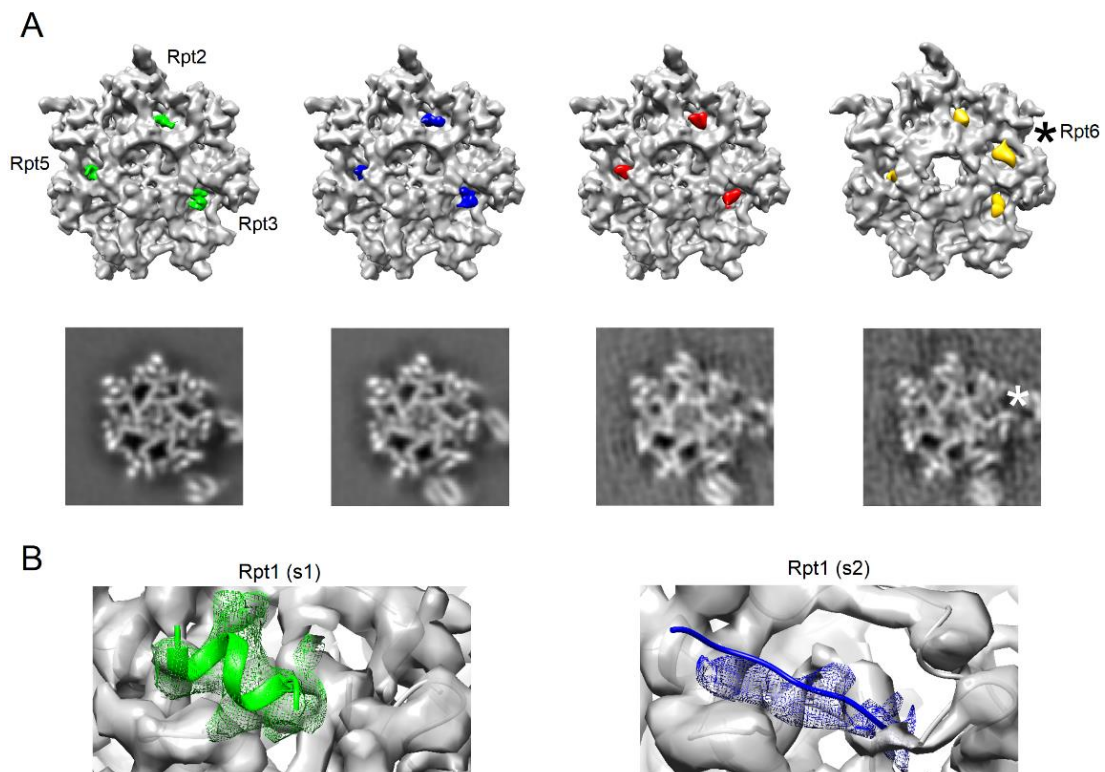


**Figure 4.21:** C-termini of the Rpt subunits (adapted from [105]). **(A, top)** The difference map resulting from the subtraction of the simulated map of the  $\alpha$ -ring of the CP and the experimental map for the four states (s1, green; s2, blue; s3, red; and s4, yellow) is depicted as an overlay with a simulated map (gray) of the closed [107] (s1, s2, s3) and open [79] (s4) 20S. A slice through the EM density at a similar position is shown in the bottom row. **(B)** Comparison of the C-terminal tail of the Rpt1 subunit in the s1 (green) and s2 state (blue). The EM map of the CP is shown in gray and the EM map of the C-terminal tail of Rpt1 is shown as mesh.

## 4.7 Comparison with other 26S proteasome models

### 4.7.1 Comparison of the yeast s1, s2 and s3 models

To visualize the agreement of the new models with the models of the s1, s2 and s3 state from the previous study of Unverdorben et al. [51], the new models were superimposed with a simulated density from the previous models (Figure 4.22). Because of structural flexibility, parts of the yeast 26S proteasome density were not well-resolved in previous studies [51], [82]. The overall architecture of the new models is in good agreement with the previously reported models. Most subunits fit into the simulated density of the corresponding states. Some parts of flexible subunits and additional parts which were not modeled previously reside outside the simulated density (Figure 4.22).

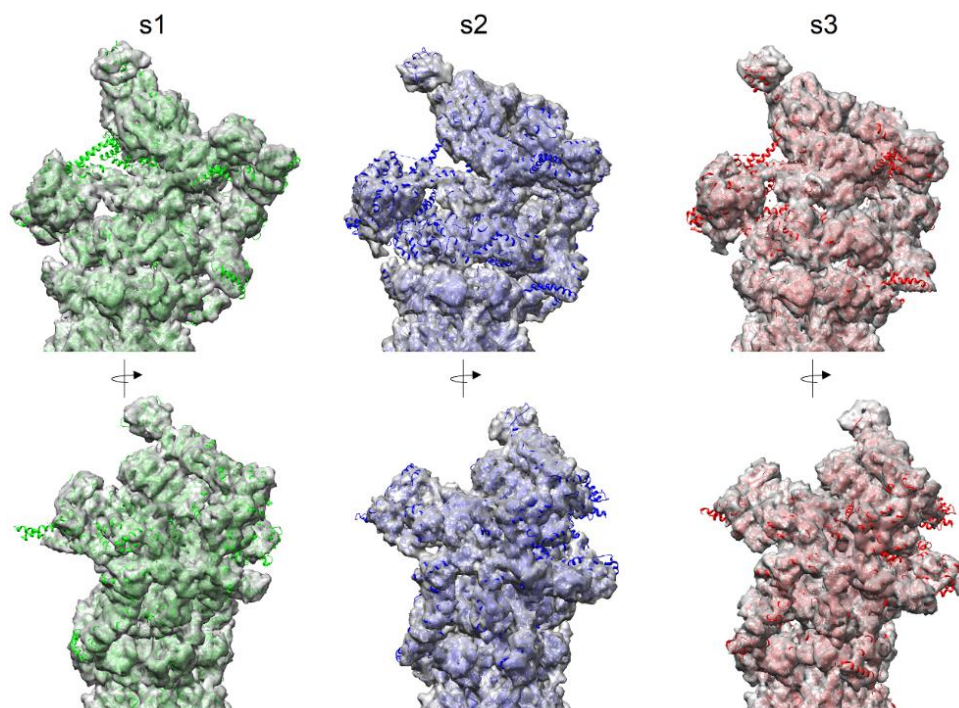


**Figure 4.22:** Comparison of yeast models. The models of the s1 (green), s2 (blue) and s3 (red) state are superimposed with a simulated map (8 Å) of the s1 (PDB-ID: 4cr2), s2 (PDB-ID: 4cr3) and s3 (PDB-ID: 4cr4) models of Unverdorben et al. [51].

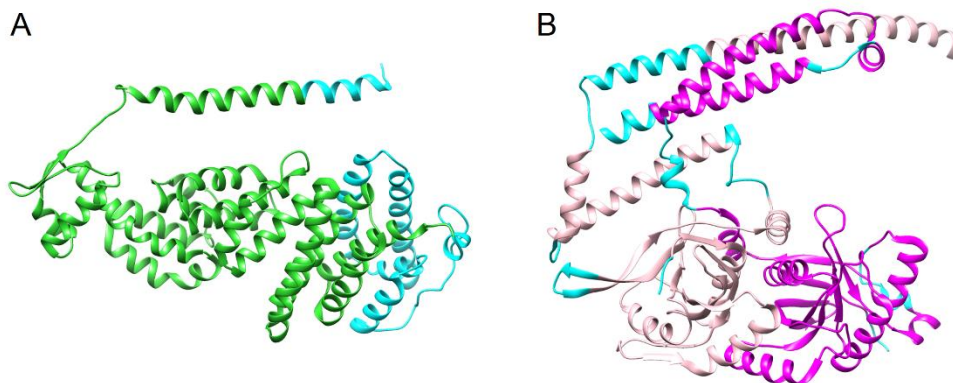
Our new EM density maps allowed us to improve the proteasome model. Nevertheless some areas, especially in the region of flexible lid subunits at the periphery, were not well-resolved and a complete model could not be built using the densities obtained in this study. The coverages of the modeled amino acids for the s1 model and the s1 model of a previous study (PDB-ID: 4cr2; [51]) are shown in Table 4.1.

**Table 4.1:** Coverage of modeled amino acids

	4cr2	s1	$\Delta$		4cr2	s1	$\Delta$
20S	97	97	0	Rpn8	75	88	13
ATPase	85	89	4	Rpn9	98	99	0
Rpn1	82	91	9	Rpn11	81	94	14
Rpn2	90	95	5	Rpn12	99	97	-3
Rpn3	67	91	23	Rpn10	74	74	0
Rpn5	93	99	6	Rpn13	81	81	0
Rpn6	99	100	1	Sem1	21	57	36
Rpn7	93	89	-5				

The sequence coverage (in %) of all modeled amino acids of the 26S proteasome subunits was calculated for the s1 model of Unverdorben et al. [51] (PDB-ID: 4cr2) and the s1 model of this study.  $\Delta$ : difference between the two models.

In comparison with the previous proteasome model of Unverdorben et al. [51], many of the subunits were modeled with a higher coverage (up to 90-100% coverage). We were able to provide a complete model of Rpn6 in this study. The regions which could not be modeled include the flexible N- and C-termini of some subunits. Some flexible parts of the coiled coils of the Rpt subunits such as the kink of the coiled coil in Rpt1/2 (Figure 4.7 C) were modeled with higher confidence in this study. Nevertheless, the interaction interface of Ubp6 at the OB domain of Rpt1 was not resolved, indicating flexibility. Modeling of the lid subunits was improved in this study. The model of Rpn3 was completed by 23%, including 110 amino acids at the N-terminus and 14 amino acids at the C-terminus (Figure 4.23 A). Missing segments of flexible regions in the MPN domains and the connections with the C-terminal helices of the Rpn8-Rpn11 heterodimer (Figure 4.23 B) were built in this study. As described in section 4.3 two  $\alpha$ -helices of Sem1 were modeled (Figure 4.7 D). The model coverage of the ubiquitin receptors Rpn10 and Rpn13 was not improved and the structure of the ubiquitin binding motif of Rpn10 is still missing in the model.

**Figure 4.23:** New modeled regions of Rpn3 (A) and the Rpn8-Rpn11 heterodimer (B) are colored in cyan. Rpn8 (pink), Rpn11 (magenta).

#### 4.7.2 Comparison of the AAA<sup>+</sup>-ATPase

The AAA<sup>+</sup>-ATPase of the proteasome forms a heterohexameric ring, in which the Rpt subunits are arranged in a lock washer conformation. The split site of the lock washer changes between the conformational states, leading to different topologies of the pore-loops and nucleotide binding pockets (section 4.6.2 and 4.6.3). In order to analyse conformational changes of reported EM structures of the 26S proteasome, we assessed the quality of the EM density map of the Rpt subunits. For comparison we generated simulated EM densities of the Rpt1 subunit at 4 Å and 8 Å, respectively (Figure 4.24). The EM densities of Rpt1 reported by several groups are shown in Table 4.2-4.5. Furthermore, the heights of the pore-1 loops and nucleotide pocket distances were calculated as described in sections 4.6.2 and 4.6.3.

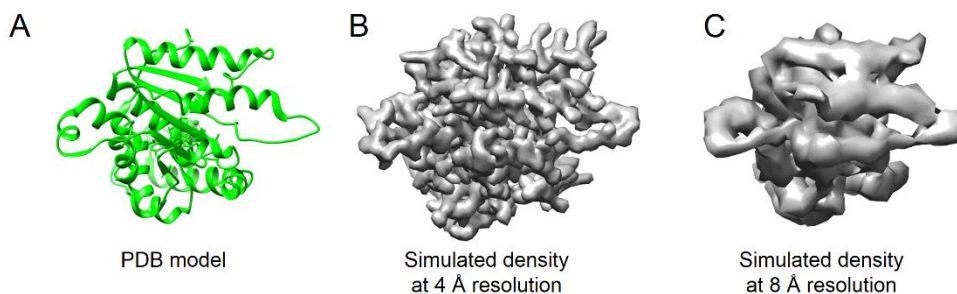


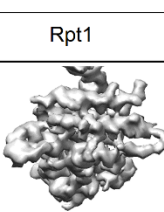
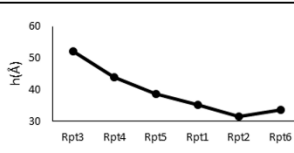
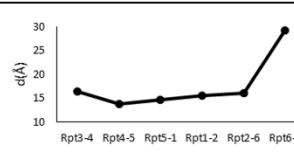
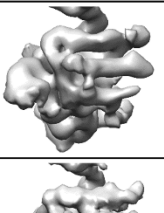
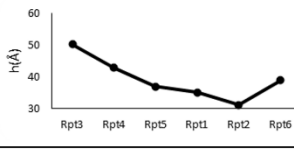
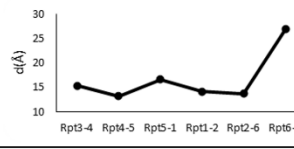
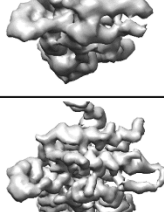
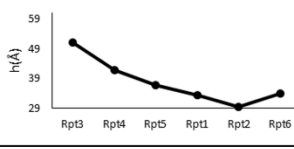
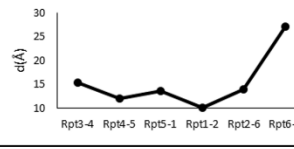
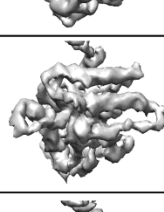
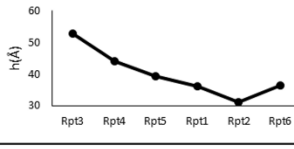
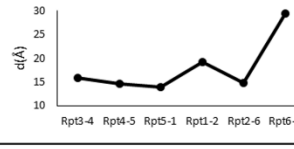
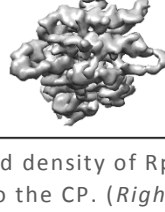
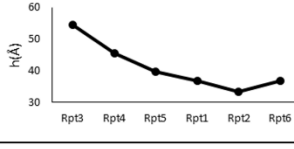
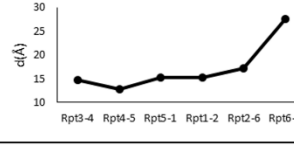
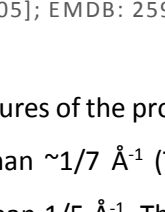
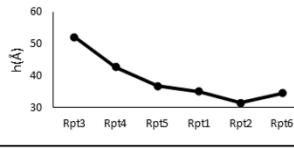
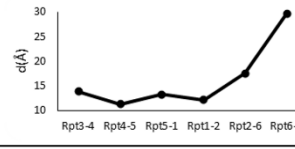
**Figure 4.24:** Simulated density of Rpt1. (A) AAA<sup>+</sup>-domain of Rpt1 (PDB-ID: 5mp9 [105]). Simulated density of Rpt1 at 4 Å (B) and 8 Å (C) resolution.

In ATP-containing buffer, most of the proteasomes adopt an s1-like conformation [51], [54], [57], [81], [82]. The overall resolution of the reported s1 state densities varies from 3.5 to 7.7 Å (Table 4.2). The reconstructions with an overall resolution of ~4 Å (EMDB: 3534, 4002, 9512) show details of some side chain densities of the Rpt subunits, which cannot be clearly resolved at 4.5 Å. Nevertheless, helices can be resolved in all maps with an overall resolution of up to 8 Å. For lower-resolved EM maps, the resolution hinders building a precise model of amino acid side chains. A flexible fitting approach could nevertheless help to position secondary structure elements into proteasome maps with an overall resolution around or lower than 1/8 Å<sup>-1</sup>, which don't show a clear separation of helical densities and therefore impede the unambiguous positioning of helices.

The α8 helices from all s1-like structures show the same helical staircase arrangement with Rpt3 at the top and Rpt5 at the bottom position. This staircase conformation seems to be a distinct feature of the s1 state of the proteasome independent of the source of the sample. The nucleotide-pocket conformation observed for the yeast 26S proteasome in this study is the same for all other s1 structures. All pockets are in an engaged conformation except for the split site of the lock washer at the interface of Rpt6/3. The only

exception is the nucleotide pocket of Rpt1/2 of the human proteasome structure of Schweitzer et al. [57]. The distance is around 5 Å larger than for the other engaged pockets. The authors of this study nevertheless suggest this pocket to be engaged. For the s1 maps reported by Chen et al. [54], Huang et al. [81], Schweitzer et al. [57] and Wehmer et al. [105] all nucleotide pockets possess a nucleotide density. It is likely, but could not be identified with certainty that the nucleotide bound to the engaged pockets is ATP.

**Table 4.2:** Comparison of the ATPase of s1-like proteasome structures

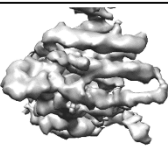
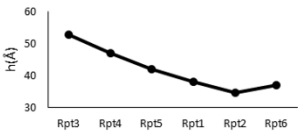
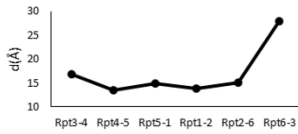
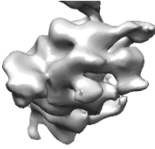
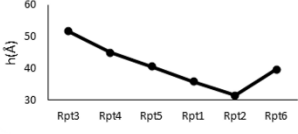
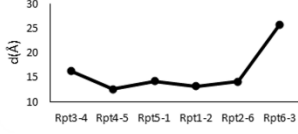
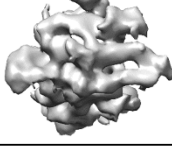
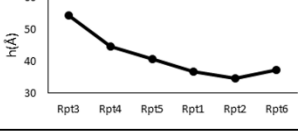
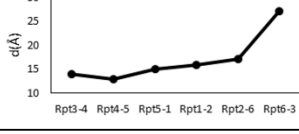
EMDB entry	Rpt1	height (h) of $\alpha 8$ helix	nucleotide pocket distance (d)
EMDB: 3534 PDB: 5mp9 yeast s1 state 4.1 Å			
EMDB: 2594 PDB: 4cr2 yeast s1 state 7.7 Å			
EMDB: 6575 PDB: 3jcp yeast M2 state 4.6 Å			
EMDB: 4002 PDB: 5l4g human s1 state 3.9 Å			
EMDB: 8334 PDB: 5t0g human S <sub>A</sub> state 4.4 Å			
EMDB: 9512 PDB: 5gjr human s1 state 3.5 Å			

(Left) The segmented density of Rpt1 is depicted in gray. (Middle) Height (h) of the N-terminal tip of the  $\alpha 8$  helix with respect to the CP. (Right) Pocket distances (d) of the N-terminal tip of helix  $\alpha 6$  and the center of  $\alpha 10$ . EMDB: 3534 [105]; EMDB: 2594 [51]; EMDB: 6575 [82]; EMDB: 4002 [57]; EMDB: 8334 [54]; EMDB: 9512 [81].

Among three structures of the proteasome in an s2-like conformation, two of the densities have an overall resolution lower than  $\sim 1/7 \text{ \AA}^{-1}$  (Table 4.3). Only the density observed in this study was resolved to a resolution higher than  $1/5 \text{ \AA}^{-1}$ . The staircase conformation and the nucleotide pocket distances of all s2-

like structures are the same as those observed in the s1 state, again showing that no ATP hydrolysis or nucleotide exchange is involved in the transition from s1 to s2.

**Table 4.3:** Comparison of the ATPase of s2-like proteasome structures

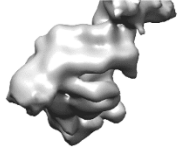
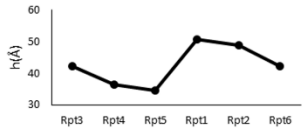
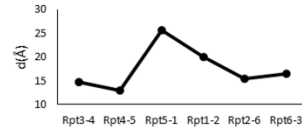
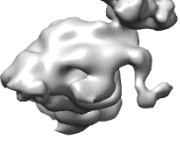
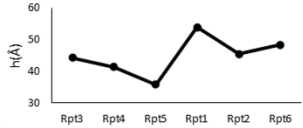
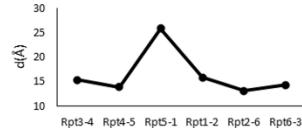
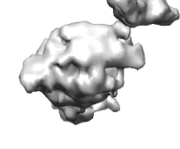
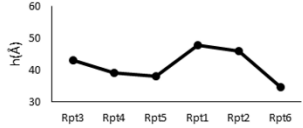
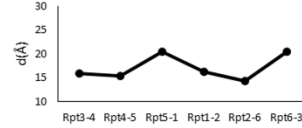
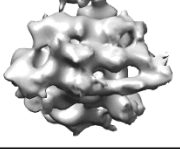
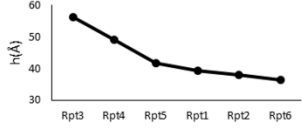
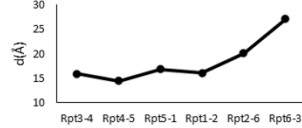
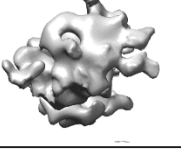
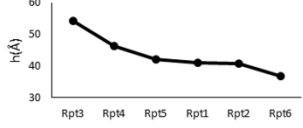
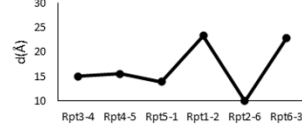
EMDB entry	Rpt1	height (h) of $\alpha 8$ helix	nucleotide pocket distance (d)
EMDB: 3535 PDB: 5mpa yeast s2 state 4.5 Å			
EMDB: 2595 PDB: 4cr3 yeast s2 state 9.3 Å			
EMDB: 8335 PDB: 5t0h human S <sub>B</sub> state 6.8 Å			

(Left) The segmented density of Rpt1 is depicted in gray. (Middle) Height (h) of the N-terminal tip of the  $\alpha 8$  helix with respect to the CP. (Right) Pocket distances (d) of the N-terminal tip of helix  $\alpha 6$  and the center of  $\alpha 10$ . EMDB: 3535 [105]; EMDB: 2595 [51]; EMDB: 8335 [54].

The proteasome adopts the s3 state mainly in the presence of non-hydrolysable ATP analogs like ATP $\gamma$ S or AMP-PNP. Other groups reported an s3-like structure of the yeast and human proteasome in the presence of ATP [54], [82] which was not detected in this study or previous studies from our group [51], [57]. All s3-like structures except for the map of the yeast M1 state [82] are not resolved to a resolution higher than  $\sim 1/8 \text{ \AA}^{-1}$  (Table 4.4). The Rpt1 EM density of the M1 state does not show, despite an overall resolution of 4.8 Å, highly resolved features of the Rpt subunit. A poorly defined EM density may result from an average over different conformational states. The conformation of the proteasome in our study was assigned based on the conformational difference of the ATPases. However, the ATPases make up only  $\sim 10\%$  of the proteasome density and small conformational changes in the ATPases might be difficult to be distinguished during classification of the holocomplex. Although the authors [54], [82] pointed out that the s3-like proteasome structures show similarities to the s3 state of the yeast 26S proteasome reported by Unverdorben et al. [51], the resolution of the EM map did not allow us to assign the precise conformational state.



**Table 4.4:** Comparison of the ATPase of s3-like proteasome structures

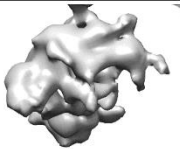
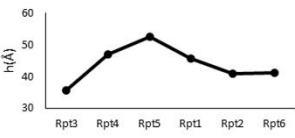
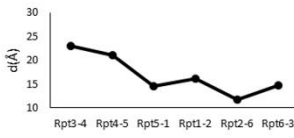
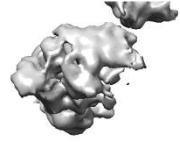
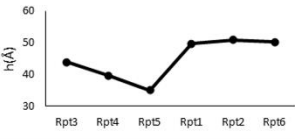
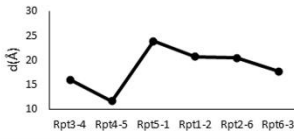
EMDB entry	Rpt1	height (h) of $\alpha 8$ helix	nucleotide pocket distance (d)
EMDB: 3536 PDB: 5mpb yeast s3 state 7.8 Å			
EMDB: 2596 PDB: 4cr4 yeast s3 state 8.8 Å			
EMDB: 6574 PDB: 3jco yeast M1 state 4.8 Å			
EMDB: 8336 PDB: 5t0i human S <sub>C</sub> state 8.0 Å			
EMDB: 8337 PDB: 5t0j human S <sub>D</sub> state 8.0 Å			

(Left) The segmented density of Rpt1 is depicted in gray. (Middle) Height (h) of the N-terminal tip of the  $\alpha 8$  helix with respect to the CP. (Right) Pocket distances (d) of the N-terminal tip of helix  $\alpha 6$  and the center of  $\alpha 10$ . EMDB: 3536 [105]; EMDB: 2596 [51]; EMDB: 6574 [82]; EMDB: 8336, 8337 [54].

The  $\alpha 8$  helices of the yeast s3 state structures (EMDB: 3536 and EMDB: 2596) show the same staircase conformation with Rpt1 at the top and Rpt5 at the bottom position. The yeast M1 state shows a different staircase conformation with Rpt6 at the bottom and Rpt1 and Rpt2 at a similar height above the CP. The split site of the lock washer is in all yeast s3-like structures between Rpt5 and Rpt1. The staircase conformation of the human S<sub>C</sub> and S<sub>D</sub> states is different from the yeast states with Rpt3 at the top and Rpt5 at the bottom position. This configuration is rather similar to the staircase of the s1 and s2 state (Table 4.2 and Table 4.3). Therefore, the staircase arrangement is contradictory to the other s3-like structures. The conformation of the nucleotide pockets of the s3-like yeast structures show the same trend with an open pocket at the interface of Rpt5/1. Nevertheless, the distance of the open pocket of the yeast M1 state is not as large as for the other yeast structures. Additionally, the distance of the nucleotide pocket between the subunits Rpt6/3 is larger than for the other engaged pockets of the M1 state. This pocket distance is also the largest in the s1 and s2 state, indicating that in the presence of ATP the proteasome might not be able to close this pocket completely. The nucleotide pocket conformation of the human S<sub>C</sub> state is different to the yeast s3-like states and shows similar distances as for the S<sub>A</sub> and S<sub>B</sub> state. In contrast

to all other s3-like structures, the human S<sub>D</sub> state shows an open pocket at the interface of Rpt1/2 and Rpt6/3 (Table 4.4). This pocket conformation was not observed in any other of the analyzed structures including the yeast s4 structure (Table 4.5).

**Table 4.5:** ATPase of other states of the proteasome

EMDB entry	Rpt1	height (h) of $\alpha$ 8 helix	nucleotide pocket distance (d)
EMDB: 3537 PDB: 5mpc yeast s4 state 7.7 Å			
EMDB: 6694 PDB: 5wvk yeast AIF <sub>x</sub> state 4.2 Å			

(Left) The segmented density of Rpt1 is depicted in gray. (Middle) Height (h) of the N-terminal tip of the  $\alpha$ 8 helix with respect to the CP. (Right) Pocket distances (d) of the N-terminal tip of helix  $\alpha$ 6 and the center of  $\alpha$ 10. EMDB: 3537 [105], EMDB: 6694 [115].

Another unique pocket conformation was reported for the yeast proteasome in the presence of ADP-AIF<sub>x</sub> [115]. The authors reported that they did not detect a significant EM density for a nucleotide in the pockets of Rpt2 and Rpt6. Our analysis shows that the pocket conformations of Rpt3-4, Rpt4-5, Rpt5-1 and Rpt6-3 are similar to the yeast s3 state (Table 4.5). The pockets of Rpt1-2 and Rpt2-6 seem to be in an open or intermediate conformation. The pore-1 loops show a similar organization as the yeast s3 state with the split site of the lock washer between Rpt5 and Rpt1. The pore-1 loops of Rpt1, 2 and 6 seem to be more planar than observed for the other yeast s3-like states. Considering the rather lowly resolved ATPase and especially the subunits Rpt2 and Rpt6 in the yeast ADP-AIF<sub>x</sub> structure (Figure 4.25) it remains unclear whether the staircase and nucleotide pocket conformation are different from previously reported states. Additionally, the low resolution of Rpt2 and Rpt6 could impede the unambiguous assignment of a nucleotide density.

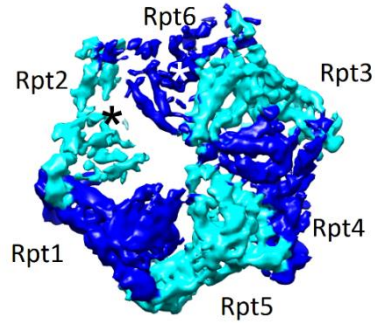


**Figure 4.25:** AAA<sup>+</sup>-ring of the 26S proteasome in presence of ADP-AlF<sub>x</sub>. The EM density of the AAA<sup>+</sup>-ring (EMDB: 6694 [115]) is depicted using the color code of Figure 1.6. Black and white asterisk indicate the approximate pocket positions with weak nucleotide densities.

#### 4.7.3 Comparison of the gate of the 20S proteasome

The radial averages calculated for the 20S  $\alpha$ -ring (Figure 4.19) showed that the gate is in a different conformation in the four proteasome states. The comparison of the gate with other proteasome densities [51], [54] indicates that the gate of the s3 state in the presence of AMP-PNP has the same radial average as the gate of the s3 state in the presence of ATPyS (Figure 4.21 A). In contrast, the reported open gate human proteasome state ( $S_D$ ) does not show the same radial average as the yeast open gate state (s4). The radial average is in better agreement with the radial average of the s3 state of the proteasome (Figure 4.21 B). If the human  $S_D$  and the yeast s4 state show different gate conformations could not be answered by the models and EM densities available.

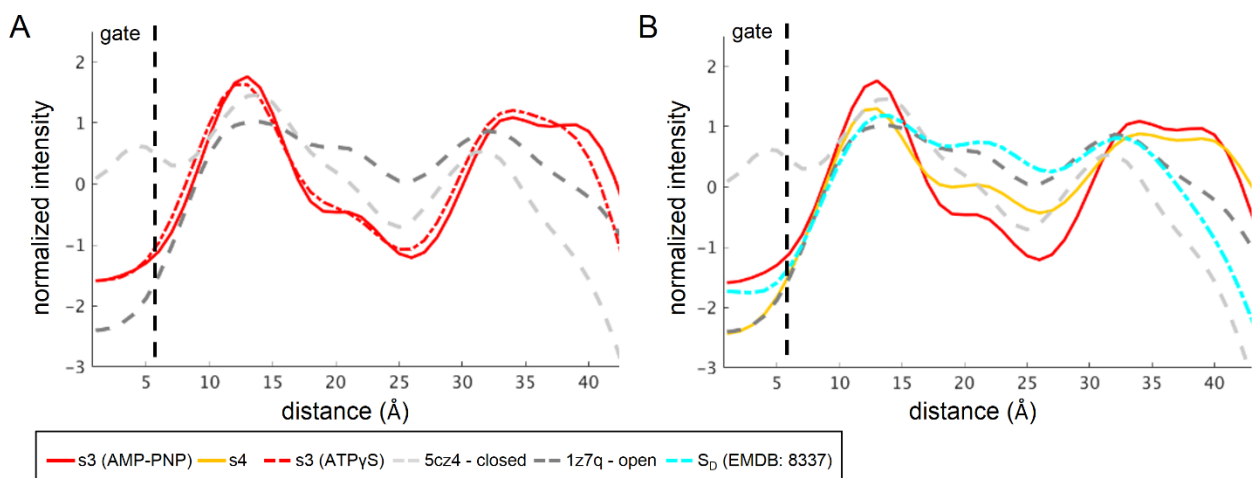


**Figure 4.21:** Radial average of the CP  $\alpha$ -ring (modified from [105]). **(A)** Overlay of the radial averages from Figure 4.19 of the EM maps of the s3 state (AMP-PNP) and the s3 state (ATPyS) from Unverdorben et al. [51]. **(B)** Overlay of the radial averages from Figure 4.19 of the EM maps of the s3 state (AMP-PNP), s4 state and the  $S_D$  state [54]. The area of the gate is indicated with a black dotted line.

## 5 Discussion

### 5.1 High-resolution proteasome structures

The resolution of 4.1 Å of the s1 state EM density of this study allowed us to build detailed models of most parts of the CP and ATPase together with several subunits like Rpn3, Rpn8, Rpn11, Rpn13 and Sem1 which were not resolved in previous studies [51]. However, structural heterogeneity of the proteasome led to lower resolved EM densities of several subunits. Due to the lower resolution, side chains at the periphery of the lid subunits were not modeled precisely. To gain a further accurate model of the side chains of the 26S proteasome, structural heterogeneity has to be minimized by modification of the sample preparation or further classification of the particles. For example, we showed in this study that the proteasome preparation using AMP-PNP traps the proteasome conformation in the s3 state only. Thus, the proteasome sample in the presence of AMP-PNP which yields homogeneous conformations could be better-resolved, including side chains. A step-wise classification approach combining standard classification with focused classification will enable us to further isolate more homogeneous particles [25]. Recently, a new classification approach where parts of the projection are subtracted was applied to a highly dynamic complex, leading to an improvement of the resolution of flexible parts [116], [117]. Macromolecules which contain either compositional or structural heterogeneity result in low-resolution EM densities because local movements of subunits are averaged. Therefore, the dissection of proteasome particles into multiple modules such as the CP, RP or AAA<sup>+</sup>-ATPase, followed by individual refinement procedure will help to improve the quality of the EM map as described for the spliceosome [118]. The refined EM densities of classes obtained by new classification strategies will provide not only a better-resolved region of interest resulting in a more precise model but also insights into the movement of individual subunits of the proteasome complex.

Several cryo-EM structures of the proteasome at a resolution in the range of 4 Å have been reported in the recent years [54], [57], [81], [82], [105], [115], where most of those densities represent the ground state (s1). This suggests that in both yeast and human samples, the s1 state is the major conformational state of the purified proteasome in the presence of ATP and most likely represents a low-energy state. However, the s1 conformation is not a unique conformation in the presence of ATP. We further processed some of the particles which we assigned to non s1-like particles and yielded an EM map of the proteasome in an activated state (s2). As it was reported in Unverdorben et al. [51], approximately 20-40 % of particles adopt the s2 state in the presence of ATP. In contrast, Luan et al. [82] reported that, in the presence of ATP, low-abundant particles adopt an s3-like state (M1 state) which was observed only in the presence of non-hydrolysable ATP analogs in our studies [30], [51], [105]. In a human proteasome study, Chen et al.

[54] reported, besides the s1 state, three coexisting conformations which are similar to either s2 or s3 states. These results indicate the conformational heterogeneity of the proteasome sample and difficulty of classification of the non s1-like particles.

Here we want to point out potential problems associated with the assignment of the conformational state of the proteasome. Our assignment is based on the conformational state of the ATPase, which was shown as different arrangements of the pore-1 loops and pocket distances. However, in most of the reported structures the ATPases were not resolved to the same extent as other regions of the proteasome. The EM density of the proteasome shows anisotropic resolution and the overall resolution is largely influenced by the high resolution of the CP structure. This hinders assigning reported EM maps with the same overall resolution to the conformational states. Additionally, in the reported models, the arrangement of the pore-1 loops in the s3-like states were not consistent within the EM maps (Table 4.4). Different classification approaches and different application of symmetry presumably influence the resolution of the ATPases and thereby prevents the assignment to particular states. Nevertheless, non s1-like proteasomes unambiguously represent one of the activated states of the proteasome.

## 5.2 The staircase arrangement of the AAA<sup>+</sup>-ATPase

The high-resolution EM map of the s1 state allowed us to build a precise model of the AAA<sup>+</sup>-ATPase of the proteasome. Using MDFF we were able to fit the model of the s1 state into the other states and obtained models for the s1, s2, s3, and s4 states. Six Rpt subunits form a ring structure as reported for other AAA<sup>+</sup>-ATPases. However, none of AAA<sup>+</sup>-ring structures of the yeast proteasome considered in this study exhibit a planar conformation. They rather form a right-handed twisted helical ring with a staircase conformation positioning the pore-loops at different heights. Five of the six interfaces of the Rpt subunits are tightly connected, whereas the interface between Rpt3 and Rpt6 contains a gap with a ramp forming a “lock washer” conformation in the s1 and s2 state. The pore-1 loops contain a conserved hydrophobic residue which directly interacts with the substrate polypeptide [119]. In the yeast s1 state, the N-terminal tips of the  $\alpha$ 8 helices, which are adjacent to the pore-1 loops, are arranged in a staircase with Rpt3 at the top and Rpt2 at the bottom position (Figure 4.16). We note that the pore-1 loop of Rpt3 is located next to the split site, while the pore-1 loop of Rpt6 is positioned nearly at the bottom. The split site of the lock washer between Rpt6 and Rpt3 exhibits the longest distance of the nucleotide pockets. Additionally the  $\alpha$ 8 helix of Rpt3 is situated almost horizontally with respect to the CP plane whereas the  $\alpha$ 8 helix of Rpt6 is tilted inwards. During the transition from s1 to s2, the AAA<sup>+</sup>-ring exhibits only a shift in its entirety but does not

undergo any significant conformational changes. The transition is most likely not to be driven by ATP hydrolysis, because our structural analysis implies that a different nucleotide-binding state is coupled to a difference in the pocket distance as observed in the s3 and s4 states. The question arises as to what triggers the transition from s1 to s2. One possibility is that it is regulated by the interaction of the N-terminal domain of Rpn1 with Rpt6 and Rpt2, which is not observed in the s1 state. Considering that Rpn1 binds substrates through the T1 site [42], substrate binding may trigger the conformational change of Rpn1 and the change is transmitted to the rest of the RP subunits to activate substrate processing by the proteasome.

The staircase conformation of the s3 state is rearranged in comparison to the s1 and s2 states in such a way that Rpt1 resides at the top and Rpt5 at the bottom position. The split site of the lock washer with the longest distance of the nucleotide-binding pocket is switched to the interface between Rpt5/1. As it was seen in the s1 and s2 states, the pore-1 loop of Rpt1 at the top position is adjacent to the split site. The split sites of the s1/s2 and s3 conformations are located on the opposite site of the AAA<sup>+</sup>-ring. The staircase arrangement of the lowly abundant transition state s4, in which Rpt5 is positioned at the top and Rpt3 at the bottom position is different from the other conformations. In the s4 state, the pocket distance of Rpt3-4 and Rpt4-5 showed an intermediate distance. It may represent either an intermediate conformation in which two subunits simultaneously hydrolyze ATP or a mixture of two different conformational states which could not be sorted by 3D classification. The low abundance of the s4 state in the BeF<sub>x</sub> data sets raise the possibility that this state is a short-lived one. In contrast, the s2 and s3 states, which represent states with the split site located on the opposite site of the lock washer, may represent more stable states in comparison to s4.

Thus, the proteasome changes the position of the pore-1 loops dynamically, presumably depending on ATP hydrolysis. The different arrangements of the pore-1 loops of the proteasome states show that substrate translocation is most likely coupled to ATP hydrolysis by changing the height of the pore-1 loops. The height difference of the  $\alpha$ -helices is approximately 20 Å, which is almost double the ClpX substrate translocation step size [120]. The pore-1 loops in the staircase arrangement can therefore most likely translocate a substrate with similar or larger step size than ClpX. The pore-2 loops follow the same arrangement as the pore-1 loops (Figure 4.16) and impose a translocation mechanism where the movements of the pore-loops are coupled.

The spiral staircase topology of the 26S proteasome has also been reported for other ring translocases of the ASCE superfamily like the AAA<sup>+</sup> E1 helicase, RecA-type Rho and DnaB helicase which adopt similar

conformations during substrate translocation [64]. In contrast ClpX, the bacterial homolog of the ATPase of the proteasome, adopts a more planar conformation in which each half of the ring contains a separate three-step staircase [67]. The only proteasome structure reported with a more planar ring topology, similar to ClpX, was solved in the presence of substrate [29]. Whether this conformation resulted from averaging of proteasome particles of different lock washer conformations or if the proteasome adopts a different topology during substrate translocation remains unclear. It is also unclear whether the ClpX ring will rearrange into a spiral staircase with only one split site upon substrate engagement. The advantage of a spiral staircase conformation, where the pore-1 loops alter their position during ATP hydrolysis, over a planar ring like topology comes from the larger height difference. Between the different proteasome states the pore-1 loops move from top to bottom positions resulting in a more efficient pulling of substrates during the power stroke.

### 5.3 Nucleotide binding pockets of the 26S proteasome

In all four reported yeast proteasome structures of this study all six nucleotide pockets exhibit nucleotide densities. This finding is in line with other reported high-resolution structures of the human proteasome in an s1-like state [54], [57], [81] which showed that all nucleotide pockets are occupied in the EM density. A recently reported yeast proteasome structure obtained in the presence of ADP and AIF<sub>x</sub> [115] showed only four out of six pockets occupied with a nucleotide density. This finding is consistent with previous biochemical work of other AAA<sup>+</sup>-ATPases [76]. However, the corresponding Rpt subunits are not resolved to the same extent as the occupied Rpt subunits (Figure 4.25) and might therefore hinder the unambiguous identification of nucleotide densities in the pockets of Rpt2 and Rpt6. Furthermore, the biochemical assays by Smith et al. [76] were conducted at a lower nucleotide concentration than used in the EM data acquisition (2 or 4 mM). This raises the question whether the full occupancy of the nucleotide pockets is a result of saturating nucleotide binding pockets with high concentration of nucleotides in the sample. The concentration of ATP in the cell is in the range of 0.05 – 5 mM. Interestingly, the purified proteasome activity has dose-dependency showing the highest activity at approximately 0.2 mM [121]. Cryo-EM analysis at a different ATP concentration together with biophysical experiments will provide further insights into the ATP hydrolysis mechanism of the 26S proteasome.

The arrangement of the pore-loops is related to the nucleotide pocket conformation of the 26S proteasome. In the engaged pockets, the Arg residues of the clockwise adjacent subunits coordinate the nucleotide [122]. The conformation is very similar to that of other AAA<sup>+</sup> family ATPases [60] where the β-

and  $\gamma$ - phosphates of the nucleotide are coordinated by the neighboring arginine side chains. Although a discrimination between ADP-Pi and ATP is not possible at 4 Å resolution the conformation of the engaged pocket favors the binding of ATP. In contrast, as observed already for the human proteasome structure [57], the split site of the lock washer shows a different conformation of the nucleotide pocket (Figure 4.17). The Arg residues are not in close contact to the bound nucleotide and instead form hydrogen bonds with the carboxyl groups of Rpt6. Since the nucleotide density bound to the open pocket is smaller in comparison to the other densities in the s1 state it is possible that ADP is bound instead of ATP.

#### 5.4 Gate-opening mechanism of the CP

The gate of the CP is formed by the N-terminal extensions of the  $\alpha$  subunits. In the closed-gate crystal structure the N-terminal extensions protrude into the central channel and block the access of substrates to the catalytic core of the CP [107]. The radial averages of the gate of the s1 state and the crystal structure of the closed 20S are identical, implying a closed gate in the s1 state. Additionally, the N-terminal extensions are in a similar conformation as the model of the crystal structure. In contrast the N-termini of the  $\alpha$  subunits turn up towards the AAA<sup>+</sup>-ring in the s4 state to form an open gate, similar to the structure of the PA26-CP complex [123]. Although the s4 state probably represents an open-gate structure, a rotation of the  $\alpha$  subunits as reported for the chimeric complex of PAN-20S, where the HbYX motifs of PAN were fused with PA26 [80], could not be observed. A higher resolution structure of the s4 state is necessary to describe the details of gate opening. The radial average of the gate of the s2 and s3 states is in between those of the s1 and the s4 state, probably representing a partially closed gate. It was reported for the complex of the proteasome activator Blm10 and the CP that the gate is in a “partially closed” conformation [74]. Flexible movements of the N-termini of the  $\alpha$  subunits could result in different opening states of the gate. Taking into consideration the flexibility of an unfolded polypeptide [124] the partially closed gate might hinder the diffusion of the polypeptide chain out of the CP.

It was reported that the interaction of the three HbYX motifs of Rpt2, 3 and 5 with the CP are important for the gate opening of the CP [114], [125]. In all yeast proteasome structures reported in this study, the three HbYX motifs bind constitutively to the pockets of the CP. Nevertheless in three out of four structures the gate is not completely open, suggesting that the engagement of the HbYX motifs is not sufficient to open the gate. In the open gate s4 structure the C-terminus of Rpt6 in addition to those HbYX motifs interacts with the pocket formed by  $\alpha$ 3 and  $\alpha$ 4. A biochemical study reported that the C-terminal tail of Rpt6 is almost as important for gate opening as the C-termini of Rpt2, 3 and 5 [126]. It is possible that the



C-termini of Rpt2, 3 and 5 stabilize the interaction of the RP with the CP, whereas the C-terminus of Rpt6 is important for the opening of the CP gate. An interaction of the pore-2 loops with the N-termini of the CP, as was reported for the complex of ClpX/P and suggested to stabilize the open gate conformation [127], was not observed in the structure of the s4 state. Nevertheless a transient interaction of flexible loop regions will most likely not be visible in the average of the EM density and is therefore still possible.

Besides the s4 structure, an open-gate structure ( $S_D$  conformation) of the human proteasome was reported [54]. Chen et al. [54] applied combinations of 2D and 3D classification and found a minor class in which the 20S gate is open. However, our analysis showed that the radial average of the EM density of the 20S gate rather resembled the s3 state than the s4 state, in which the gate is “partially open”. One explanation for the difference in the radial averages may be a different conformation of the N-termini of the  $\alpha$  subunits in the human structure. Interestingly, the interaction of the C-terminus of Rpt1 with the CP in the  $S_D$  state was not detected in the yeast s4 state of this study. Beside the differences observed for Rpt6, the C-terminus of Rpt1 showed a different conformation in the s1 and s2 states (Figure 4.21 B). However, biochemical studies reported that removing the tail of Rpt1 did not really influence gate opening [126]. It will be interesting to get a deeper insight into the gate opening mechanism by generating higher resolution EM densities of an open-gate structure of the proteasome and to decipher the different roles of the C-termini of the Rpt subunits.

## 5.5 Functional model of ATP hydrolysis coupled to substrate translocation

Based on the conformations of the AAA<sup>+</sup>-ring in the four states of the yeast proteasome, the following model describes the coupling of the translocation of substrate to ATP hydrolysis (Figure 5.1).

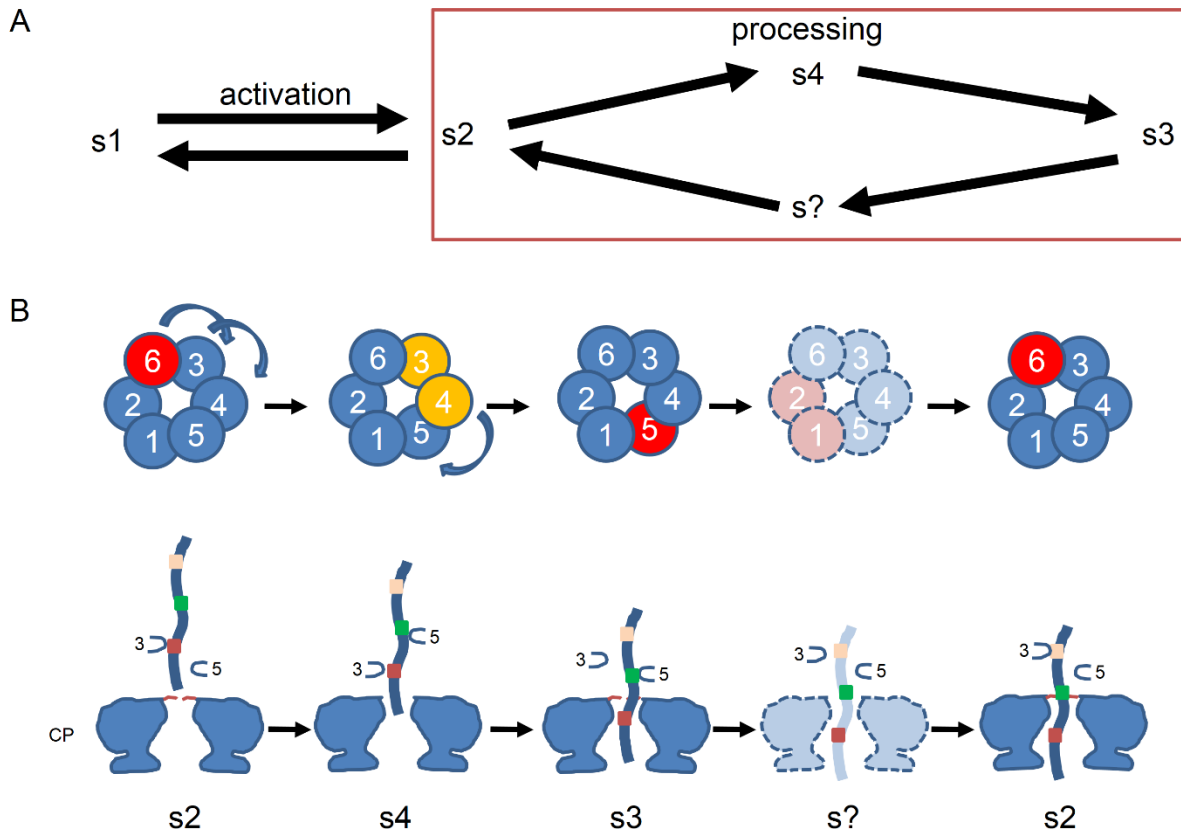


**Figure 5.1:** Model of the coupling between ATP hydrolysis and substrate translocation of the 26S proteasome (taken from [105]). **(A)** Upon activation, the proteasome shifts from the ground state (s1) to the substrate-processing states (s2, s3, and s4). **(B, Top)** ATP hydrolysis cycle occurs in a sequential order around the AAA<sup>+</sup>-ring. The conformational state of the nucleotide-binding pockets is shown in different colors (open, red; engaged, blue; and intermediate, yellow) **(B, Bottom)** Concerted conformational change of the AAA<sup>+</sup>-ATPase with the CP gate. The positions of the pore-1 loops of Rpt3 and Rpt5 are indicated. s?, hypothetical states.

The s1 state represents the ground state of the proteasome which is the major conformational state in the absence of substrate and most likely represents a low-energy conformation. Indeed, in situ studies of proteasomes from intact hippocampal neurons showed that 60-80% of the proteasomes inside the cell are present in an s1-like ground state [31]. The proteasome is activated in an ATP-independent manner, presumably by substrate binding because no conformational change was observed in the AAA<sup>+</sup>-ATPase from s1 to s2. In contrast, a conformational change of the subunit Rpn1 brings the N-terminus closer to

the AAA<sup>+</sup>-ring. It is possible that this transition is triggered by Rpn1 which interacts with both the AAA<sup>+</sup>-ring and ubiquitylated substrates [42].

In contrast, the transitions in the substrate processing states (s2, s3, and s4) are most likely to be driven by the hydrolysis of ATP. Those conformations probably represent snapshots of the mechanism by which substrate is translocated in an ATP dependent manner. To power substrate translocation, a conformational change of the pore-1 loop coupled to the release of Pi is required [124]. Additionally, the pore-1 loop of a subunit which is in contact to a translocated polypeptide has a higher probability of hydrolyzing ATP [128]. In the s2 state, the pore-1 loop of Rpt3 which is in the highest position in the staircase arrangement might interact with the substrate first, resulting in ATP hydrolysis of Rpt3-bound ATP. Mutation of the pore-2 loop of Rpt3 impaired the degradation of substrates even though ATP hydrolysis rate and gate opening were not affected [126]. Thus, similar to the pore-1 loop, the pore-2 loop interacts with a substrate polypeptide directly for the translocation.

Primary ATP hydrolysis of Rpt3 coupled to Pi release presumably leads a conformational change which brings the pore-1 loop of Rpt3 to the bottom of the staircase, thereby pulling the substrate into the direction of the CP. The movement of Rpt3 could then activate the clockwise adjacent subunit Rpt4 which shares an interface module with Rpt3. Rpt4 undergoes a conformational change resulting in the rearrangement of the staircase in which the pore-1 loop of Rpt4 is in the highest position (s4 state). As ATP hydrolysis of Rpt3 induces the conformational change of Rpt4, ATP hydrolysis of a subunit activates the clockwise adjacent subunit in a sequential reaction, resulting in the conformation observed in the s3 state. In the s3 state, the pore-1 loop of Rpt1 is at the top position of the staircase and the interaction of the pore-1 loop of Rpt1 with the substrate may initiate the next hydrolysis of ATP. Other short-lived transition states with open pockets of Rpt1-2 and Rpt2-6 are most likely to exist. The ADP- $\text{AlF}_x$  structure [115] may represent such a transition state of the proteasome. A concerted conformational change occurs to open the CP gate and allow the substrate to enter the antechamber of the proteasome. The intermediate gate conformations of the s2 and s3 states might hinder slipping back of translocated substrates.

Mechanochemical studies revealed that the substrate degradation by ClpX can be divided into a short burst phase and a long dwell phase. In the burst phase, substrate is translocated in conjunction with ATP hydrolysis and Pi release, whereas ADP is released and replaced by new ATP in the dwell phase [129]. Our structural analysis showed that the s2 and the s3 states are more abundant than the s4 state or other undiscovered conformations. Interestingly, it was reported for ClpX that three sequential hydrolysis reactions of ATP occur in the burst phase [129]. The s2 and s3 states might represent a resting state which

the proteasome adopts in the dwell phase. Thus, our cryo-EM analysis provided a snapshot of the proteasome reaction cycle and prefers a sequential hydrolysis model rather than a stochastic one.

## 6 Conclusion and Outlook

This work addressed the functional cycle of the ATPase module of the 26S proteasome using SPA cryo-EM studies. The EM maps of the proteasome in the four different states s1, s2, s3, and s4 provide further insights into the conformational changes of the ATPase coupled to substrate processing or ATP binding/hydrolysis. Additionally, the EM density of the s1 state, which was resolved to a resolution of 4.1 Å, allowed the construction of a near-atomic model of the yeast 26S proteasome which provides detailed insights into various aspects of the proteasome architecture. The nucleotide occupancy of the ATPases is similar to that of previously reported human proteasome structures [54], [57], [81]. However, in contrast to the human proteasome structures, the HbYX motifs of the yeast proteasome constitutively bind to the  $\alpha$ -ring of the CP in all four states. In the s4 state the C-terminus of Rpt6 additionally binds to the pocket formed by  $\alpha$ 3 and  $\alpha$ 4 and most likely is involved in the gate opening of the CP.

Despite several new insights, some questions were not answered by the structures obtained in this study. To understand the mechanochemical cycle of the proteasome reaction, a precise assignment of nucleotides, distinguishing either ATP or ADP-Pi, needs to be done by further improving the s1 structure. The detailed mechanism of gate opening triggered by interactions of the C-termini of Rpt subunits with the CP were unclear due to the lower resolution of the s4 state. A higher resolution of the EM density of the open-gate proteasome will help to decipher the interplay of ATPase and CP. Additionally, the low resolution map of the ATPase ring in the s4 state hindered interpreting the functional state. Unlike s2 and s3 states, the nucleotide pockets of Rpt3/4 and Rpt4/5 were not fully open. It is not clear whether the s4 state represents a mixture of two different states or a conformation stabilized by BeF<sub>x</sub>.

The ATPase conformations of the four states favor a sequential model for the ATPase cycle, where the neighboring Rpt subunit activates nucleotide hydrolysis of the adjacent subunit. This implies that six different conformational states of the proteasome might exist, each showing a different open pocket with the adjacent pore-loops at the top position. It would be interesting to find all six conformations and to gain a detailed understanding of the ATPase motor.

Finally, the development of 3D classification procedures focusing on individual areas of the 26S complex will help to obtain a better resolved EM density of as yet not well-resolved regions, leading to an accurate atomic model. Accurate models of the whole proteasome in the different conformational states will provide the basis for computational simulations which will help to better understand the conformational landscape of the 26S proteasome.

## 7 Appendix

### 7.1 Abbreviations

2D	= two-dimensional
3D	= three-dimensional
AAA <sup>+</sup> -ATPase	= ATPases associated with diverse cellular activities
ADP	= adenosine diphosphate
AlF <sub>x</sub>	= aluminum fluoride
AMP-PNP	= adenylyl-imidodiphosphate
Ar-Φ	= hydrophobic aromatic
Arg	= arginine
ASCE	= additional strand catalytic glutamate
ATP	= adenosine triphosphate
ATPγS	= adenosine 5'-(3-thiotriphosphate)
BeF <sub>x</sub>	= beryllium fluoride
BSA	= bovine serum albumin
CCD	= charge-coupled device
ClpX	= ATP-dependent caseinolytic protease X
CP	= core particle (20S proteasome)
CPh	= creatine phosphate
CPK	= creatine phosphate kinase
cryo-EM	= cryo-electron microscopy
CTF	= contrast transfer function
dc26S	= double-capped 26S proteasome
DDD	= direct detection device
dH <sub>2</sub> O	= ultrapure Water
DQE	= detective quantum efficiency
DTT	= dithiothreitol
E1	= ubiquitin-activating enzyme
E2	= ubiquitin-conjugating enzyme
E3	= ubiquitin-ligase
EDTA	= ethylenedinitrilotetraacetic acid disodium salt dehydrate
EM	= electron microscopy
EMDB	= Electron Microscopy Data Bank
FE	= FLAG eluate
FEG	= field emission gun
FSC	= Fourier shell correlation
FT	= Fourier transformation
HbYX	= hydrophobic-tyrosine-any amino acid tripeptide
HCl	= hydrochloric acid
HEPES	= N-2-Hydroxyethylpiperazine-N'-2-ethanesulfonic acid
iBAQ	= label-free intensity-based absolute quantification MS approach

MDFP	= molecular dynamics flexible fitting
MgCl <sub>2</sub>	= magnesium chloride
ML	= maximum likelihood
MOPS	= 3-(N-Morpholino)propanesulfonic acid
MPN	= Mpr1/Pad1 N-terminal
MS	= mass spectrometry
NaCl	= sodium chloride
NaF	= sodium fluoride
NSF	= N-Ethylmaleimide-Sensitive Factor
OB	= oligosaccharide binding
PAN	= proteasome-activating nucleotidase
PC	= proteasome/cyclosome
PCI	= proteasome-COP9-initiation factor
PDB	= Protein Data Bank
PIP	= proteasome interacting protein
PN	= protein homeostasis network
Pru	= pleckstrin-like receptor for ubiquitin
psc26S	= pseudo single-capped 26S proteasome
RMSD	= root-mean-square deviation
RP	= regulatory particle
Rpn	= regulatory particle non-ATPase
Rpt	= regulatory particle tripleA-ATPase
<i>S. cerevisiae</i>	= <i>Saccharomyces cerevisiae</i>
sc26S	= single-capped 26S proteasome
SDS-PAGE	= sodium dodecyl sulfate polyacrylamide gel electrophoresis
SNR	= signal-to-noise ratio
SP cryo-EM	= single-particle cryo-electron microscopy
SPA	= single-particle analysis
SPR	= single particle reconstructions
Suc-LLVY-AMC	= N-succinyl-Leu-Leu-Val-Tyr-7-amino-4-methylcoumarin
UA	= uranyl acetate
Ub	= ubiquitin
UbAld	= ubiquitin aldehyde
UBL	= ubiquitin-like
Ubp6	= ubiquitin-specific protease 6 (Usp14 in human)
UCSF	= University of California at San Francisco
UIM	= ubiquitin-interacting motif
UPS	= ubiquitin-proteasome-system
VMD	= Visual Molecular Dynamics, program for the visualization of molecular systems
YPD	= yeast extract peptone dextrose

## 7.2 Bibliography

1. Labbadia, J. and R.I. Morimoto, *The biology of proteostasis in aging and disease*. Annu Rev Biochem, 2015. **84**: p. 435-64.
2. Kim, Y.E., et al., *Molecular chaperone functions in protein folding and proteostasis*. Annu Rev Biochem, 2013. **82**: p. 323-55.
3. Finley, D., *Recognition and processing of ubiquitin-protein conjugates by the proteasome*. Annu Rev Biochem, 2009. **78**: p. 477-513.
4. Yang, Z. and D.J. Klionsky, *Mammalian autophagy: core molecular machinery and signaling regulation*. Curr Opin Cell Biol, 2010. **22**(2): p. 124-31.
5. Hershko, A. and A. Ciechanover, *The ubiquitin system*. Annu Rev Biochem, 1998. **67**: p. 425-79.
6. Finley, D., et al., *The ubiquitin-proteasome system of Saccharomyces cerevisiae*. Genetics, 2012. **192**(2): p. 319-60.
7. Corn, P.G., *Role of the ubiquitin proteasome system in renal cell carcinoma*. BMC Biochem, 2007. **8 Suppl 1**: p. S4.
8. McGrath, J.P., S. Jentsch, and A. Varshavsky, *UBA 1: an essential yeast gene encoding ubiquitin-activating enzyme*. EMBO J, 1991. **10**(1): p. 227-36.
9. Deshaies, R.J. and C.A. Joazeiro, *RING domain E3 ubiquitin ligases*. Annu Rev Biochem, 2009. **78**: p. 399-434.
10. Varshavsky, A., *The ubiquitin system, an immense realm*. Annu Rev Biochem, 2012. **81**: p. 167-76.
11. Peng, J., et al., *A proteomics approach to understanding protein ubiquitination*. Nat Biotechnol, 2003. **21**(8): p. 921-6.
12. Tagwerker, C., et al., *A tandem affinity tag for two-step purification under fully denaturing conditions: application in ubiquitin profiling and protein complex identification combined with in vivocross-linking*. Mol Cell Proteomics, 2006. **5**(4): p. 737-48.
13. Meierhofer, D., et al., *Quantitative analysis of global ubiquitination in HeLa cells by mass spectrometry*. J Proteome Res, 2008. **7**(10): p. 4566-76.
14. Xu, P., et al., *Quantitative proteomics reveals the function of unconventional ubiquitin chains in proteasomal degradation*. Cell, 2009. **137**(1): p. 133-45.
15. Komander, D. and M. Rape, *The ubiquitin code*. Annu Rev Biochem, 2012. **81**: p. 203-29.
16. Ciechanover, A., *Intracellular protein degradation: from a vague idea through the lysosome and the ubiquitin-proteasome system and onto human diseases and drug targeting*. Neurodegener Dis, 2012. **10**(1-4): p. 7-22.
17. Thrower, J.S., et al., *Recognition of the polyubiquitin proteolytic signal*. Embo j, 2000. **19**(1): p. 94-102.
18. Kravtsova-Ivantsiv, Y. and A. Ciechanover, *Non-canonical ubiquitin-based signals for proteasomal degradation*. J Cell Sci, 2012. **125**(Pt 3): p. 539-48.
19. Lu, Y., et al., *Substrate degradation by the proteasome: a single-molecule kinetic analysis*. Science, 2015. **348**(6231): p. 1250834.
20. Meyer, H.J. and M. Rape, *Enhanced protein degradation by branched ubiquitin chains*. Cell, 2014. **157**(4): p. 910-21.
21. Verma, R., et al., *Role of Rpn11 metalloprotease in deubiquitination and degradation by the 26S proteasome*. Science, 2002. **298**(5593): p. 611-5.
22. Prakash, S., et al., *An unstructured initiation site is required for efficient proteasome-mediated degradation*. Nat Struct Mol Biol, 2004. **11**(9): p. 830-7.
23. Voges, D., P. Zwickl, and W. Baumeister, *The 26S proteasome: a molecular machine designed for controlled proteolysis*. Annu Rev Biochem, 1999. **68**: p. 1015-68.
24. Peters, J.M., et al., *Structural features of the 26 S proteasome complex*. J Mol Biol, 1993. **234**(4): p. 932-7.



25. Bohn, S., et al., *Structure of the 26S proteasome from Schizosaccharomyces pombe at subnanometer resolution*. Proc. Natl Acad Sci U S A, 2010. **107**(49): p. 20992-20997.
26. Beck, F., et al., *Near-atomic resolution structural model of the yeast 26S proteasome*. Proc. Natl Acad Sci U S A, 2012. **109**(37): p. 14870-5.
27. Lander, G.C., et al., *Complete subunit architecture of the proteasome regulatory particle*. Nature, 2012. **482**(7384): p. 186-91.
28. Lasker, K., et al., *Molecular architecture of the 26S proteasome holocomplex determined by an integrative approach*. Proc. Natl Acad Sci U S A, 2012. **109**(5): p. 1380-7.
29. Matyskiela, M.E., G.C. Lander, and A. Martin, *Conformational switching of the 26S proteasome enables substrate degradation*. Nat Struct Mol Biol, 2013. **20**(7): p. 781-8.
30. Sledz, P., et al., *Structure of the 26S proteasome with ATP-gammaS bound provides insights into the mechanism of nucleotide-dependent substrate translocation*. Proc. Natl Acad Sci U S A, 2013. **110**(18): p. 7264-9.
31. Asano, S., et al., *A molecular census of 26S proteasomes in intact neurons*. Science, 2015. **347**(6220): p. 439-442.
32. Pathare, G.R., et al., *The proteasomal subunit Rpn6 is a molecular clamp holding the core and regulatory subcomplexes together*. Proc Natl Acad Sci U S A, 2012. **109**(1): p. 149-54.
33. Pathare, G.R., et al., *Crystal structure of the proteasomal deubiquitylation module Rpn8-Rpn11*. Proc. Natl Acad Sci U S A, 2014.
34. Worden, E.J., C. Padovani, and A. Martin, *Structure of the Rpn11-Rpn8 dimer reveals mechanisms of substrate deubiquitination during proteasomal degradation*. Nat Struct Mol Biol, 2014. **21**(3): p. 220-7.
35. Funakoshi, M., et al., *Sem1, the yeast ortholog of a human BRCA2-binding protein, is a component of the proteasome regulatory particle that enhances proteasome stability*. J Cell Sci, 2004. **117**(Pt 26): p. 6447-54.
36. Estrin, E., et al., *Formation of an intricate helical bundle dictates the assembly of the 26S proteasome lid*. Structure, 2013. **21**(9): p. 1624-35.
37. Yao, T. and R.E. Cohen, *A cryptic protease couples deubiquitination and degradation by the proteasome*. Nature, 2002. **419**(6905): p. 403-7.
38. Neuwald, A.F., et al., *AAA+: A class of chaperone-like ATPases associated with the assembly, operation, and disassembly of protein complexes*. Genome Res, 1999. **9**(1): p. 27-43.
39. Iyer, L.M., et al., *Evolutionary history and higher order classification of AAA+ ATPases*. J Struct Biol, 2004. **146**(1-2): p. 11-31.
40. Hanson, P.I. and S.W. Whiteheart, *AAA+ proteins: have engine, will work*. Nat Rev Mol Cell Biol, 2005. **6**(7): p. 519-529.
41. Rosenzweig, R., et al., *Rpn1 and Rpn2 coordinate ubiquitin processing factors at proteasome*. J Biol Chem, 2012. **287**(18): p. 14659-71.
42. Shi, Y., et al., *Rpn1 provides adjacent receptor sites for substrate binding and deubiquitination by the proteasome*. Science, 2016. **351**(6275).
43. He, J., et al., *The structure of the 26S proteasome subunit Rpn2 reveals its PC repeat domain as a closed toroid of two concentric alpha-helical rings*. Structure, 2012. **20**(3): p. 513-21.
44. Husnjak, K., et al., *Proteasome subunit Rpn13 is a novel ubiquitin receptor*. Nature, 2008. **453**(7194): p. 481-8.
45. Schreiner, P., et al., *Ubiquitin docking at the proteasome through a novel pleckstrin-homology domain interaction*. Nature, 2008. **453**(7194): p. 548-52.
46. Riedinger, C., et al., *Structure of Rpn10 and its interactions with polyubiquitin chains and the proteasome subunit Rpn12*. J Biol Chem, 2010. **285**(44): p. 33992-4003.
47. Chen, L. and K. Madura, *Rad23 promotes the targeting of proteolytic substrates to the proteasome*. Mol Cell Biol, 2002. **22**(13): p. 4902-13.

48. Funakoshi, M., et al., *Budding yeast Dsk2p is a polyubiquitin-binding protein that can interact with the proteasome*. Proc Natl Acad Sci U S A, 2002. **99**(2): p. 745-50.
49. Saeki, Y., et al., *Identification of ubiquitin-like protein-binding subunits of the 26S proteasome*. Biochem Biophys Res Commun, 2002. **296**(4): p. 813-9.
50. Kaplun, L., et al., *The DNA damage-inducible Ubl-UbA protein Ddi1 participates in Mec1-mediated degradation of Ho endonuclease*. Mol Cell Biol, 2005. **25**(13): p. 5355-62.
51. Unverdorben, P., et al., *Deep classification of a large cryo-EM dataset defines the conformational landscape of the 26S proteasome*. Proc. Natl Acad Sci U S A, 2014. **111**(15): p. 5544-9.
52. Aufderheide, A., *Structural studies of the 26S proteasome and its interaction with Ubp6 by cryo-electron microscopy*. 2016, Technische Universität München: PhD thesis.
53. Wehmer, M. and E. Sakata, *Recent advances in the structural biology of the 26S proteasome*. Int J Biochem Cell Biol, 2016. **79**: p. 437-442.
54. Chen, S., et al., *Structural basis for dynamic regulation of the human 26S proteasome*. Proc. Natl Acad Sci U S A, 2016. **113**(46): p. 12991-12996.
55. Forster, F., et al., *An atomic model AAA-ATPase/20S core particle sub-complex of the 26S proteasome*. Biochem Biophys Res Commun, 2009. **388**(2): p. 228-33.
56. Tomko, R.J., Jr., et al., *Heterohexameric ring arrangement of the eukaryotic proteasomal ATPases: implications for proteasome structure and assembly*. Mol Cell, 2010. **38**(3): p. 393-403.
57. Schweitzer, A., et al., *Structure of the human 26S proteasome at a resolution of 3.9 Å*. Proc. Natl Acad Sci U S A, 2016. **113**(28): p. 7816-21.
58. Aufderheide, A., et al., *Structural characterization of the interaction of Ubp6 with the 26S proteasome*. Proc. Natl Acad Sci U S A, 2015. **112**(28): p. 8626-31.
59. Lander, G.C., A. Martin, and E. Nogales, *The proteasome under the microscope: the regulatory particle in focus*. Curr Opin Struct Biol, 2013. **23**(2): p. 243-51.
60. Wendler, P., et al., *Structure and function of the AAA+ nucleotide binding pocket*. Biochim Biophys Acta., 2012. **1823**(1): p. 2-14.
61. Iosefson, O., et al., *Coordinated gripping of substrate by subunits of an AAA+ proteolytic machine*. Nat Chem Biol, 2015.
62. Baker, T.A. and R.T. Sauer, *ClpXP, an ATP-powered unfolding and protein-degradation machine*. Biochim Biophys Acta, 2012. **1823**(1): p. 15-28.
63. Lyubimov, A.Y., M. Strycharska, and J.M. Berger, *The nuts and bolts of ring-translocase structure and mechanism*. Curr Opin Struct Biol, 2011. **21**(2): p. 240-8.
64. Nyquist, K. and A. Martin, *Marching to the beat of the ring: polypeptide translocation by AAA+ proteases*. Trends Biochem Sci., 2014. **39**(2): p. 53-60.
65. Itsathitphaisarn, O., et al., *The hexameric helicase DnaB adopts a nonplanar conformation during translocation*. Cell, 2012. **151**(2): p. 267-77.
66. Thomsen, N.D. and J.M. Berger, *Running in reverse: the structural basis for translocation polarity in hexameric helicases*. Cell, 2009. **139**(3): p. 523-34.
67. Glynn, S.E., et al., *Crystal structures of asymmetric ClpX hexamers reveal nucleotide-dependent motions in a AAA+ protein-unfolding machine*. Cell, 2009. **139**(4): p. 744-756.
68. Zhao, M. and A.T. Brunger, *Recent Advances in Deciphering the Structure and Molecular Mechanism of the AAA+ ATPase N-Ethylmaleimide-Sensitive Factor (NSF)*. J Mol Biol, 2016. **428**(9 Pt B): p. 1912-26.
69. Groll, M., et al., *Structure of 20S proteasome from yeast at 2.4 Å resolution*. Nature, 1997. **386**(6624): p. 463-71.
70. Chen, P. and M. Hochstrasser, *Autocatalytic subunit processing couples active site formation in the 20S proteasome to completion of assembly*. Cell, 1996. **86**(6): p. 961-72.

71. Arendt, C.S. and M. Hochstrasser, *Identification of the yeast 20S proteasome catalytic centers and subunit interactions required for active-site formation*. Proc Natl Acad Sci U S A, 1997. **94**(14): p. 7156-61.
72. Groll, M., et al., *Molecular machines for protein degradation*. Chembiochem, 2005. **6**(2): p. 222-56.
73. Baumeister, W., et al., *The proteasome: paradigm of a self-compartmentalizing protease*. Cell, 1998. **92**(3): p. 367-80.
74. Sadre-Bazzaz, K., et al., *Structure of a Blm10 complex reveals common mechanisms for proteasome binding and gate opening*. Mol Cell, 2010. **37**(5): p. 728-35.
75. Tian, G., et al., *An asymmetric interface between the regulatory and core particles of the proteasome*. Nat Struct Mol Biol, 2011. **18**(11): p. 1259-67.
76. Smith, D.M., et al., *ATP binds to proteasomal ATPases in pairs with distinct functional effects, implying an ordered reaction cycle*. Cell, 2011. **144**(4): p. 526-38.
77. Benaroudj, N., et al., *ATP hydrolysis by the proteasome regulatory complex PAN serves multiple functions in protein degradation*. Mol Cell, 2003. **11**(1): p. 69-78.
78. Rabl, J., et al., *Mechanism of gate opening in the 20S proteasome by the proteasomal ATPases*. Mol Cell, 2008. **30**(3): p. 360-8.
79. Forster, A., et al., *The 1.9 Å structure of a proteasome-11S activator complex and implications for proteasome-PAN/PA700 interactions*. Mol Cell, 2005. **18**(5): p. 589-99.
80. Yu, Y., et al., *Interactions of PAN's C-termini with archaeal 20S proteasome and implications for the eukaryotic proteasome-ATPase interactions*. Embo j, 2010. **29**(3): p. 692-702.
81. Huang, X., et al., *An atomic structure of the human 26S proteasome*. Nat Struct Mol Biol, 2016. **23**(9): p. 778-85.
82. Luan, B., et al., *Structure of an endogenous yeast 26S proteasome reveals two major conformational states*. Proc. Natl Acad Sci U S A, 2016. **113**(10): p. 2642-7.
83. Bradford, M.M., *A rapid and sensitive method for the quantitation of microgram quantities of protein utilizing the principle of protein-dye binding*. Anal Biochem, 1976. **72**: p. 248-54.
84. Bartolommei, G., M.R. Moncelli, and F. Tadini-Buoninsegni, *A method to measure hydrolytic activity of adenosinetriphosphatases (ATPases)*. PLoS One, 2013. **8**(3): p. e58615.
85. Cox, J., et al., *Accurate proteome-wide label-free quantification by delayed normalization and maximal peptide ratio extraction, termed MaxLFQ*. Mol Cell Proteomics, 2014. **13**(9): p. 2513-26.
86. Ruskin, R.S., Z. Yu, and N. Grigorieff, *Quantitative characterization of electron detectors for transmission electron microscopy*. J Struct Biol, 2013. **184**(3): p. 385-93.
87. McMullan, G., et al., *Comparison of optimal performance at 300keV of three direct electron detectors for use in low dose electron microscopy*. Ultramicroscopy, 2014. **147**: p. 156-63.
88. Kuijper, M., et al., *FEI's direct electron detector developments: Embarking on a revolution in cryo-TEM*. J Struct Biol, 2015. **192**(2): p. 179-87.
89. Li, X., et al., *Electron counting and beam-induced motion correction enable near-atomic-resolution single-particle cryo-EM*. Nat Methods., 2013. **10**(6): p. 584-90.
90. Frank, J., *Three-dimensional electron microscopy of macromolecular assemblies : visualization of biological molecules in their native state*. 2nd ed. 2006, Oxford ; New York: Oxford University Press. xiv, 410 p.
91. Korinek, A., et al., *Computer controlled cryo-electron microscopy--TOM(2) a software package for high-throughput applications*. J Struct Biol, 2011. **175**(3): p. 394-405.
92. Grant, T. and N. Grigorieff, *Automatic estimation and correction of anisotropic magnification distortion in electron microscopes*. J Struct Biol, 2015. **192**(2): p. 204-8.
93. Li, X., et al., *Electron counting and beam-induced motion correction enable near-atomic-resolution single-particle cryo-EM*. Nat Methods, 2013. **10**(6): p. 584-90.

94. Mindell, J.A. and N. Grigorieff, *Accurate determination of local defocus and specimen tilt in electron microscopy*. J Struct Biol, 2003. **142**(3): p. 334-47.
95. Frank, J., *Single-particle reconstruction of biological macromolecules in electron microscopy--30 years*. Q Rev Biophys, 2009. **42**(3): p. 139-58.
96. Orlova, E.V. and H.R. Saibil, *Structural analysis of macromolecular assemblies by electron microscopy*. Chem Rev, 2011. **111**(12): p. 7710-48.
97. Egelman, E.H., *Comprehensive biophysics*. 2012, Amsterdam ; New York: Elsevier. 9 volumes.
98. Nogales, E. and S.H. Scheres, *Cryo-EM: A Unique Tool for the Visualization of Macromolecular Complexity*. Mol Cell, 2015. **58**(4): p. 677-89.
99. van Heel, M., et al., *Single-particle electron cryo-microscopy: towards atomic resolution*. Q Rev Biophys, 2000. **33**(4): p. 307-69.
100. Sorzano, C.O.S., et al., *Optimization problems in electron microscopy of single particles*. Annals of Operations Research, 2006. **148**(1): p. 133-165.
101. Sigworth, F.J., et al., *An introduction to maximum-likelihood methods in cryo-EM*. Methods Enzymol, 2010. **482**: p. 263-94.
102. Penczek, P.A., R.A. Grassucci, and J. Frank, *The ribosome at improved resolution: new techniques for merging and orientation refinement in 3D cryo-electron microscopy of biological particles*. Ultramicroscopy, 1994. **53**(3): p. 251-70.
103. Scheres, S.H., *RELION: implementation of a Bayesian approach to cryo-EM structure determination*. J Struct Biol, 2012. **180**(3): p. 519-30.
104. Scheres, S.H., et al., *Disentangling conformational states of macromolecules in 3D-EM through likelihood optimization*. Nat Methods, 2007. **4**(1): p. 27-9.
105. Wehmer, M., et al., *Structural insights into the functional cycle of the ATPase module of the 26S proteasome*. Proc Natl Acad Sci U S A, 2017. **114**(6): p. 1305-1310.
106. Chen, S., et al., *High-resolution noise substitution to measure overfitting and validate resolution in 3D structure determination by single particle electron cryomicroscopy*. Ultramicroscopy, 2013. **135**: p. 24-35.
107. Huber, E.M., et al., *A unified mechanism for proteolysis and autocatalytic activation in the 20S proteasome*. Nat Commun., 2016. **7**: p. 10900.
108. Goh, B.C., et al., *Computational Methodologies for Real-Space Structural Refinement of Large Macromolecular Complexes*. Annu Rev Biophys., 2016. **45**: p. 253-78.
109. Trabuco, L.G., et al., *Molecular dynamics flexible fitting: a practical guide to combine cryo-electron microscopy and X-ray crystallography*. Methods, 2009. **49**(2): p. 174-80.
110. Ribeiro, J.V., et al., *QwikMD - Integrative Molecular Dynamics Toolkit for Novices and Experts*. Sci Rep., 2016. **6**: p. 26536.
111. Humphrey, W., A. Dalke, and K. Schulten, *VMD: visual molecular dynamics*. J Mol Graph., 1996. **14**(1): p. 33-8, 27-8.
112. Phillips, J.C., et al., *Scalable molecular dynamics with NAMD*. J Comput Chem., 2005. **26**(16): p. 1781-802.
113. Sakata, E., et al., *The catalytic activity of Ubp6 enhances maturation of the proteasomal regulatory particle*. Mol Cell, 2011. **42**(5): p. 637-49.
114. Smith, D.M., et al., *Docking of the proteasomal ATPases' carboxyl termini in the 20S proteasome's alpha ring opens the gate for substrate entry*. Mol Cell, 2007. **27**(5): p. 731-44.
115. Ding, Z., et al., *High-resolution cryo-EM structure of the proteasome in complex with ADP-AIFx*. Cell Res, 2017. **27**(3): p. 373-385.
116. Scheres, S.H., *Processing of Structurally Heterogeneous Cryo-EM Data in RELION*. Methods Enzymol, 2016. **579**: p. 125-57.
117. Nguyen, T.H., et al., *Cryo-EM structure of the yeast U4/U6.U5 tri-snRNP at 3.7 Å resolution*. Nature, 2016. **530**(7590): p. 298-302.

118. Nguyen, T.H., et al., *The architecture of the spliceosomal U4/U6.U5 tri-snRNP*. Nature, 2015. **523**(7558): p. 47-52.
119. Park, E., et al., *Role of the GYVG pore motif of HslU ATPase in protein unfolding and translocation for degradation by HslV peptidase*. J Biol Chem, 2005. **280**(24): p. 22892-8.
120. Liu, S., G. Chistol, and C. Bustamante, *Mechanical operation and intersubunit coordination of ring-shaped molecular motors: insights from single-molecule studies*. Biophys. J, 2014. **106**(9): p. 1844-58.
121. Huang, H., et al., *Physiological levels of ATP negatively regulate proteasome function*. Cell Res, 2010. **20**(12): p. 1372-85.
122. Kim, Y.C., et al., *ATP binding to neighbouring subunits and intersubunit allosteric coupling underlie proteasomal ATPase function*. Nat Commun, 2015. **6**: p. 8520.
123. Whitby, F.G., et al., *Structural basis for the activation of 20S proteasomes by 11S regulators*. Nature, 2000. **408**(6808): p. 115-20.
124. Sen, M., et al., *The ClpXP Protease Unfolds Substrates Using a Constant Rate of Pulling but Different Gears*. Cell, 2013. **155**(3): p. 636-46.
125. Gillette, T.G., et al., *Differential roles of the COOH termini of AAA subunits of PA700 (19 S regulator) in asymmetric assembly and activation of the 26 S proteasome*. J Biol Chem, 2008. **283**(46): p. 31813-22.
126. Beckwith, R., et al., *Reconstitution of the 26S proteasome reveals functional asymmetries in its AAA+ unfoldase*. Nat Struct Mol Biol, 2013. **20**(10): p. 1164-72.
127. Martin, A., T.A. Baker, and R.T. Sauer, *Distinct static and dynamic interactions control ATPase-peptidase communication in a AAA+ protease*. Mol Cell, 2007. **27**(1): p. 41-52.
128. Martin, A., T.A. Baker, and R.T. Sauer, *Pore loops of the AAA+ ClpX machine grip substrates to drive translocation and unfolding*. Nat Struct Mol Biol, 2008. **15**(11): p. 1147-51.
129. Rodriguez-Aliaga, P., et al., *Substrate-translocating loops regulate mechanochemical coupling and power production in AAA+ protease ClpXP*. Nat Struct Mol Biol, 2016.

### 7.3 Acknowledgements

The work of this thesis was conducted in the department of Molecular Structural Biology at the Max Planck Institute for Biochemistry in Martinsried. I would like to thank all department members for the good working atmosphere. In particular, I would like to thank the following people.

I would like to thank Prof. Dr. Wolfgang Baumeister for the supervision of this thesis and the opportunity he gave me to dive into the world of electron microscopy. I want to point out the excellent infrastructure he has built up in the department which provides perfect research conditions.

I would especially like to thank Dr. Eri Sakata, my direct supervisor and mentor during my thesis, for her constant support, advice and all the fruitful discussion we had. I also want to thank her for reading this thesis.

I would also like to acknowledge all members of my thesis advisory committee for their helpful comments and discussions during our annual meetings: Prof. Dr. Wolfgang Baumeister, Prof. Dr. Sevil Weinkauf, Dr. Eri Sakata and Prof. Dr. Friedrich Förster.

Special thanks go to Oana Mihalache and Günter Pfeifer who helped me a lot in learning how to work with electron microscopes. Especially I would like to thank Günter for all the time we spent at the microscope acquiring thousands of micrographs. In addition I would like to thank Prof. Dr. Jürgen Plitzko for the effort he puts in the electron microscope infrastructure at the Max Planck Institute and for being such a great mentor during my time as a member of the department.

I am grateful to the members of the “Krisenteam”: Florian Beck, Antje Aufderheide and Till Rudack for spending endless hours in the computer room, doing data processing, model building and data analysis. Especially I want to thank Florian for his support in computational work and all the time he spent answering my questions.

I would like to thank Birgit Book and Nathalie Leclercq for the help in organization and Inga Wolf for helping with computer problems. In addition I would like to thank Fuku, Niko, Andreas, Uli, Maryam, Markus, Nicole and Rado for their support, help and the good time in the department.

I am grateful to the students Stefan Juhas, Alexander Ulrich and Friederike Mey, whom I was allowed to supervise during my thesis.

I would like to thank Jürgen Peters and Ruben Fernandez-Busnadiego for proof reading my thesis.

I would like to thank my girlfriend Inez for all the support and especially for the care packages she prepared during the intense paper writing period. Last but not least, I would like to thank my family and my friends who have supported me during my studies.